Cellular mechanoresponse to extracellular matrix shear strain and stiffness studied in a cell culture model of breast gland development

Dissertation

Zur

Erlangung des Doktorgrades (Dr. rer. Nat)

der

Mathematisch-Naturwissenschaftlichen Fakultät

der

Rheinischen Friedrich-Wilhelms-Universität Bonn

Vorgelegt von

Friedland, Florian

aus

Berlin

Bonn, November 2022

Angefertigt mit Genehmigung der Mathematisch-Naturwissenschaftlichen Fakultät
der Rheinischen Friedrich-Wilhelms-Universität Bonn

1. Gutachter: Prof. Dr. Rudolf Merkel
2. Gutachter: Prof. Dr. Ulrich Kubitscheck

Tag der Promotion: 20.03.2023

Erscheinungsjahr: 2023

Abstract

Mechanobiological regulation is a crucial element for tissue development and homeostasis. Dysregulation of the normal mechanobiological microenvironment of cells is linked to disease and negatively affects cancer patients' clinical outcomes. On the level of individual cells, much is known on sensation and transduction of mechanical signals. However, it remains elusive how cells integrate multiple signals on a tissue level to orchestrate complex differentiation processes of cells and tissues. A promising approach to elucidate these processes is offered by experiments on three-dimensional (3D) cell culture models like breast epithelial spheroids grown in EHS (Engelbreth Holm Swarm) hydrogels.

The breast gland is a mechanically active tissue constantly subjected to shear deformations by external forces, for example, upon normal physiological activity. However, little is known about the role of these forces in mammary epithelium development and homeostasis because tools to study the impact of such mechanical cues are still lacking.

In this work, a novel shear stress device was employed to apply physiological stress to breast epithelial spheroids. This device utilized magnetic coupling to apply tangential force to the surface of EHS-substrate-derived hydrogels. Moreover, it enabled confocal live cell microscopy over extended periods. The resulting strain in gels was thoroughly analyzed by tracking gel-embedded fluorescent microspheres in 3D. These measurements confirmed reproducible formation of pure and constant shear strain throughout the whole analysis volume. Three-dimensional breast epithelial spheroids with nature-like architecture were subsequently embedded into hydrogels to analyze cellular shear stress responses. Confocal microscopy of the cells' actin cytoskeleton allowed for the determination of shear strain amplitude within gel-embedded spheroids. This analysis revealed a significant decrease in strain compared to the surrounding matrix, implying a mechanical resistance of breast spheroids to extracellular matrix (ECM) strain. Analyses of strain response in spheroids of different developmental stages showed that spheroid architecture and basement membrane (BM) development are crucial for breast epithelial mechanical resistance.

The device was then utilized to cyclically strain spheroids for prolonged periods (22 hours). Cell viability was not compromised by this procedure. Mechanoresponse was studied by live cell analysis of actin cytoskeleton dynamics. In young, low-developed spheroids cellular morphology indicated a loss of cell-cell contacts upon cyclic shear stress. Furthermore,

stressed spheroids were extruding cells that subsequently underwent apoptosis as shown by immunocytochemical labeling of the apoptotic effector protein cleaved caspase-3. Quantification revealed that cell extrusion as a cellular response to shear stress application was exclusively occurring in young, immature spheroids with incomplete epithelial differentiation.

During cancer development, the breast gland ECM undergoes intensive remodeling processes. Here, increased stiffness in tumor tissue causes increased malignant behavior and frequency of BM invasion events. However, due to a sparsity of appropriate tools it is only rudimentary known how cell force generation is modified by the extracellular matrix (ECM) in a physiological 3D context.

Therefore, development of a 3D traction force microscopy (TFM) approach that will allow for the investigation of breast spheroid-derived forces was begun by tracking of microsphere displacements. Confocal image stacks were analyzed with dedicated image processing routines to accurately determine microsphere displacement in 3D and over time. This 3D TFM approach enabled measurement and visualization of spheroid-derived matrix deformation patterns in 3D. Surprisingly strong tangential displacements were observed close to the spheroids' surfaces. Further development of this novel tool will allow for the quantification of mammary epithelial force generation in response to natural and tumor-like microenvironments in 3D.

In essence, this work was concerned with the mechanobiological regulation of breast gland development and homeostasis. Development of a novel 3D TFM approach was initiated with the aim of investigating cellular force generation in mammary epithelial spheroids. By use of a novel device on a cell culture model of the breast gland, it was possible to apply physiological stresses in a nature-like matrix to mimic the complex mechanical microenvironment of breast epithelial tissue and to observe cellular mechanoresponses to this important mechanical cue.

Table of contents

Abbreviations

°C	Degree Celcius
2D	Two dimensional
3D	Three dimensional
AJ	Adherens junction
AFM	Atomic force microscopy
AM+	Assay medium with EGF
AM-	Assay medium without EGF
BM	Basement membrane
cC-3	Cleavec Caspase-3
DWI	Leibniz-Institut für Interaktive Materialien
ECM	Extra cellular matrix
EGF	Epidermal growth factor
EHS	Engelbreth-Holme-Swarm
Em	Emission
EMT	Epithelial to mesenchymal transition
ERK	Extracellular signal-regulated kinases (ERK)
Ex	Excitation
F-Actin	Fibrous actin
FZJ	Forschungszentrum Jülich
FA	Focal adhesion
GM	Growth medium
$GdCl_3$	Gadolinium (III) chloride
G-Actin	Globular actin
HD	Hemidesmosome
IBI-2	Institute for Biological Information Processing
LCI	Live cell imaging
LSM	laser scanning microscope
LTM	Lehrstuhl für Technische Mechanik
MCF	Michigan cancer foundation
MMP	Matrix metalloproteases
MSC	Mechanosensitive ion channel
n.s.	not significant
PDMS	Poly dimethyl siloxane
Rcf	rotational centrifugal force
RT	Room temperature
RWTH	Rheinisch-Westfälische Technische Hochschule Aachen
S1P	Sphingosine-1-phosphate
TEB	Terminal end bud
TFM	traction force microscopy

Figures

Tables

1 Introduction

All cells of the human body are constantly subjected to mechanical stress. For example, endothelial cells of the vasculature experience fluid shear stress by blood flow [1], cardiac myocytes undergo cyclic compression during heart pumping [2], and the epithelium of the lung faces tensile stress during breathing [3]. Tissue stiffness ranges widely from breast tissue (~167 Pa [4]) to bone surface (9.9 GPa [5]). Cells sense both extracellular forces and stiffness of the extracellular matrix (ECM) and adapt to them. Cells integrate mechanical cues into biochemical signaling cascades (mechanotransduction) to modulate their motility, differentiation, and morphology. Understanding how these processes are facilitated on a molecular level is crucial for comprehending tissue-scale cellular dynamics [6]. Such mechanobiological regulation circuits are known to steer tissue development, homeostasis, and wound healing [7–9]. Further, is the dysregulation of this cellular mechanical microenvironment of healthy tissue directly linked to many diseases, especially cancer development and progression [10–13]. Understanding mechanoresponses, therefore, has broad implications in a clinical context.

As a naturally mechanically active tissue, the breast gland is a fascinating subject to study cellular mechanobiological regulation. The adult epithelial breast gland is embedded into a soft fatty tissue (~167 Pa [4]), which is constantly strained upon daily body motion [14,15]. During sport exercise, these stresses result in shear straining of the breast tissue of up to 50%. Further, breast gland tissue undergoes fundamental morphological and functional remodeling that depends on changing physiological demands: For instance, during lactation, the gland is also subjected to static milk pressure and radial contractile forces of myoepithelial cells [16].

However, this mechanical microenvironment is dysregulated in the course of cancer progression. Here, solid forces of a growing tumor mass, reciprocal tissue stiffening, and interstitial pressure act on the epithelial gland [16]. Such dysregulations are known to fuel cancer progression and negatively affect clinical outcomes. Shedding light on how the normal breast epithelium and mammary cancer cells sense and integrate these mechanical signals on a molecular level is therefore relevant for developing new clinical approaches to cancer treatment.

The following sections describe how cells sense and interpret mechanical cues on a molecular level and how cell culture models in physiological environments are utilized to study mechanoresponses on a tissue scale level *in vitro*.

1.1 Cellular mechanosensing and mechanotransduction mechanisms

Cells are physically connected to neighboring cells and the extracellular matrix (ECM), a fibrous network of proteins, via cell-cell and cell-ECM adhesive complexes. Externally applied or internally generated forces are therefore propagated throughout a tissue. The ECM composition, and thereby its mechanical properties, is tissue-specific [17].

Specialized proteins enable cells to transduce mechanical cues, such as substrate stiffness or tensile forces, into biochemical signals [18,19]. Cells adapt to these mechanical cues by changing morphology or migratory behavior or altering gene expression levels that influence their differentiation. Cellular mechanosensing and the resulting signaling cascades are therefore critical elements of tissue development and its ability to execute its function, thereby enabling multicellular organisms [20,21].

The following chapters will describe how mechanical forces are transmitted at cellular and tissue levels. Further will be explained how cells facilitate sensing and mechanotransduction of mechanical cues.

1.1.1 The cytoskeleton is decisive for cellular mechanoresponses

The cytoskeleton is a fibrous protein framework that governs cellular shape and fulfills various purposes. Three filamentous networks comprise the cytoskeleton: Microtubules, Intermediate filaments, and microfilaments (F-Actin) (Figure 1 A). These networks are to some degree interconnected or connected to the same cellular structures, serving, however, distinct functions. Microtubules are the thickest filaments (25 nm) spanning from a microtubule organizing center to the periphery (in non-mitotic cells [22]). Motor proteins such as dynein or kinesin can bind cargo such as vesicles or cell organelles while simultaneously moving along microtubules, facilitating directional transport within cells [23,24]. Continuous growth at the peripheral end of microtubules further allows for generation of pushing forces [25].

Intermediate filaments are thinner than microtubules (8-10 nm) and encapsulate a variety of filamentous protein structures, which mostly serve as a static mechanical support system that buffers mechanical stress through its flexibility [26]. The intermediate filament keratin, e.g., is found in high concentrations in the skin, where it serves as a mechanical stabilizer that helps maintain tissue integrity [27].

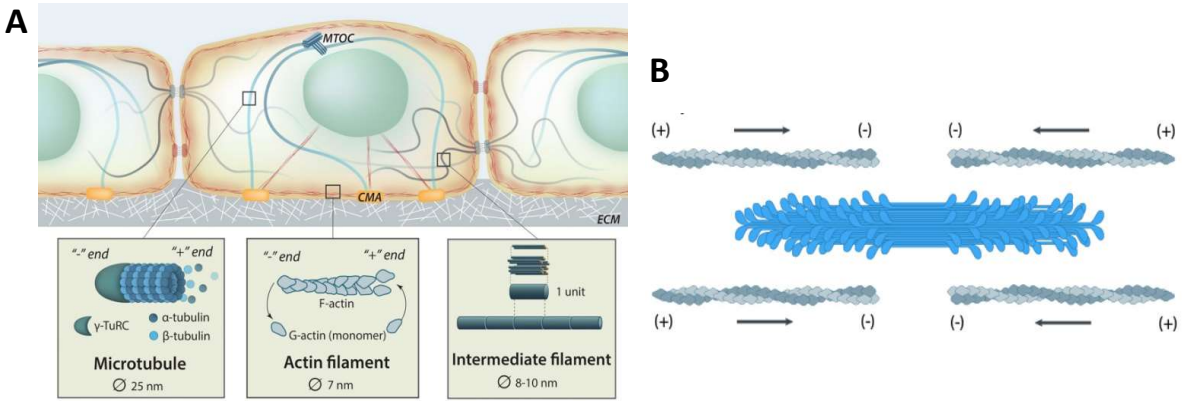

Figure 1: Cytoskeletal composition and actomyosin-based cellular force generation. (A) Schematic of cytoskeletal morphology in a cell. (B) Principle of force generation via actomyosin contraction. Actin filaments (grey) are shifted by activity of Myosin II (Blue). Adapted from [35]

From a mechanobiological perspective, is the actin cytoskeleton the most important cytoskeletal element. It is composed of thin (7 nm) microfilaments that form crosslinked branched or linear networks of fibrous actin (F-actin) [28].

F-actin is formed through the polymerization of globular actin (G-actin) under hydrolysis of ATP to ADP [29]. Formation and dissociation of F-actin is orchestrated by various F-Actin-Binding factors such as Rho-GTPase signals or Nucleation Promoting Factors and environmental cues such as temperature or indirectly by control of G-actin concentration in a cell [30,31]. The highly dynamic control of F-actin assembly and disassembly allows cells to rapidly integrate various signals into a cellular response by reorganizing the cytoskeletal actin network.

F-actin comprises the framework of force-generating actomyosin and is one of the most abundant proteins in eukaryotic cells. Organized in thick bundles with the motor protein myosin II is F-actin composing the contractile apparatus of muscle tissue [32].

Non-muscle myosin II allows for generation of cellular contractile forces by shifting parallel actin filaments in opposite directions (Figure 1 B). Thus, actomyosin is essential for cellular force generation also of non-muscle cells.

Non-muscle myosin II was shown to be a crucial element in epithelial-to-mesenchymal transition (EMT) and force-driven basement membrane (BM) invasion in breast epithelial cells [33,34].

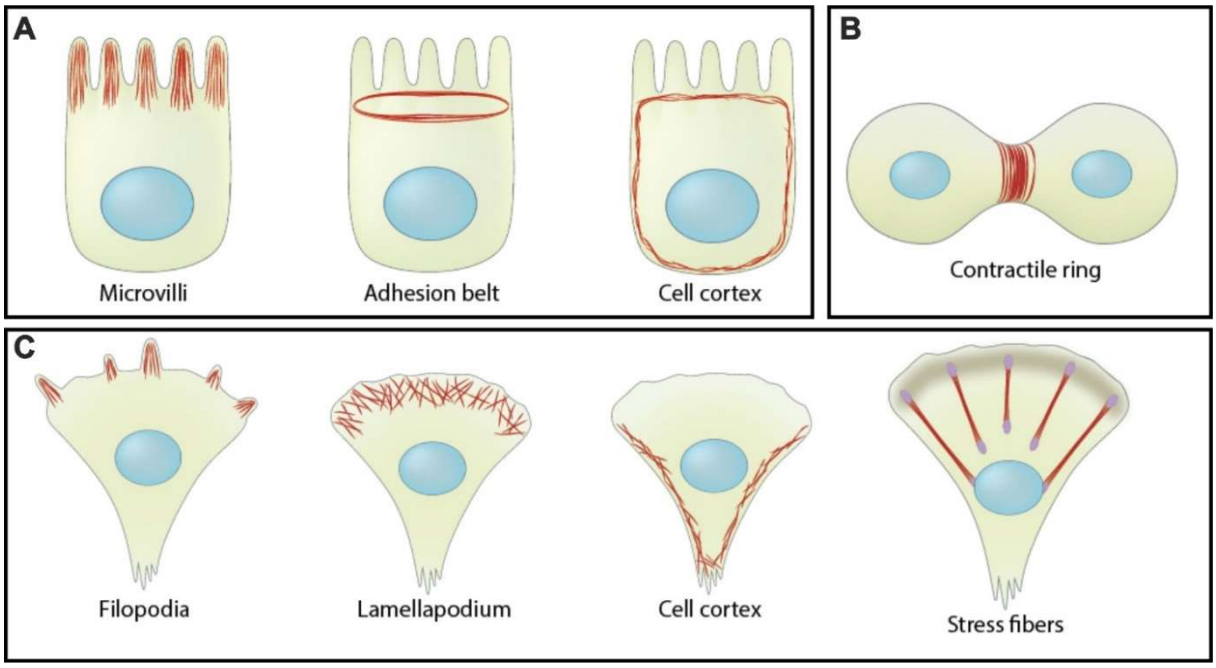

Figure 2: The actin cytoskeleton. Schematics depicting different F-actin organization in (A) polarized epithelial cells, (B) mitotic cells or (C) migrating cells of mesenchymal morphology. Adapted from [35]

The actin cytoskeleton enables cells to adapt their shape (morphology), form protrusions and migrate [36]. The branched cortical actomyosin network is anchored to the plasma membrane and regulates membrane tension and cell shape (Figure 2 A & C) [37,38]. In preparation for mitosis, the cortical network contracts to increase membrane tension, resulting in round morphology of cells (Figure 2 B) [39]. Additional contractile actin ring formation then allows for the separation of the two daughter cells [40].

Morphological adaption from a sessile, polarized epithelial cell to a migrating mesenchymal cell requires reorganization of the cortical actin networks during epithelial-to-mesenchymal transition (EMT) (Figure 2 A & C) [41]. EMT is further often accompanied by increased migration [42]. Migration of single cells or as a collective also depends on actomyosin-derived force generation [43,44]. Highly motile cells often exhibit stress fiber formation (figure 2 B). Stress fibers are thick bundles of crosslinked linear F-actin and non-muscle myosin II. They are either formed by reinforcement of cortical actin or polymerized at matrix adhesion sites (for details, see chapter 1.1.2) and allow cells to generate increased contractile forces for migration[45,46].

In essence, the actin cytoskeleton and non-muscle myosin II allow for cellular force generation. Further is the organization of the actin cytoskeleton inseparable from cellular morphology and migratory behavior.

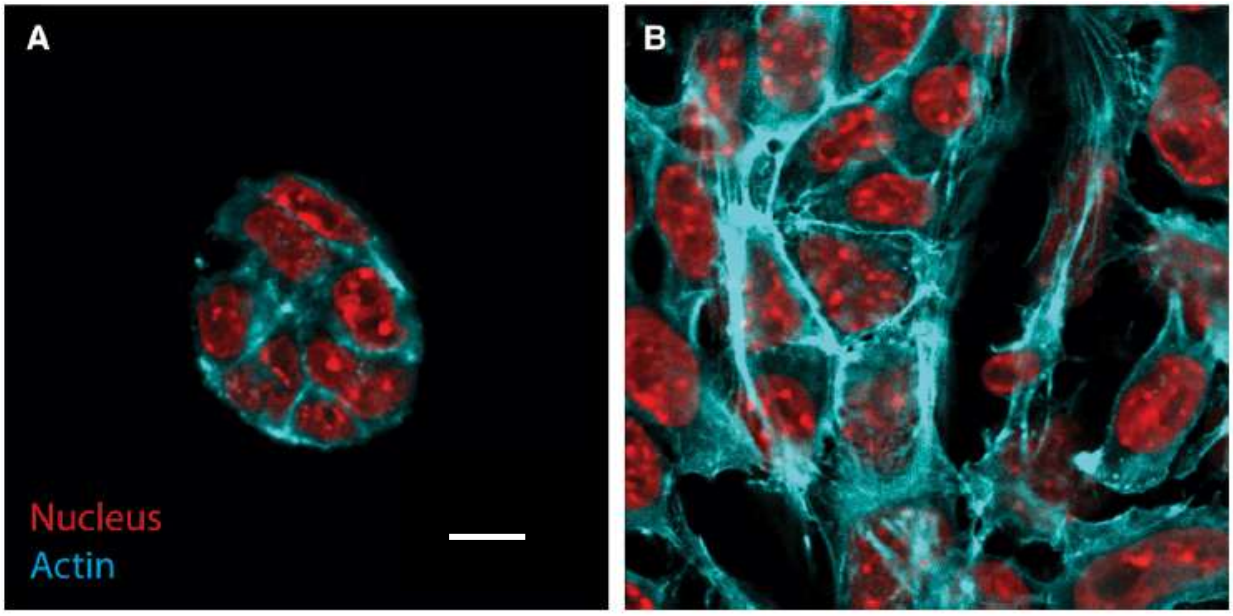

Figure 3: Actin Reorganization during Developmental Transitions. Micrographs of embryonic stem cells before and after adapting their morphology on stiff cell culture plastic (2.28-3.38 GPa [47]) (A) Native pluripotent stem cells exhibit mostly cortical actin networks. (B) In response to a stiff substrate, the cells lose their pluripotency and adopt a spread-out morphology accompanied by reorganization of the actin cytoskeleton and stress fiber formation. Scale = 10 µm. Adapted from [48]

For example, cortical actin is predominant in embryonic stem cells (Figure 3 A), but they adopt flat- and spread-out morphology and stress fiber formation when cultured on stiff cell culture plastics (Figure 3 B). Further was shown that the motility of cells in response to high-stiffness substrates is dramatically increased [49].

In lung epithelial monolayers, neighboring cells form contractile actomyosin rings to shed apoptotic cells to maintain homeostatic cell numbers while preserving epithelial barrier function (Figure 4 A). Extrusion of living cells was also observed to be a mechanoresponse to crowding and is similarly facilitate by the formation of a contractile actomyosin ring (Figure 4 A). Thereby, dynamic processes of actin cytoskeleton reorganization and targeted force generation have significant implications for tissue development and homeostasis.

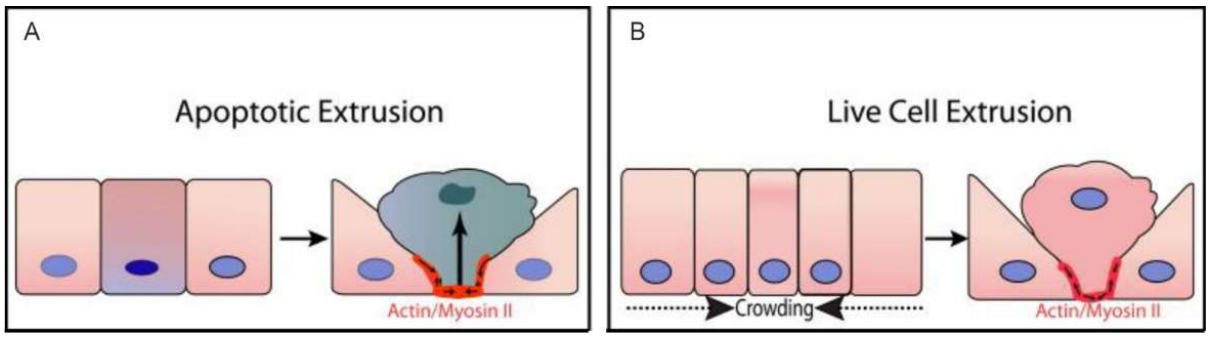

Figure 4: Contractile actomyosin ring formation allows for cellular extrusion from epithelial monolayers. Epithlieum cells generate actomyosin rings across multiple neighboring cells to facilitate active cell extrusion of (A) apoptotic cells or (B) as a mechanoresponse to crowding to extrude live cells. Adapted from [252]

The actin cytoskeleton is not only generating forces but is also directly involved in sensing mechanical cues. The cortical actin network forms membrane protrusions like filopodia, blebs, or microspikes [34,44]. Such protrusions act as ECM-mechanosensing units for probing of the environment. Tensed F-actin can bind transcription factors, forcing their localization to the cytosol. Thereby can F-actin tension directly influences transcription factor activity of promoting DNA transcription in the nucleus [50].

Essentially, the actin cytoskeleton is a highly dynamic multiprotein network that facilitates cellular movement and morphological adaptions integral to cellular and tissue functions. Observation of such fundamental processes is crucial in characterizing cellular mechanoresponses, which are often accompanied by actin cytoskeleton reorganization.

1.1.2 Mechanosensitive cell junctions and ECM adhesions

Tissues are composed not only of cells but also of a fibrous protein network, the extra cellular matrix (ECM), that acts as a scaffold. Cells are connected to neighboring cells and the ECM via specialized cell junctions and adhesion sites to facilitate tissue integrity and force transmission.

Cell-cell junctions are aggregations of multiprotein complexes which connect cytoskeletal components to transmembrane receptors of neighboring cells (Figure 5). Desmosomes allow the interconnection of intermediate filament networks of neighboring cells via transmembrane cadherins [51]. Adherens junctions (AJs), on the other hand, allow for interconnecting actin networks between cells. Such interconnection of cytoskeletal networks allows for direct force transmission between cells, be it active force generation via actin tensions or passive deformations resulting from external force application [52].

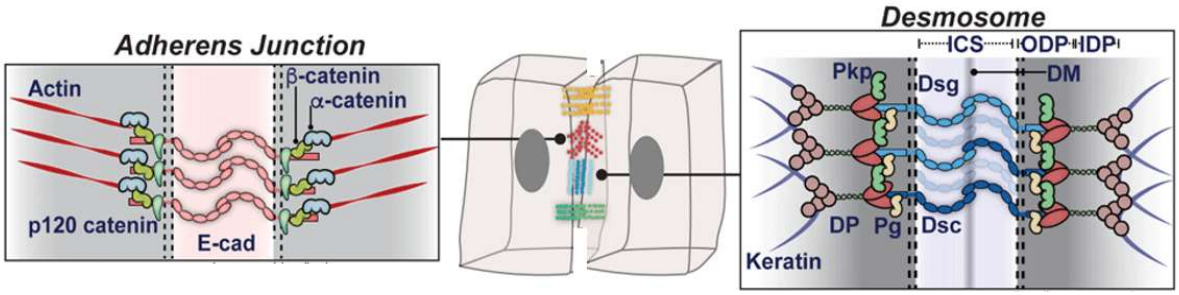

Figure 5: Schematic representing the major molecular components of adherens junctions and desmosomes. (A) Cells anchor the actin cytoskeleton to adherens junction by interaction of cadherins, β-catenin and actin binding α-catenin (B) Desmosomal cadherins desmogleins (dsg) and desmocollins (dsc) interact with plakoglobin (Pg) and plakophilins (Pkp) and desmoplakin (DP) to anchor the intermediate filaments of a neighboring cell. Adapted from [53]

Adherens junctions are also capable of sensing and transducing tensional forces [54]. The tensional force of F-actin unfolds a cryptic binding site on α-catenin proteins at AJs. They undergo conformational changes under tension that allows the binding of vinculin. The vinculins have two additional binding sites for actin, thereby promoting actin cytoskeleton reinforcement and more force generation [55,56]. Alternatively, other proteins like Afadin, Formins, or α-actinin be recruited to trigger AJ reinforcement by different signaling pathways [57]. Cell-cell junctions thereby serve both as a physical connection between cells and as tension sensors.

Cells also connect to the ECM, a cell-secreted complex scaffold of proteins (figure 6). While in general mainly composed of collagens, fibronectins, laminins and elastin, is the ECM protein composition highly specific to tissues and their function [58,59].

Similar to cytoskeletal components, the ECM is highly dynamic. Embedded cells remodel the ECM by the production and secretion of ECM components or matrix metalloproteases (MMPs) to stabilize or break down the ECM. Thus, cells dynamically shape their environment and alter the mechanical properties of the surrounding tissue [60].

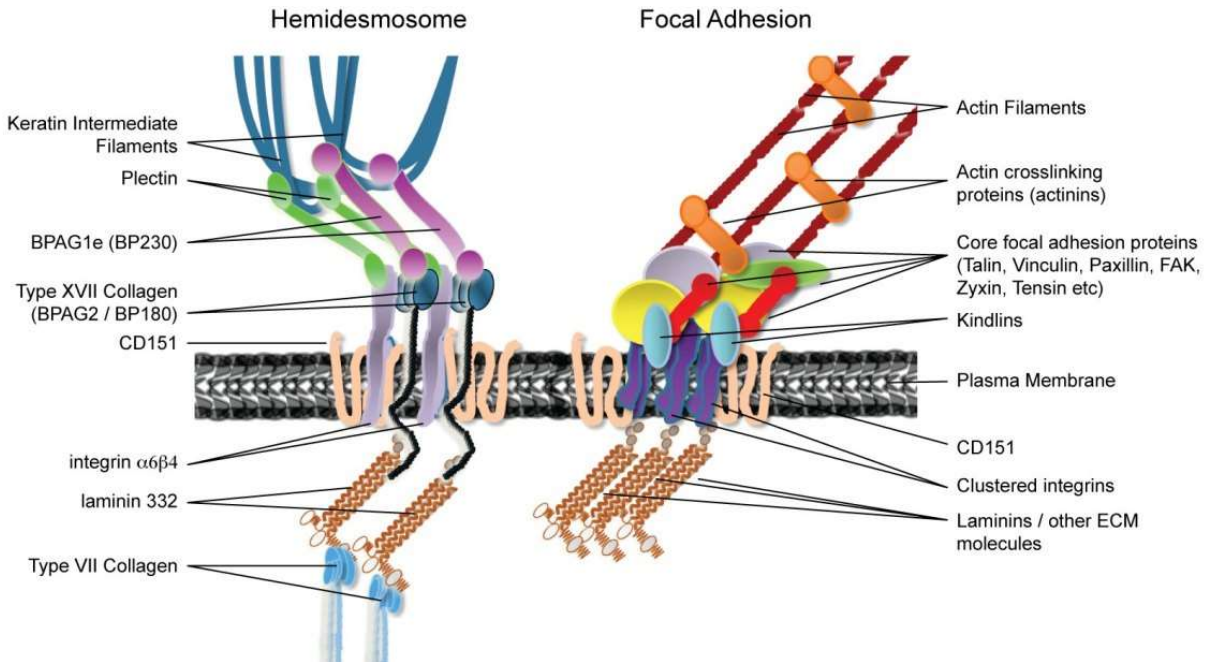

Figure 6: Schemetic representing the major molecular components of hemidesmosmoes and focal adhesion. Hemdidesmosomes and focal adhesions are aggregates of transmembrane receptor proteins integrin. The integrins bind ECM components and connective protein complexes that attach to intermediate filaments (hemidesmosomes) or F-actin (focal adhesions). Adapted from [276]

Specialized adhesion complexes called focal adhesions (FAs) allow cells to link their actin cytoskeleton directly to ECM proteins like collagens, laminin, vitronectin or fibronectin (Figure 6). Thereby are FAs enabling the application of tensional forces to their ECM. FAs are essential for cell migration, where they are formed at the leading edge of cells. The formation of contractile stress fibers at FAs allows a cell to pull itself in the migration direction [61]. High tension forces at FAs results, analog to AJs, in the reinforcement of actomyosin and increased recruitment of integrins [62]. Turnover of FA proteins and reinforcement by tension sensing allows for continuous dynamic assembly and disassembly of FAs at the leading edge of migrating cells (Figure 2 C) [63]. At FAs, the focal adhesion kinase (FAK) activation is modulated by both tension and matrix rigidity [64,65]. The FAK is a major player in various cellular signaling circuits which govern cell division, survival, migration and force generation [66,67]. Overexpression of FAK is a frequent occurrence in advanced-stage solid cancers, leading to a high interest in its dynamics and activation for the development of therapeutics [68].

Therefore, binding of a cells cytoskeleton to ECM molecules via adhesions sites not only provides mechanical stability and scaffold for migration but allows for mechanosensing of matrix stiffness and tensional forces.

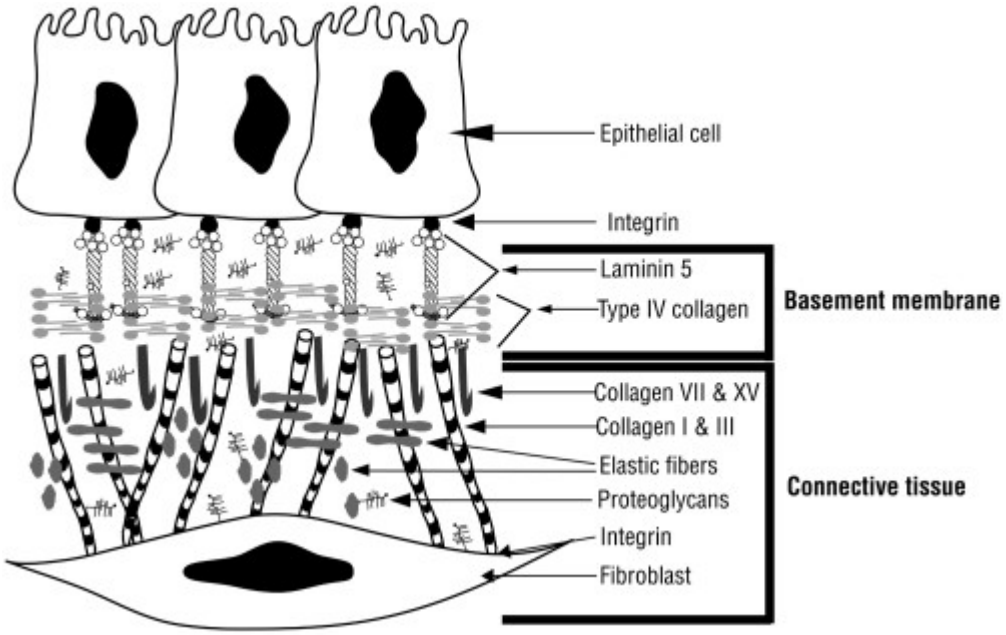

Figure 7: The basement membrane. The basement membrane forms by binding of laminins by epithelial cell via integrins which promotes assembly of a collagen type IV network. FAdapted from [277]

A special form of ECM is the basement membrane (BM), comprised of up to 50 components but mostly laminins, proteoglycans, nidogen, and up to 50% collagen type IV [69]. The BM protein meshwork is very dense and can function as a diffusion barrier [70]. The BM is unique due to its composition, localization, and function. Separating epithelial cells from the surrounding connective tissue is the BM found in tissues like the skin, the gastrointestinal tract or the mammary gland, where it serves as a supporting structure and cell adhesion site [71]. Further is the BM a physical barrier that protects against the invasion of transformed epithelial cancer cells [72]. The BM also provides mechanical cues for the epithelium such as stiffness gradients which promote polarized cell orientation[73]. These cues are sensed by cells through the mechanical coupling of the BM with the intracellular intermediate filament network via hemidesmosomes (HDs) (Figure 6). Hemidesmosomal connection of specific integrins to the BM is vital for normal mammary gland morphogenesis and epithelial differentiation [74]. Dysregulation of BM-epithelial adhesion sites is further implied to promote a malignant, invasive behavior in cancer cells, highlighting the role of the BM for normal breast tissue homeostasis [75,76].

Both FAs and HDs utilize transmembrane proteins of the integrin family, which act as mechanotransducers from the ECM to intracellular networks [77]. They are implied in various fundamental cellular processes such as migration and cancer cell invasion, proliferation, and differentiation [78–80].

Tissue integrity and homeostasis is controlled by the ECMs composition, cellular cytoskeleton networks and their interconnectivity through cell-cell and cell-matrix adhesions. This connective continuum of cells and the ECM allows cell-generated and external forces to be transmitted through tissues. Thereby transmitted forces and matrix stiffness are sensed and integrated into vital cellular processes.

1.1.3 Mechanosensitive ion channels

Mechanosensitive ion channels (MSCs) have been intensively studied and characterized as major contributors to cellular mechanosensitivity [81–83]. From bacteria to plants and animals, MSCs contribute to cellular function and mechanoadaption. MCSs are membrane-bound channel proteins that undergo conformational changes under tension to open partially or entirely to facilitate ion movement over the otherwise hydrophobic lipid bilayer [84]. They serve various functions on various scales ranging from touch sensation and hearing to control of cell proliferation and differentiation [85–88]. Since their discovery in 1984, many MSCs have been identified and structurally well characterized [89–91]. Still, it remains unknown how exactly force is transmitted to those channels exactly. Both membrane tension and direct tethering of MSCs to cytoskeletal components are indicated to play a role in the mechanical opening of the channels (Figure 8 A & B) [84,92].

When opened, they allow for a rapid flux of ions across the channels, activating various signaling circuits such as depolarization of neurons or dysregulation of the mitochondrial regulatory machinery through Ca^{2+} influx [93,94]. Considering that MSCs exhibit variations in sensitivity to stress as well as varying selectivity to ions, are the global mechanosensitive capabilities a spectrum rather than an on/off response (Figure 8 C)[95,96]. Further are the expression levels of MSCs, such as Piezo1, dependent on age (including alteration during embryogenesis) and tissue [97–99]. Further, can expression levels of Piezo1 diverge for different cell types within a tissue and are dependent on cellular differentiation state [100].

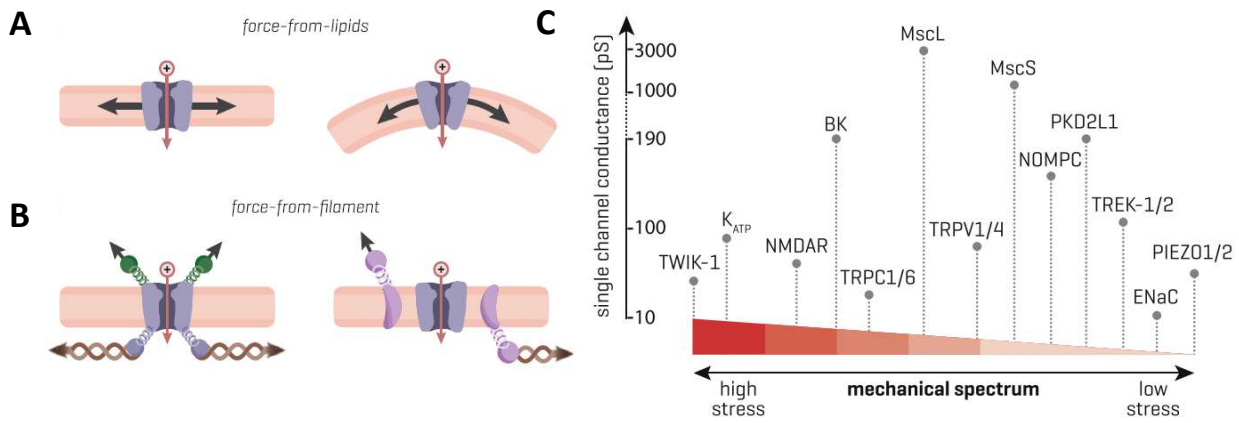

Figure 8: Principle of mechanosensitive ion channel force gated opening. Proposed modes for force gated opening of MSCs by (A) membrane tension and (B) direct force application through connected proteins. Red arrow indicates ion flow, green represents ECM filament, brown represents cytosceletal components and violet represents transmembrane proteins. (C) MSCs sensitivity as measured by patch-clamp technique. Structure of ECM and cytoskeletal networks may shift MSCs along the spectrum. Adapted from [91]**.**

Many profound tissue-scale processes of mammalian cells have been shown to rely on MSC activity. By deletion and pharmacological blocking, it was found that Piezo1 is responsible for the cellular sensation of crowding in human lung epithelial monolayers [101,102]. The cellular response to this crowding effect was the production of intracellular Sphingosine-1-Phosphate (S1P), which prompts neighboring cells to extrude the S1P-producing cells via a contractile actin ring which ultimately leads to apoptotic cell death of the extruded cell (Figure 4). *In vivo,* this process is believed to regulate tissue homeostasis by shedding cells in crowded monolayers. Interestingly, disruption of this S1P pathway results in cellular behavior common for aggressive tumors [103]. The MSCs proteins Piezo1 and TRPV4 were also suggested to activate extracellular signal-regulated kinases (ERK), which facilitate transcription factor activation to regulate gene expression involved in fundamental cellular processes like proliferation and cell survival, extracellular matrix degradation, and migration [104–106]. Malignant activation of ERK signaling in cancer cells is known to increase tumor cell invasion into the adjacent tissue, thereby enabling the formation of metastases [107]. Further, did Piezo1 knockout in mice results in ultimately lethal deregulation of embryonic development evident by growth-retardation, pericardial effusion, and impeded cardiovascular function [108].

Mechanosensing, transduction, and responses are significant processes for normal cellular behavior and tissue homeostasis. How specific mechanical cues are integrated into cellular behavior can dramatically differ depending on the tissue of origin, as differentiation drastically changes the expression pattern of mechanosensitive components [109,110].

In vitro Investigations of single cellular mechanoregulatory processes benefit from minimizing factors to identify molecular components and signaling pathways. To study mechanobiological regulation on a tissue scale, however, it is necessary to mimic the tissue of interest on a global scale, including the cells' cytoskeletal structure, cell-cell and cell-matrix contacts, the ECM and mechanical stresses.

1.2 Mechanobiological regulation of normal breast tissue development and function

The mammary epithelium is a mechanically active tissue [16]. Adult breast tissue is subjected to extreme external tissue deformation during exercise. The amplitude of strain was measured by Haake & Surr to be up to 50% during exercise [15]. Norris et al. measured peak breast skin strain to be widely ranging between the breast support type, activity and breast size. For example, under low support conditions were skin strain rates on average 24% (11-47%) during standing, 26% (14-49%) during walking and 35% (19-62%) while running [14]. In breast tissue, these complex deformations are best described by shear forces acting on a solid elastic object (figure 9).

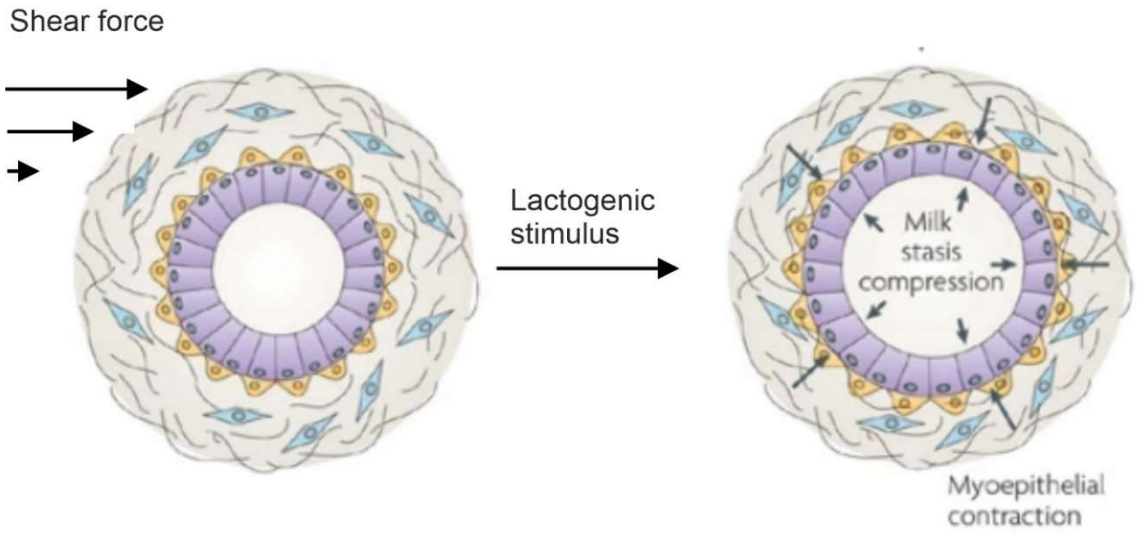

Figure 9: Forces acting on the breast epithelium. The normal mammary gland is subjected to shear force. Upon lactogenic stimulus, hydrostatic luminar pressure and contractile forces derived from myopithelial cells add additional mechanical stresses. Adapted from [16]

During puberty and pregnancy, the mammary epithelium undergoes reorganization coupled with systematic growth, branching, and cellular differentiation, which involves epithelial collective migration into the fatty breast tissue [111]. During hormone-triggered lactation, the mammary epithelium is subjected to static milk pressure and contractile forces derived from myoepithelial cells to eject milk [112].

1.2.1 Mammary gland architecture and development

As the name suggests, the mammary gland is an organ exclusive to mammals and ontogenetically derived from hair follicles [113]. As an endocrine gland, it serves the production of milk for the nourishment of newborns, which is tightly controlled by circulating hormones during and after pregnancy [114]. The mammary gland differentiates itself from other tissues because its development is not completed at birth. Instead, is most of the gland typical branching morphogenesis executed during puberty [115].

At birth, the mammary gland consists of a rudimentary mammary tree embedded into adipose tissue below the nipple (Figure 10 A) [116]. Upon puberty onset, the female body begins with fat collection and adipocyte aggregation in the breast, resulting in tissue growth [117]. Branching morphogenesis of the epithelial cells is then triggered by the secretion of hormones like estrogen [118]. During this stage, the mammary epithelium rapidly proliferates and forms terminal end buds, which grow into the adipose tissue of the breast (Figure 10 B) [119]. Along with hormonal cues, this process is believed to involve mechanical adaption of the ECM via matrix metalloproteases (MMPs) and integrin-mediated mechanosensing [111,120]. While cap cells at the tip of TEB facilitate directed migration based on ECM structure, are body cells of the TEB proliferative, thereby producing the cells which settle in the mammary ducts as differentiated luminal cells [121].

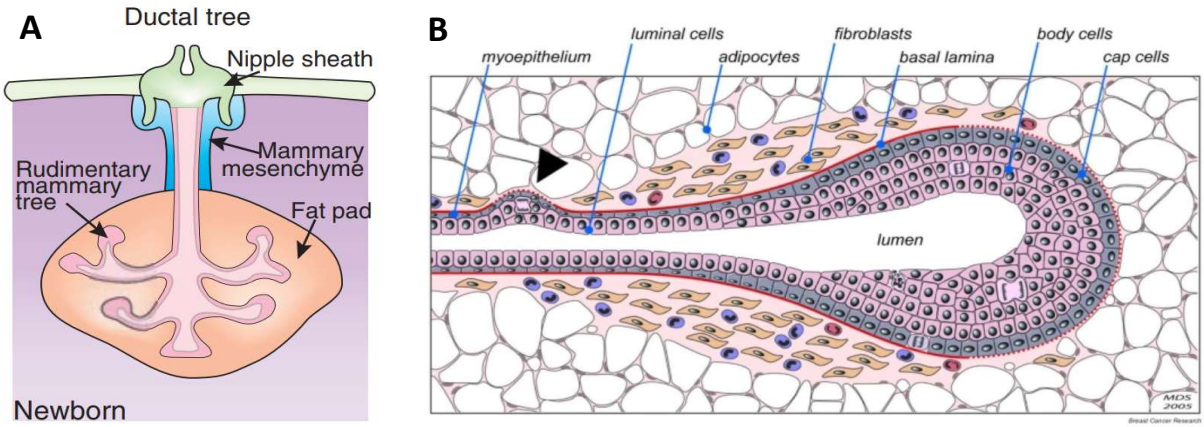

Figure 10: Mammary epithelium architecture during breast gland development. (A) Schematic of the breast epithelium architecture after birth. (B) Schematic of a TEB during mammary branching morphogenesis. Adapted from [118,119]

After branching morphogenesis is completed, the mammary epithelium resembles a tree-like structure of hollow ducts embedded into adipose tissue (Figure 11 A & B). During pregnancy, smaller milk-producing alveoli are formed that branch off the ducts. [122]. The alveoli exhibit a particular architecture (Figure 11 C) of a single-cell lining of luminal epithelial cells and basal myoepithelial cells around a hollow lumen. The epithelial cells are separated from the surrounding tissue, containing adipocytes and fibroblasts, by a BM [123]. The milk-producing luminal cells secret milk components into the hollow lumen of the structure. Contraction of the basal myoepithelial cells facilitates the generation of pressure, pushing the milk through the ducts toward the nipple [124]. After suckling has stopped, the gland undergoes involution, a process of controlled cell death (apoptosis) and ECM remodeling to restore the epithelium's pre-lactating architecture [125]. The transformation to a lactating gland and involution is repeated during every pregnancy. The mammary gland thereby undergoes the most dramatic naturally occurring organizational and morphological changes of adult human tissues.

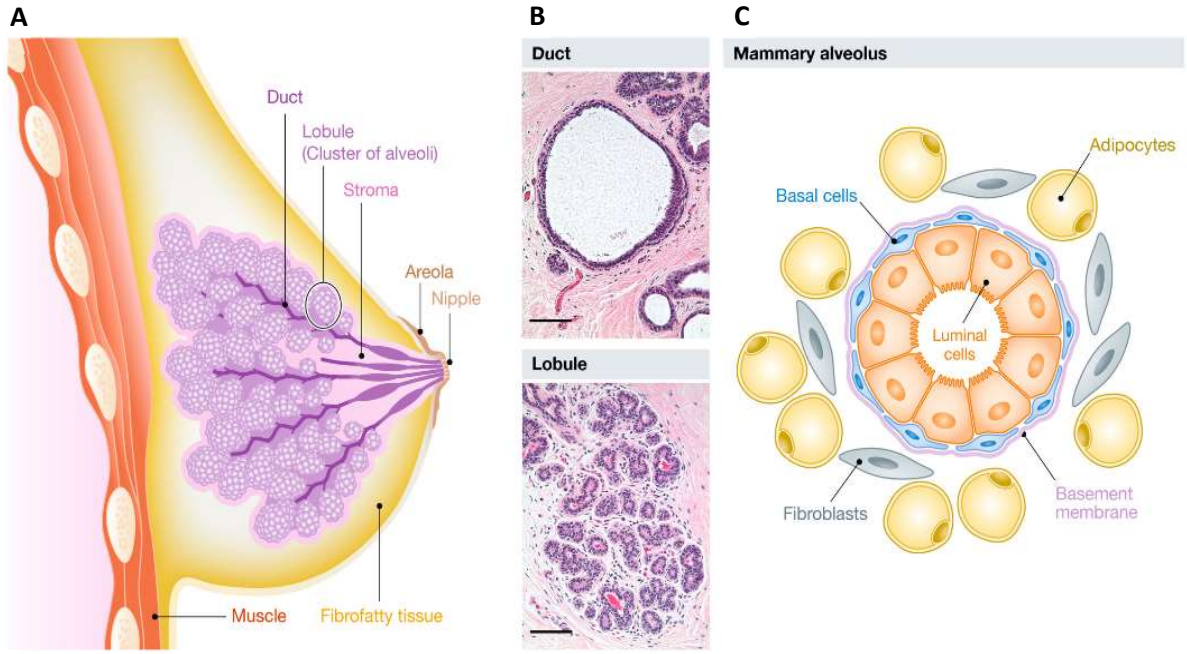

Figure 11 : Architecture of the adult female breast and embedded mammary epithelium. (A) The macroscopic structure of the human breast. (B) Histological sections of ducts and lobules. Scale bars = 100 µm (C) Schematic of mammary alveoli architecture. Adapted from [122]

Mammary gland development is mainly triggered by hormonal cues [118]. However, Fine control of cell migration, proliferation, and cell differentiation seems to be regulated by mechanosensory signaling pathways [120]. For example, the breast epithelial branching morphogenesis in mice was shown to be directed by ECM stiffness variations [126].

Accordingly, it has been demonstrated that branching directly depends on the integrin-mediated binding of laminin and proper downstream signaling [127]. Integrin-mediated cell adhesion to fibronectin on the other hand, was shown to be necessary for appropriate alveolar differentiation [128].

The adult breast tissue exhibits a tissue stiffness of ~170 Pa as measured by indentation [4]. This extremely soft tissue is subjected to constant external deformation, best described by shear deformation in solid objects. Haake and Surr measured this deformation by calculating nipple displacement and found that, during exercise, the strain rates reach up to 50% [15]. As epithelial cells are connected to their underlying ECM, this strain must also be transmitted to the mammary epithelial cells. How exactly the epithelium maintains normal tissue function under such stresses, even though it appears to be highly mechanically regulated, remains elusive.

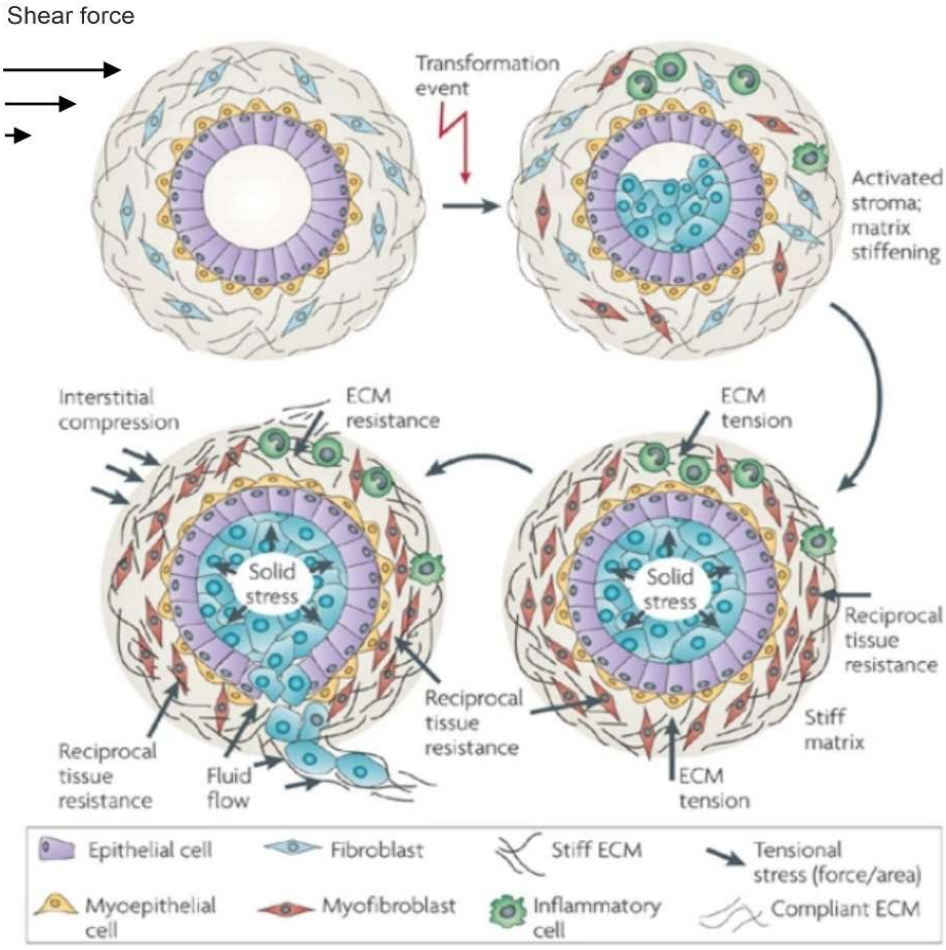

Figure 12: Dysregulation of the mechanical microenvironment of the mammary gland. Transformative events can turn healthy mammary epithelial cells into cancer cells. These proliferate and fill the lumen, creating a constant solid stress acting on the healthy epithelium. Fibroblasts of the stroma produce ECM proteins, stiffening the matrix and compress the ECM as myofibroblasts. Cancer cells ultimately invade through the BM surrounding the epithelium into the adjacent tissue. Adapted from [16]

Tumor development in the breast is often accompanied by reshaping of the tissue, drastically increased solid stress, ECM stiffness, and interstitial fluid pressure (figure 12) [129]. Mammary cells perceive these mechanical cues and react by increasing force generation and production of ECM components, further stiffening their environment in a process termed mechanic reciprocity [4,130,131]. This process fuels cancer cell malignancy which ultimately causes BM breaching and cancer metastasis.

Understanding how mechanical regulation is involved in normal tissue homeostasis and the malignant outcome of cancer is vital to developing effective clinical approaches to cancer treatment.

Mechanical regulation of breast cancer cells is directly linked to their proliferation, migratory behavior, and clinical outcome [132]. Here it appears that ECM compositions and cell-derived forces acting on the cells play significant roles in cancer cell behavior.

A higher breast tissue stiffness is associated with an increased risk of developing breast cancer [133]. Cancer cells can turn fibroblasts in their microenvironment into cancer-associated fibroblasts that secrete various factors, including ECM proteins and ECM crosslinkers resulting in substantial stiffening of the tumor surrounding matrix [134,135]. Thereby increased tumor tissue stiffness can reach up to 4049 ±938 Pa, which is why tumors are often palpable [4]. Both worse clinical outcomes and increases in integrin transcription have been found to be directly related to an increase in tumor stiffness [77,136].

In vitro experiments have further shown that cancer cells in general and breast cancer cells specifically drastically increase their force generation compared to non-malignant counterparts [137,138]. This effect might be caused or act independent of findings that suggest traction forces to increase based on substrate stiffness, as studies suggested this to be true only for normal breast epithelial cells but not cancer cells [139,140]. Therefore, the direct impact of a dysregulated microenvironment on cancer cell behavior is strongly indicated.

The beforementioned studies, however, were conducted utilizing 2D cell culture models, which often fail to mimic a physiologically relevant microenvironment. 3D cell culture models are often employed in vitro studies to gain more insight into tissue dynamics.

1.2.2 2D and 3D cell culture models

How exactly the mechanobiological regulation of breast epithelial cells is orchestrated remains elusive. To shed light on mechanical sensing and mechanotransduction processes involved in cellular regulation during mechanical homeostasis or dysregulation on a tissue scale requires sophisticated models.

In vitro experiments on mammalian cells date back more than 100 years [141]. Since then, thousands of cell lines have been established as models for various tissues, animals, and diseases. Cell lines such as the normal Michigan cancer foundation (MCF)10A cell line and the cancerous MCF7 cell line are immortalized [142]. They gained a mutation, either by chance or by manipulation, which allows them to divide continuously outside the body. While one must consider that such cells are not in every aspect identical to cells *in vivo*, they allow for investigations on simple-to-handle and mostly homogenous model cells. Characterization into normal and cancer cell lines is usually determined by the tissue of origin, therefore, healthy or tumor tissue. Cancer cell lines acquired additional mutations, while normal cell lines closely resemble physiological cells.

The MCF10A and MCF7 cell lines are common model systems for human breast epithelium [143–145]. As such, are they commonly used to compare reactions to, e.g., chemical stimuli of normal and cancerous cells or for investigations on what factors prompt normal cells to adopt a malignant phenotype [33,146]. These model systems were, for example, utilized to correlate local substrate stiffness with local traction forces via combined traction force microscopy (TFM) and scanning ion conductance microscopy [140].

Cell culture model systems grown on 2D substrates are often analyzed either as a single cell or in a continuous cell layer (Figure 13 A). While the latter allows for the formation of cell-cell contacts vital for force transmission in tissue, does this cultivation method not represent the *in vivo* situation of the breast gland. Mechanoregulatory processes of the breast gland and correct differentiation of mammary epithelial cells are implied to be reliant on hemidesmosomal integrin binding of BM components [76,120]. Mimicking typical breast epithelial cellular organization, therefore, requires the incorporation of a BM into cell culture model systems. This can be achieved by the cultivation of breast epithelial cell lines in natural 3D hydrogels.

Among others, 3D cell culture approaches were pioneered by Mina Bissel and co-workers, who investigated the influence of ECM composition on cellular behavior and morphology [130,147].

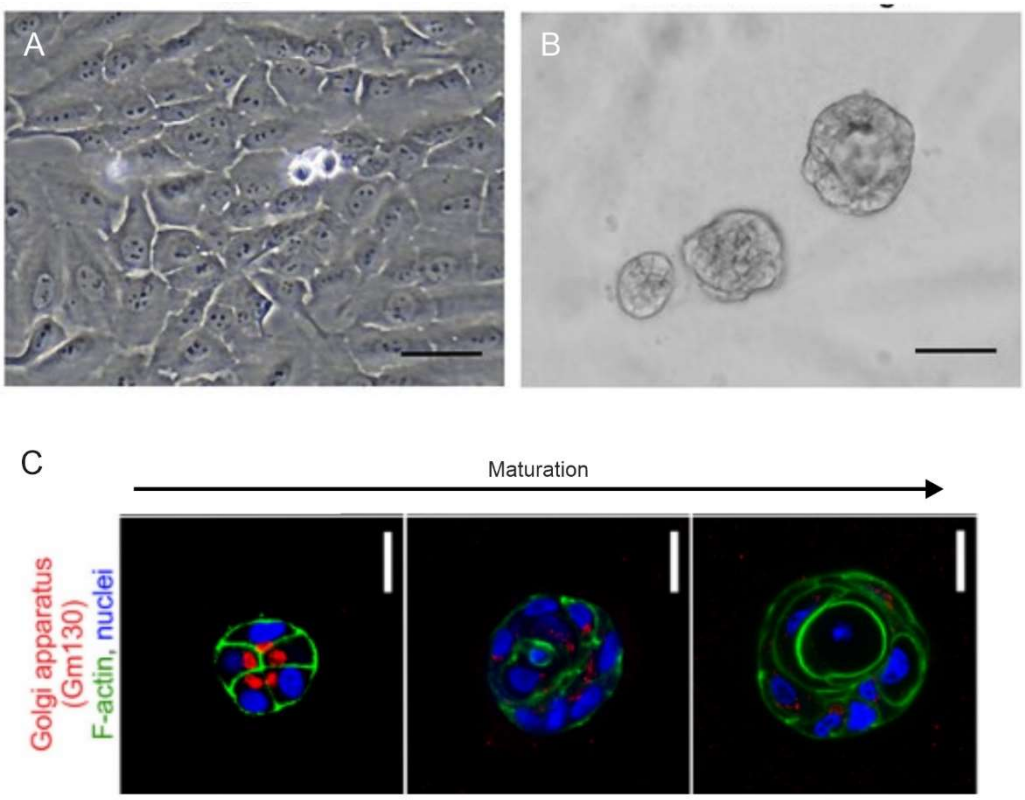

Figure 13: 2D and 3D cell culture methods. Bright field images of MCF10A cells cultured (A) on cell culture plastics form monolayers adopting a "cobblestone" morphology. (B) Cultured in 3D EHS-substrate derived gels, these cells form 3D spheroids. Scale bars = 100 µm (C) Spheroids generated via 3D cultivation undergo a progressive maturation which resembles breast epithelial differentiation. Scale bars = 20 µm. Adapted from [70,278]

Today, tissue or three-dimensional (3D) cell culture models are gaining more and more popularity in research on tissue scale cellular dynamics, especially in the past 20 years [148]. In contrast to 2D substrates, 3D models provide a much more natural environment for cells, allowing the formation of tissue-like cell-cell and cell-matrix adhesion for cells in matrices of tissue-like stiffness. Cells cultured in 3D hydrogels were found to provide characteristics that closely resemble their tissue of origin regarding normal morphology and differentiation, but also tumor cell migration and invasion [149].

3D cell culture methods rely on soft hydrogels to grow complex cellular constructs. For this, cells are usually maintained and propagated as a 2D culture (Figure 13 A) before they are detached and transferred to a hydrogel allowing for 3D morphogenesis (Figure 13 B & C). Commonly used hydrogels for 3D cell culture are, e.g., agarose, collagen I gels, gelatin, or Poly(ethylene glycol) (PEG) gels as a surrogate for natural ECM. Cancer cells cultivated in such

gels often form solid tumor-like cellular structures[150]. On the other hand, normal epithelial cell lines such as the canine-derived Martin-darby kidney cells produce spheroids with a hollow lumen and distinct cellular morphology as well as cell-cell contacts when cultured in collagen I-gels [151]. 3D cell culture techniques are used to analyze cellular behavior in tissue-like environments.

Artificial environment stiffening is often used to simulate tumor-like stiffening (for details, see chapter 1.3.1). Such analysis revealed that a stiffer matrix increases the invasion of cells from MCF7-derived breast cancer spheroids [152]. Recently, various 3D matrices with tuneable stiffness and defined matrix properties were developed, allowing for 3D cultivation of different cell lines in matrices that mimic their natural or tumor-like ECM or allow for specific biocomponent modification to facilitate integrin binding [153]. Modulation of integrin binding sites, and thereby alteration of cell-ECM interactions, are an especially useful tool for investigations on cellular differentiation as cells were observed to exhibit distinct morphological features based on the matrix they were placed in. Evidence suggests that specific matrix components are, independent of matrix stiffness, necessary for polarization of EpH4 mammary epithelial cells as they acinar structures in Matrigel but not collagen I gel [154].

3D cell culture models allow for fascinating possibilities to study how cells integrate stiffness, complex forces, and integrin binding to their ECM into cellular behavior and differentiation. Further, do 3D cell culture techniques allow for studies on breast epithelial-derived cells which mimic natural differentiation. Thereby are such models excellent candidates for investigations on breast tissue dynamics.

1.2.3 Modeling the mammary gland morphogenesis *in vitro*

MCF10A-derived spheroids are one of the most common models for normal breast epithelium. Controlled cell culture conditions allow for the generation of well-defined spheroids (acini) from single MCF10A cells, which closely resemble the *in vivo* architecture of breast gland alveoli, including a BM, polarized cells and a hollow lumen (Figure 14 A). For this, natural ECM surrogates derived from Engelbreth-Holme-Swarm (EHS) mouse sarcoma substrates (commercially available as Matrigel or Geltrex) are utilized. EHS-substrates are mainly composed of laminins, collagen IV, heparin sulfate proteoglycan perlecan and entactin provide and provide cells with a natural ECM which allows for the growth of normal breast epithelial spheroids in a physiologically relevant environment [155].

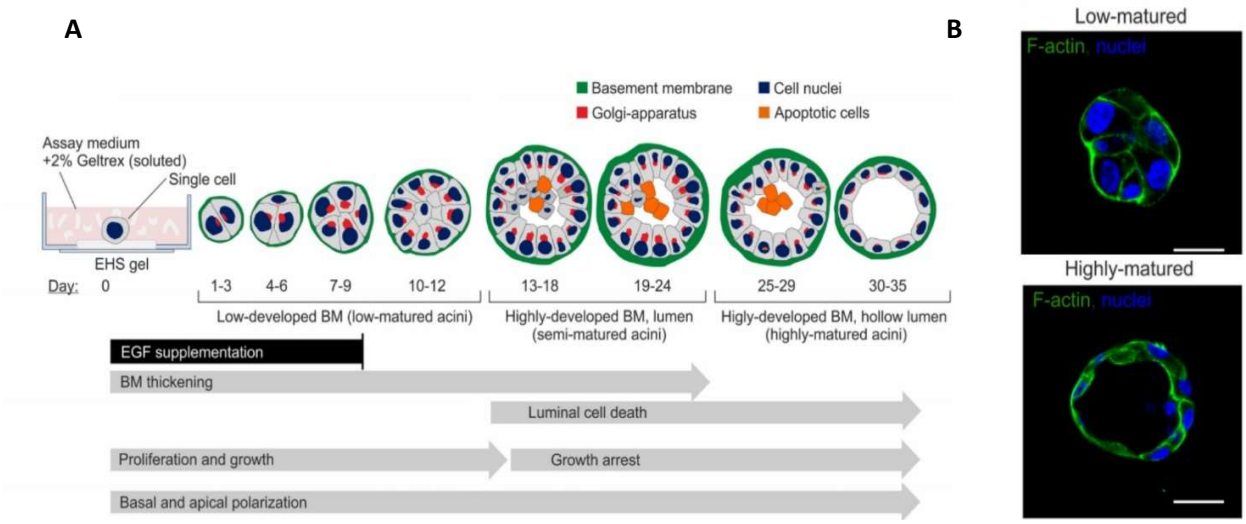

Figure 14: The MCF10A spheroid development. (A) MCF10A cells undergo a defined spheroidal development when cultured in EHS-gel. EGF supplementation in the first 9 days of cultivation promotes cell division and spheroid formation. After growth arrest, a lumen is formed by apoptotic cell death of central cells. A BM starts forming at day one. The outer cell layer increasingly basoapical polarizes as indicated by intracellular basal orientation of nuclei and apical orientation of the golgi apparatus. (B) Micrographs of a low-matured and highly-matured MCF10A spheroid. Adapted from [70]

By control of growth factor concentration can the development and behavior of these spheroids be further controlled to resemble normal breast epithelial structure or produce cancer cell-like invasion events (Figure 14 A) [33,70]. The development of MCF10A spheroids is described by an initial proliferation stage (< day 13) and subsequent growth arrest combined with luminal cell death (> day13). Further characterization revealed that the BM covering the spheroids is progressively stiffening and thickening throughout this development [72]. Another important morphological factor of epithelial differentiation *in vivo* is cellular polarization, the orientation of cellular organelles, cell-cell, and cell-matrix contacts [156–158]. MCF10A spheroids display a gradual increase of basoapical polarization, defined by the orientation of the nucleus and Golgi apparatus towards the BM, thereby exhibiting epithelial differentiation morphologically. Fully developed MCF10A spheroids closely imitate the natural architecture of the alveolar breast gland epithelium (Figure 14 B), thus constituting an excellent model system to investigate its mechanobiological regulation. Especially the formation of a BM is a remarkable feature missing in most 3D cell culture models. The BM provides cells with a natural epithelial ECM that allows for HD and FA formation. Further allows the presence of a BM for investigations on BM breaching during cancer cell invasion. For example, were tumor-like stiffness and growth factor stimulation used to trigger aberrant cancer cell-like behavior in originally non-invasive MCF10A spheroids. BM breaching events were only partially

dependent on MMPs and were mostly driven by increased force generation of cells as measured by traction force microscopy [33]. Simultaneously, the BM was shown to act as a mechanical barrier where high-developed BMs delayed cell invasion. Such investigations underline the relevance of the MCF10A model for studies on normal breast epithelium and breast cancer cell behavior in response to mechanical cues. Further, it is implied that otherwise normal and differentiated breast epithelium alters their behavior in response to aberrant mechanical and biochemical cues.

Ultimately, can no cell culture model perfectly mimics the natural cell-environment niche. Nevertheless, MCF10A breast spheroids recapitulate essential morphological features of natural breast epithelia. Most importantly, a BM and differentiated epithelium. Therefore they represent a physiologically relevant model to study mechanobiological regulation circuits in breast epithelial development and homeostasis on a tissue scale. Hence, this model has been used for all subsequent experiments present in this work.

1.3 *In vitro* approaches to model mechanoresponses

Analysis of cellular mechanoregulation often relies on the stimulation of cells and cell clusters with physiological mechanical cues. Most commonly investigated are cellular responses to alteration of the substrate and ECM stiffness, measurement of cellular forces, and morphological adaption to external mechanical stresses, as well as combinatory approaches to analyze potential synergistic effects. Many tools are available to conduct such experiments using 2D cell culture models on planar substrates or within hydrogels. In contrast, there is a lack of tools to perform experiments utilizing 3D cell culture models that interact with 3D ECM surrogates

1.3.1 Substrate stiffness modulates cellular behavior

Substrate stiffness has various effects on cellular morphology, differentiation, and motility. Also integral to this response is the composition of the underlying substrate. Investigations on three glioblastoma cell lines (LBC3, LN229, LN18) revealed that the cells react to substrate stiffness with a spread morphology, increased motility and increased force generation [159]. The specific cellular reactions to stiffness depended on integrin binding sites on the substrates and cell line origin. Thereby implied was the relevance of cellular integrin expression patterns, which depend on cellular differentiation. [160]3D cell culture models are getting more attention and various approaches were developed to investigate cellular responses to matrix stiffening using 3D cell culture models. Several studies found MCF10A spheroids to adopt cancer cell

traits and undergo EMT when cultured in stiff 3D matrices (1.5-5 kPa) [4,161–163]. MCF10A cell reacted to stiffness increase to mimic the maximal mammographic density of normal breast tissue with a significant increase in expression levels of ERBB2, a growth factor receptor that is often overexpressed in tumors[163,164]. Thereby highlighted is the importance of mechanosensing for normal non-transformed mammary epithelial cells. In accordance with 2D experiments, were MDA-MB-231 and MCF10A cells found to display different morphology and surface receptor exposition in response to cultivation in hydrogels either composed of collagen I, EHS-substrate, or tissue matrix gel produced from decellularized mouse breast tissue [165]. These gels, however, are not only differing in stiffness but also in adhesion site composition. To untangle collective mechanoresponses to stiffness and integrin binding sites, tuneable synthetic hydrogels are frequently employed as 3D matrices, allowing for the adaption of specific characteristics. For example, synthetic PEG or polyacrylamide hydrogels are employed that allow for independent stiffness tuning via crosslinking agent concentration or precursor modification [166,167]. Specialized approaches even allow for gradual stiffness tuning after gelation by magnetic straining or light-induced crosslinking [168,169]. These systems allow for the simulation of gradual substrate stiffening during tumor development. As such, they were utilized in analyzing mammary carcinoma drug resistance or morphological adaption of fibroblasts to a stiffening microenvironment.

Modulation of adhesion site composition in synthetic gels is also of interest. Synthetic gels can be modified with the fibronectin-derived integrin binding peptide commonly referred to as RDG-sequence [170,171]. Synthetic hydrogels allowing for degradability by MMPs or by cell-derived forces have been further used to investigate cellular matrix remodeling [172,173]. Such approaches only now unravel the detailed stiffness, adhesion sites and remodeling capacities that an *in vitro* ECM surrogate must provide to allow for specific development and differentiation of physiological breast epithelial spheroids *in vitro* [174].

Therefore, are models such as MCF10A spheroids still reliant on EHS-substrates and their specific stiffness and adhesions site composition to facilitate basoapical polarized and BM-forming physiologically relevant 3D cell culture models with natural epithelial differentiation.

1.3.2 Traction force microscopy

Cells use actomyosin structures to generate contractile forces. These forces are applied to the ECM via focal adhesions or neighboring cells via adherens junctions. To understand how cells modify actomyosin contraction in dependence of substrate stiffness, integrin binding sites or

cellular differentiation status, it is necessary to measure these forces quantitatively. This is facilitated by traction force microscopy (TFM), which utilizes high-resolution microscopy to determine cell force-generated substrate deformations. The most common approach to TFM employs tracking of deformations in elastic substrates by measuring the displacement of fluorescently labeled microspheres either placed on top of or embedded into the substrate (Figure 15 A-D)[175–178]. Considering the mechanical properties of the substrate, i.e., poly dimethyl siloxane (PDMS) based silicone rubber, it is possible to reconstruct the cell-derived forces that generated local substrate deformations (Figure 15 E & F).

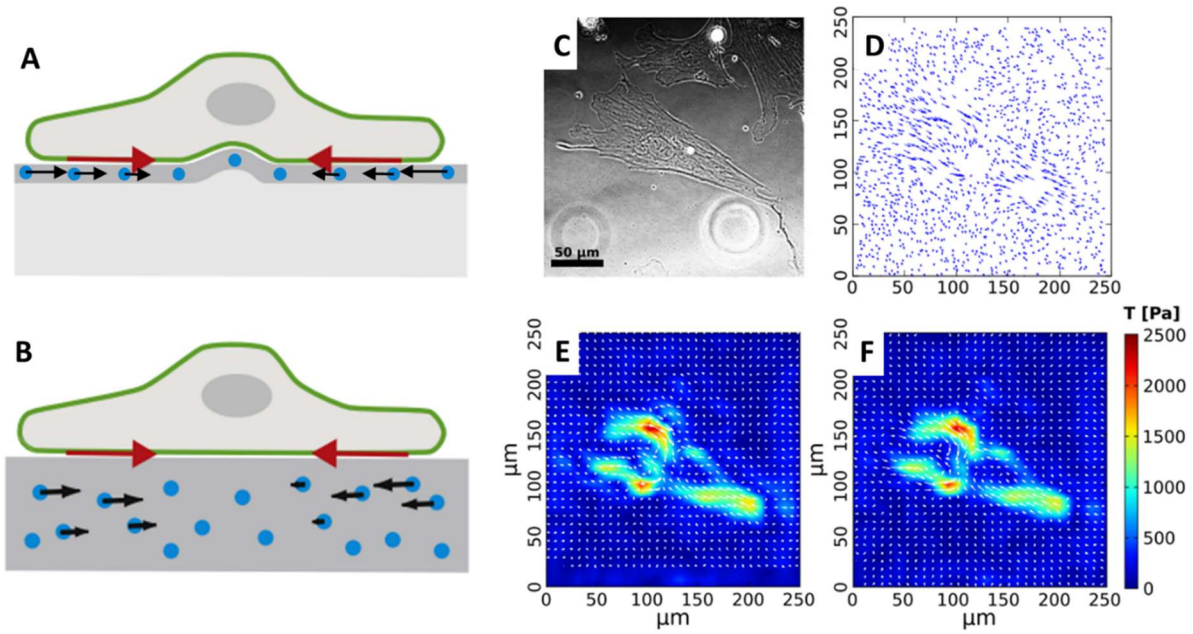

Figure 15: Principle of traction force microscopy. (A) Fluorescent microspheres are placed on top of an elastic matrix (B) or are embedded. Deformation of the matrix by cellular movement displaces the microspheres. (C) Phase contrast image of cardiac myofibroblast on a poly dimethyl siloxane (PDMS) based silicone rubber substrate with an elastic modulus of 15 kPa. (D) Displacement vectors of microspheres resulting from cellular movement of B. (E) Traction force reconstruction via regularized Fourier transform traction cytometry. (F) Finite element method-based traction force reconstruction. T = tractions (force per area). Adapted from [175]

The utilization of TFM revealed functional coupling of substrate stiffness and cellular force generation. For example, the cellular force generation of breast cancer cells is increased compared to normal cells [138]. Further is cell-derived force generation modified by substrate adhesion sites [175,179]. Thereby implied is that substrate stiffening in tumors leads to more force generation of cancer cells.

Accordingly, TFM measurements on MCF10A breast spheroids placed on elastomer substrates have shown that cellular force generation under tumor conditions was increased [33]. Further could be shown that force generation directly correlates with invasive breaching of the BM and transmigration of cells onto the 2D silicone substrate (Figure 16). It is clear that TFM is a valuable tool for investigations on cellular-derived forces, which have vital implications for tumor development.

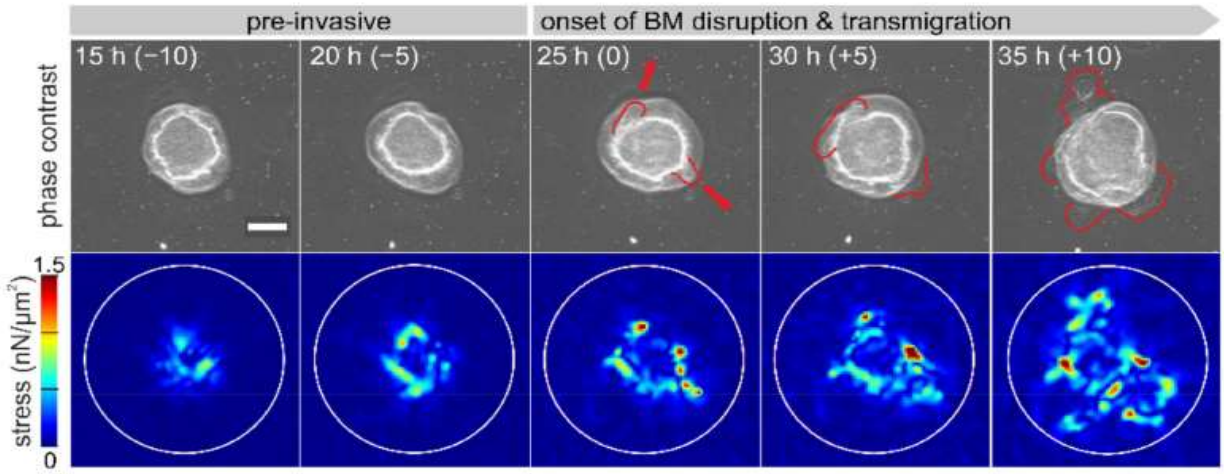

Figure 16: TFM of MCF10A spheroid invasion on 2D elastomeric substrates. Phase images and corresponding strain energy maps of MCF10A spheroids before, during, and after BM breaching. Ref arrows indicate BM invasion location. Red outlines indicate invasive cells. Scale bars = 20 µm. Adapted from [33]

The two-dimensionality of TFM, however, does not allow for the analysis of cell-derived forces in a natural, tissue-like 3D environment. To fully comprehend how cell forces are modified *in vivo* and how they affect normal and cancer cells in the breast tissue, it is necessary to switch from 2D to 3D cell culture models.

A notable approach to this is, for example, 3D TF-optical coherence microscopy (OCM) [180]. TF-OCM however, relies on tracking of relatively large microspheres (1 µm) with large spacing (18 µm), which limits resolution capacity. The 3D TFM approach proposed by the group Christopher Chen relies on confocal microscopy and allows for better resolution is however still relying on 2D substrates [181]. The group of Ben Fabry realized 3D TFM to measure force generation of invading breast carcinoma cells [182]. Their approach is quick to compute but relies on a simplification of the deformed matrix´ mechanical properties, assuming it to be linearly elastic and not considering strain stiffening effects.

An approach to reliably determine cellular force generation in a 3D matrix suitable for studies on breast epithelial spheroids is still missing.

1.3.3 Cellular reactions to dynamic mechanical stresses

Many tissues experience mechanical stress regularly. The epithelium lining outside the lung experiences up to 110% strain during breathing [183]. The heart experiences up to 50% strain during pumping [184]. Blood pressure variations cause pulsating arterial expansion, leading to strains of up to 3.7% in the brain [185]. Endothelial cells lining the inside of blood vessels experience near-permanent fluid shear stress. Many studies focus on mimicking these stresses to understand how they affect cellular behavior and contribute to normal tissue homeostasis.

There is a plethora of cell stretching devices, allowing for uniaxial cyclic stress application to cells cultivated on elastomeric substrates [186–189]. When stressed with such a device, cardiomyocytes derived from the heart or fibroblasts originating from the skin reorient their cytoskeleton perpendicular to the strain axis, thereby best avoiding the stress [178,190]. Neuronal stem cells in a similar setup, however, orient parallel to stress direction [191]. Further was shown that such reactions depend on the frequency, amplitude of applied strain and the duration of stress exposure [178,192,193]. Cellular reactions to cyclic strain depend on the cell type and, therefore, the tissue of origin. Thus are cellular mechanoresponses dependent on cellular differentiation.

Specific types of stress can also trigger differentiation. To mimic blood flow *in vitro*, several cell culture-compatible microfluidic devices were developed [194–198]. The application of fluid shear stress was shown to differentiate stem cells into endothelial cells, which *in vivo* line the inner wall of blood vessels [199–202]. Thus, mechanical stress can lead to cytoskeletal reorganization and is an essential stimulus for shaping cell fate. Mechanical stresses are native to all cells and tissues and actively steer cell-type specific responses and adaptations. Further, dynamic extracellular mechanical stresses that act on cells are essential drivers of tissue development [203].

Even though the breast tissue experiences dynamic strains during body motion [14,15], little is known about the effects of such high strains on the mammary epithelium. This is primarily due to a lack of tools. The breast gland experiences, as a tissue, what is best described as shear strain. To best mimic the breast gland tissue strain, it would be necessary to apply mechanical shear strain to breast epithelial spheroids in a natural matrix. Of note, suitable tools that would accomplish this important task remained missing.

1.4 Aim of this work

The breast gland is a complex tissue that undergoes massive remodeling even after adulthood is reached. Additionally, is the mammary epithelium permanently subjected to internal and external forces. Such mechanical cues, together with cell-cell and cell-ECM adhesions, orchestrate the mechanobiological regulation processes that modulate cytoskeletal organization and morphology, motility and cell force generation, proliferation and differentiation. All these processes are essential for normal tissue homeostasis. This is especially evident in tumor development, where reciprocal dysregulation of the mechanical microenvironment fuel cancer cell aggressiveness and, finally, BM breaching and metastasis. Understanding how breast tissue integrates mechanical signaling processes into normal behavior is key to understanding how dysregulation promotes breast cancer progression.

This work aims to investigate how naturally occurring solid shear stress is involved in the development and normal behavior of breast epithelial cells. Of special interest was how the naturally occurring shear forces acting on the epithelium are interpreted on a cellular level. As an *in vitro* approach to this question, MCF10A spheroids embedded in a natural matrix should be cyclically shear strained while simultaneously observing cellular responses. Also, should the cellular response to matrix stiffening in a physiological context be investigated. For this should spheroid-derived 3D matrix deformations be analyzed in hydrogels of varying stiffness.

A novel device was constructed to analyze the mechanoresponse of breast epithelial spheroids to physiological solid shear stresses. The device should be optimized and strain production characterized to enable reproducible defined stress application under optimal cell culture conditions. Cellular reactions should be captured with confocal live cell imaging of actin dynamics to allow direct evaluation of cell motility, morphology, and spheroidal integrity. To investigate the role of mammary epithelium development, should this analysis also be done in regard to the maturation state of MCF10A spheroids. Any observed mechanoresponse should be further examined concerning its molecular mechanosensing components. The goal was to shed light on how external force application affects normal breast gland epithelium.

No tool was available to investigate spheroid-derived forces in 3D matrices in response to stiffness alterations. Therefore, a novel approach should be developed to track fluorescent

microspheres in 3D matrices of tunable stiffness using confocal microscopy. This approach should then be used to analyze the response of breast spheroids to tissue stiffening.

Ultimately, was the aim of this work to better the understanding of the mechanobiological regulations in the breast gland and

2 Materials & Methods

2.1 Instruments

Table 1: Instruments.

Instrument	**Manufacturer**
Arium Pro	Sartorius, Göttingen
Axiovert 40 CFL Mikroscop e	Carl Zeiss, Jena
Axio Vert.A1	Carl Zeiss, Jena
Binokular Stemi 2000-CS	Carl Zeiss, Jena
Stemi 508	Carl Zeiss, Jena
Cryo 1 °C Freezing Container (Mr. Frosty)	Thermo Scientific, Braunschweig
Heating block SBH130D	Stuart/ Cole-Parmer, Stone, VA
Heracell Incubator	Thermo Fisher, Waltham, USA (MA)
Incubator XL	Carl Zeiss, Jena
JB1603-C/FACT Caratscale	Mettler Toledo, Gießen
Laserscanning Mikroscope 880 + Airy Scan	Carl Zeiss, Jena
MilliQ Gradient A10	Merck, Darmstadt
pH-Meter 766 Calimatic	Knick, Berlin
Plasmaoven Pico	Diener Electronics, Ebhausen
Mercury-vapor lamp HXP120	Carl Zeiss, Jena
Rocker 2D	IKA, Bremen
Sigma 3-16L Centrifuge	Sigma Laborzentrifugen GmbH, Osterode am Harz
Cleanbench (Herasafe KS)	Thermo Fisher, Waltham, USA (MA)
Vortex REAX top	Heidolph, Schwabach
Heating cabinet	Memmert, Schwabach
Waterbath WB22	Memmert, Schwabach
Cell counter Moxi-Z-mini	Orflo, Ketchum, USA (Idaho)
Centrifuge 5415R	Eppendorf, Wesseling
Shear stress device parts	
Linear motor stage 24x29x65 Sonder Pico	Steinmeyer-Mechatronik
Motor control unit	Self-constructed at the FZJ
3D printed parts	Self-constructed at the FZJ
Aluminum parts	Self-constructed at the FZJ
Lenovo Flex 10 netbook	Lenovo
Bowden cable, stainless steel, Teflon sheath	Online Bowdenzug 24.de
Radial ball bearing DIN 625	Mädler
1 mm cubic NdFeB N45, Ni-Cu-Ni coating	Webcraft, Gottmadingen, Germany
30 x 10 x 5 mm cuboid NdFeB N42, Ni-Cu-Ni coating	Webcraft, Gottmadingen, Germany
TG165-X Spot Thermal Camera + Diode	FLIR

2.2 Materials

Table 2: Materials.

Materials	Manufacturer
Acrodisc Syringe 25 mm/0,1 µm Filter	Pall Corporation, Dreieich
Cover glasses, #0, #00, #1,5 #1,5 HP 22 x 22 mm	Menzel, Braunschweig
One way-Stripettes, 5 ml, 10 ml, 50 ml	VWR, Darmstadt
Falcon-Reactiontubes (15 und 50 ml)	BD Biosciences, San Jose, Kalifornien, USA
Kimtech Science precision wipes	Kimberly-Clark Professional, Koblenz
Kryotubes	VWR, Darmstadt
Lochschale, ø 35 mm mit ø 18 mm Loch	Greiner Bio-one, Frickenhausen
Moxi Z Cassete type S	Orflo Technologies, Hailey, Idaho, USA
Petrisdishes	VWR, Darmstadt
Pipette tips(10 µl, 200 µl, 1000 µl)	Star Lab, Hamburg
Research Plus Pipettes (10, 200 and 1000 µl Volume)	Eppendorf, Wesseling
Protein LoBind Tubes (1,5 and 2 ml)	Eppendorf, Wesseling
Reaction tubes (0.2; 0.5; 1.5 and 2 ml)	Eppendorf, Wesseling
Weighing pan (div. Sizes)	VWR, Darmstadt
Cell culture bottles, 25 cm^2 und 75 cm^2	BD Biosciences, San Jose, Kalifornien USA
Titanium mesh TI008710 100 x100 mm	Goodfellow

2.3 Compounds and Reagents

Table 3:Compounds and reagents.

Compound/Reagent	Manufacturer
(D)-Glukose	Sigma Aldrich, München
AffiniPure Goat F(ab')2 Fragment	Jackson ImmunoResearch, West Grove, USA (Pennsylvania)
Bovines Serum Albumin (BSA)	Merck, Darmstadt
Choleratoxin from *Vibrio Cholerae*	Sigma Aldrich, München
Corning® Cell Recovery Solution	BD Biosciences, San Jose, Kalifornien USA
Cryo-SFM	PromoCell GmbH, Heidelberg
Dextran von Leuconostoc spp. (Mr 70,000)	Sigma Aldrich, München
Dimethylsulfoxid (DMSO)	Sigma Aldrich, München
Disodiumhydrogenphosphat (Na_2HPO_4 *12 H_2O) (Dodecahydrat)	Sigma Aldrich, München
DRAQ5	Cell Signaling, Danvers, Massachusetts, USA
Epidermal growth factor (EGF)	Sigma Aldrich, München
Acetic acid	Merck, Darmstadt
Ethanol (reciprocated 97% und absolut)	Merck, Darmstadt
Ethylenglycol-bis(aminoethylether)-N,N,N',N'-tetraacetic acid (EGTA)	Sigma Aldrich, München
FluoSpheres® carboxylate microspheres 0,2 µm (660/680)	Thermo Fisher, Waltham, Massachusetts, USA
GeltrexTM LDEV-Free Reduced Growth Factor Basement Membrane Matrix LOT:2327547 (17.5 mg/mL) LOT: 2327543 (15.8 mg/mL) LOT: 2248602 (16 mg/mL)	Thermo Fisher, Waltham, Massachusetts, USA
Glutaraldehyd, 25% (EM Grade)	Ted Pella, Inc., Redding, Kalifornien, USA
Glycin	Sigma Aldrich, München
Hydrocortisol	Sigma Aldrich, München
Immersionsoils for objektives	Carl Zeiss, Jena
Insulin (30ecombinant)	Sigma Aldrich, München
Isopropanol	Promochem, Wesel
Potasstiumdihydrogenphosphat (KH2PO4)	Sigma Aldrich, München
Magnesiumchlorid (MgCl2)	Sigma Aldrich, München
Methanol	Merck, Darmstadt
Milk powder	Carl Roth, Karlsruhe
Sodiumborhydrid (NaBH4)	Merck, Darmstadt
Sodiumchlorid (NaCl)	Sigma Aldrich, München
NucBlue™ Fixed Cell ReadyProbes™ Reagent (DAPI)	Thermo Fisher, Waltham, Massachusetts, USA
Penicillin-Streptomycin (10000 U/ml)	Sigma Aldrich, München
Horse serum (hitzeinaktiviert)	Thermo Fisher, Waltham, Massachusetts, USA
Sylgard® 184 Silcone Elastomer Kit	Dow Corning, Wiesbaden
Tris(hydroxymethyl)aminomethane (Tris Base)	Sigma Aldrich, München

TritonTM X-100	Sigma Aldrich, München
Trypsin/EDTA Phenolrot 0.05%	Thermo Fisher, Waltham, Massachusetts, USA
Gadoliunium(III)chloride hexahydrate	Sigma Aldrich, München
Tween® 20	Sigma Aldrich, München
Texas red conjugated dextran tracer solution 200 µg mL-1, Ex/Em = 585/905 nm,	Life Technologies

2.4 Solutions, Buffers and Media

Table 4: Solutions, buffers and Media.

Solution/Buffer/Medium	**Manufacturer/Components**
Blocking solution for immunofluorescence	5 % Milk powder in CB- Buffer
Cryo-SFM	PromoCell, Heidelberg
DMEM/F-12 (1x)(1:1) GlutaMAX	Life Technologies, Darmstadt
Fixation solution for spheroids in EHS-gels	2 % Formaldehyd 1% Glutaraldehyd in CB-Buffer
Fixation solution for transferred spheroids	3,7% Formaldehyd in CB-Buffer
Glycin-Solution	30 mM Glycin in CB-Buffer
Permeabilisation-solution	0,01 % Triton-X-100 in CB-Puffer
Phosphate buffered salt solution (PBS) (pH 7,4)	Thermo Fisher, Waltham, Massachusetts, USA
Phosphate buffered salt solution (PBS) (pH 7,4)	15,5 mM NaCl 0,105 mM KH2PO4 0,297 mM Na2HPO4 *12 H2O
Quenching-Solution	1 % Sodium boron hydrid in CB-Puffer
Dilution buffer	1 % Milchpulver in CB-Puffer
Cytoskeleton-Buffer (CB-Puffer), pH 6,1	150 mM NaCl 5 mM MgCl2 5 mM EGTA 5 mM Glucose 10 mM MES 1 g/l Streptomycin
$GdCl_3$ – solution (10 mM)	0,04 g Gadoliunium chloride Hexahydrate 10.75 mL Milli-Q H_2O
2-[4-(2-Hydroxyethyl)piperazin-1-yl] ethane-1-sulfonic acid (HEPES), 1 M	ThermoFisher Scientific
10 kDa Dextran Texas red conjugated (Em/Ex = 585/905 nm; 10.000 µg/mL)	Life Technologies

2.5 Primary antibodies

Table 5: Primary antibodies.

Epitope	Origin	Producer	Clone/ Ordering number
GM 130	Mouse	BD Biosciences, Franklin Lakes New Jersey, USA	BD 610822 / 35-GM130
Collagen IV	Rabbit	Abcam, Cambridge, UK	Ab6586
Cleaved Capsase-3	Rabbit	Cell Signaling Technology, Danvers, Massachusetts, USA	9661S
Piezo1	Rabbit	Novus Biologicals	NP1-78446

2.6 Secondary antibodies

Table 6: Secondary antibodies

Isotype	Donor	Fluorescent dye	Producer: (Ordering number)
Rabbit	Chicken	Alexa 488	Invitrogen, Karlsruhe (A21441)
Rabbit	Goat	Alexa 405	Invitrogen, Karlsruhe (A32556)
Mouse	Donkey	Alexa 488	Invitrogen, Karlsruhe (A21202)

2.7 Fluorescent dyes

Table 7: Fluorescent dyes.

Product	Target	Producer (Ordering number)
DRAQ5	Nuclei (DNA)	Thermo Fisher, Waltham, Massachusetts, USA (62251)
NucBlue (4’,6-Diamidin-2-Phenylindol (DAPI))	Nuclei (DNA)	Thermo Fisher, Waltham, Massachusetts, USA (R37606)

2.8 Commercial Software

Table 8: Commercial software.

Software	Producer
Corel Draw Version 2019 (21)	Corel, Munich
Imaris 9.4	Bitplane, Zurich, Switzerland
ImageJ	National Institute of Health, Bethesda, USA (MD)
MatLab 9.0	MathWorks, Natick, USA (MA)
Python 3	Python Software Foundation, Wilmington, USA (NC)
ZEN 2.3 blue edition	Carl Zeiss, Jena
ZEN black 8.0	Carl Zeiss, Jena
Microsoft office (Excel, Word & Powerpoint)	Microsoft, Redmond, WA, USA

2.9 Cell culture methods

All cell culture methods were performed under a sterile clean bench. Cells were regularly tested for mycoplasma contamination and kept in a cell culture incubator at 37°C in a humidified environment with 5% CO_2 if not stated otherwise. All solutions used with living cells were (Media, PBS, Trypsin) preheated to 37°C in a water bath before use if not stated otherwise. The MCF10A wildtype cell line was obtained from the american type culture collection (ATCC, Manassas, Virginia, USA), while the MCF10A LiveAct-RFP variant was produced by Dr. Erik Noetzel-Reiss, Dr. Lisann Esser and Dr. Aljona Gaiko-Shcherback (all IBI-2, FZJ). 3D cultivation of MCF10A spheroids was based on the work of Dr. Aljona Gaiko-Shcherback, who optimized cultivation protocols and characterized a defined spheroidal developmental schedule [70,155]. Cell counting was performed by pipetting 75 µL of cell suspension onto a Moxi Z cassette type S, which was placed into a Moxi-Z mini. The Moxi-Z mini cell counter then calculated cell number and size, excluding cell aggregates, dead cells or debris with 95% accuracy.

Table 9: Cell culture media composition for MCF10A cultivation.

Components	Growth media (GM)	Assay-Medium with EGF (AM+)	Assay-Medium without EGF (AM-)
Hydrocortisone	0,5 µg/ml	0,5 µg/ml	0,5 µg/ml
Penicillin/Streptomycin	1 %	1 %	1 %
Insulin	10 µg/ml	10 µg/ml	10 µg/ml
EGF	20 ng/ml	5 ng/ml	-
Cholera Toxin	100 ng/ml	1 ng/ml	1 ng/ml
Horse serum	5 %	2 %	2 %

2.9.1 Thawing of cells from cryo storage

Thawing cells was done by placing cell solution containing cryo tubes into a 37°C water bath until a liquid phase formed. To the cell solution was then quickly added 4 mL of GM, pipetting gently up and down to thaw any remaining ice. The cell solution was then centrifuged at 120 g for 5 min, the supernatant was disposed and the cell pellet was gently resuspended in 6 mL GM. The resulting cell solution was finally completely transferred into a 25 cm^2 cell culture flask which was placed into a humidified cell culture incubator with 5% CO_2 at 37°C until cell confluency reached 80-90% (~2 days) and cells were passaged.

2.9.2 Cell maintenance and passaging

Cells were passaged in 25 cm^2 cell culture plastic flasks. At 80-90% confluency (3-4 days after seeding), cells were passaged into a new cell culture flask. For this, cells were first washed twice with warm (37°C) PBS twice, carefully washing away the media and remnant cell debris. Cells were then treated with 0.05% Trypsin solution for detachment of cells from the cell culture plastic. The solution was distributed across the cells by swirling before incubation in a humidified incubator at 37°C for 10-13 minutes, depending on the confluency of the cells. Detachment of cells was expedited by careful knocking on the cell culture flask to reduce stress due to media starvation. The cell-trypsin solution was mixed with 4.5 mL GM to stop trypsin activity before cell number was determined with a cell counter Moxi-Z-mini and a Moxi-cassette type S. Cell counting was performed with 75 µL of cell suspension. At this point, 15000 were transferred into 3 ml AM+ for 3D spheroid cultivation before centrifuging the mixture(s) at 120 g for 5 min to pellet the cells and disposal of trypsin-containing media. After disposing of the supernatant, the cell pellet was suspended in 5 mL of GM. 6 mL GM was placed into a cell culture flask before adding 100.000 to 120.000 cells into the flask and swirling the media in an “8” motion to distribute the cells homogeneously and avoid clumping. Cells were then cultivated for 3 to 4 days before confluency of 80-90% was reached and cells were passaged again.

2.9.3 Preparation for cryostorage of cells

For long-term storage, cells were suspended in specialized media, frozen and stored in liquid nitrogen. Cells cultivated as described in 2.9.2 were detached with trypsin, suspended, counted and centrifuged. After dispensing the supernatant, Cryo-SFM medium was used to resuspend the cell pellet. The amount of Cryo-SFM used was calculated to give a final cell concentration of 500.000-1.000.000 cells/mL. Corresponding amounts of Cryotubes were

filled with 1 mL of this cell suspension and placed in a Mr. Frosty cell freezing container. The container was filled to the mark with 97% isopropanol and placed into a -80°C freezer to ensure even cooldown and freezing of the cell solution. After at least 14h in the freezer, the tubes were transferred to liquid nitrogen-filled tanks for indefinite storage.

2.9.4 3D cell culture

For 3D cultivation of MCF10A spheroids, single cells were seeded in between two layers of EHS-derived hydrogels. The EHS substrate was stored at -80°C and thawed overnight at 0°C before aliquoting. EHS-substrate was then stored at 4 °C and used within 4 weeks after thawing. To do so, 100 µL of ice-cold EHS substrate was pipetted carefully into the inner well of a 35 mm cell culture dish with a #0 cover glass bottom plate. The dish was cooled for at least 1 min on top of a steel block at -20°C. The EHS substrate was mixed thoroughly by pipetting, taking care to don't introduce bubbles into the liquid. Before use, the cell culture dishes were treated in a plasma oven for sterilization and hydrophilization. The dishes were placed for 25 minutes into a cell culture incubator for gelation. Cells were detached from cell culture flasks and suspended in GM as described in chapter 2.9.2. The concentration of cells in the solution was determined with a Moxi counter. 15.000 cells were then pipetted into 3 mL Am+ and pelleted in a centrifuge at 120 rcf (rotational centrifugal force) for 5 minutes. The supernatant was discarded and the pellet was resuspended in 3 mL AM+. 100 µL of the resulting cell solution was carefully added to the EHS gels by pipetting single drops on the gel surface. Placed into a cell culture incubator, the cells were left to adhere for 25 minutes. After confirming cell adherence with a microscope by gentle shaking, the remaining media was carefully discarded by pipette without breaking the gel. Under a sterile bench, residual media was left to dry for 10 minutes to avoid dilution of the second gel layer consistent of 50 µL ice-cold EHS-substrate, which was subsequently pipetted on top of the first gel layer and distributed over the inner well of the dish by rotational tilted movement. The second gel layer was also left to solidify in a cell culture incubator for 25 minutes before finalizing sample preparation by adding 1.5 mL AM+. 3D cell culture samples were kept in a cell culture incubator, discarding old and adding fresh media every 3 to 4 days. At day 9 of cultivation, cells were starved for EGF by discarding AM+ and adding AM- to maintain a well-described developmental process of breast epithelium spheroids.

2.9.5 MCF10A spheroid transfer and fixation

For fluorescent imaging of immunostained targets, spheroids were transferred onto high-precision cover glasses to achieve the highest possible image quality. For this, spheroid samples were cultivated as described in chapter 2.9.4 and were treated with 2 mL CRS for 30 minutes at 4 °C. Subsequently, the solution was discarded and the EHS-gel was disrupted by pipetting with a 1000 µL pipette tip after adding 1mL of ice-cold AM- to the sample. The resulting spheroid suspension containing EHS-gel residues was transferred to a low binding 1,5 mL reaction tube. In 300 µL steps, the suspension was pipetted onto clean 35Ø mm cell culture dishes to pick up individual spheroids with a 200 µL pipette tip utilizing a Binocular Stemi 2000-CS. The spheroids were transferred into 300 µL of fresh cold AM- in a low-binding reaction tube to minimize EHS-gel residues. This spheroid suspension was similarly placed into a cell culture dish to take up ~20-50 spheroids in 20 µL volume and transferred onto an EHS-substrate coated cell culture dish with a high precision cover glass bottom plate. Dishes were coated overnight at 4°C with 20 µg/mL EHS-substrate in PBS. Spheroids were left to adhere to coated surfaces for 20 to 30 minutes. After adherence was confirmed via microscopy, the spheroids were fixated with a 3.7% PFA in CB solution for 20 minutes before washing 5 minutes with a 30 mM glycin solution and storing samples at 4°C in 1 mL CB buffer until immunocytochemical treatment.

2.10 Shear stress device experiments

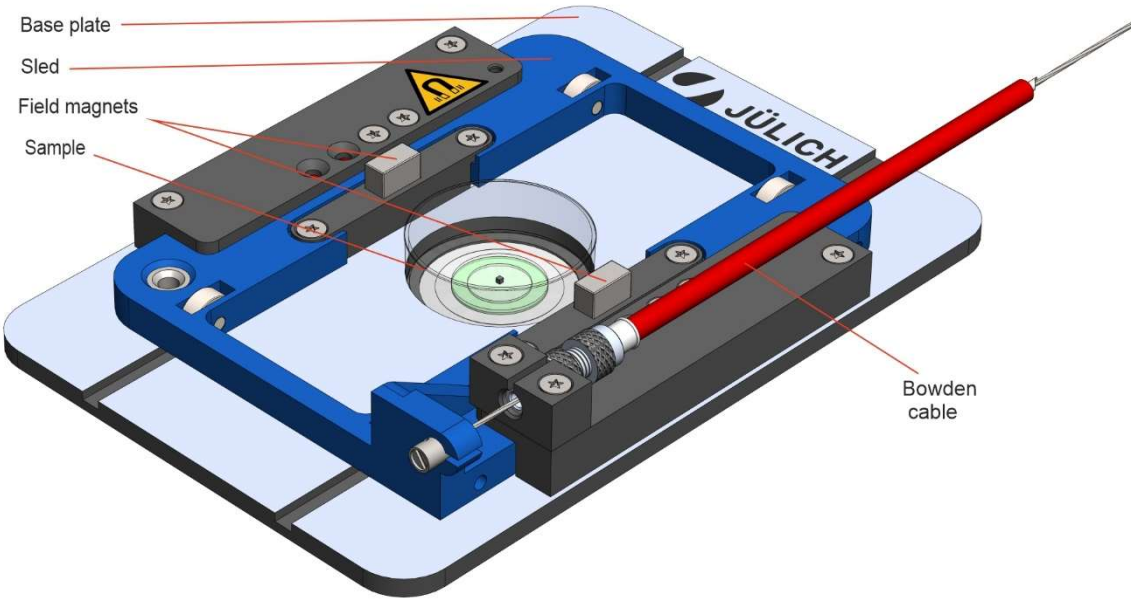

Figure 17: The magnetic shear stress device developed in the course of this work. Engineering schematic of the shear stress device. Image by Jens Konrad.

All stress application and strain measurements in hydrogels and MCF10A spheroids were performed with a shear stress device (figure 17). All experiments were performed with a Zeiss LSM (laser scanning microscope) 880 with an airy scan detector equipped with an Incubator XL. At least 3 hours prior to experiments, the device was placed into the microscopes table and incubation was set to 37 °C. For treatment with $GdCl_3$, 6 µL of a 10 mM $GdCl_3$ stock solution was mixed with 3mL AM-, which was added to the samples before stress application.

2.10.1 Shear stress device principle and design

In principle, the shear stress device utilized magnetic coupling to apply a pulling force parallel to the surface of EHS-substrate-derived hydrogels. The device has a moveable sled with two built-in field magnets (figure 17). For shear stress application, a magnetic sample lid was attached to the top of a hydrogel.

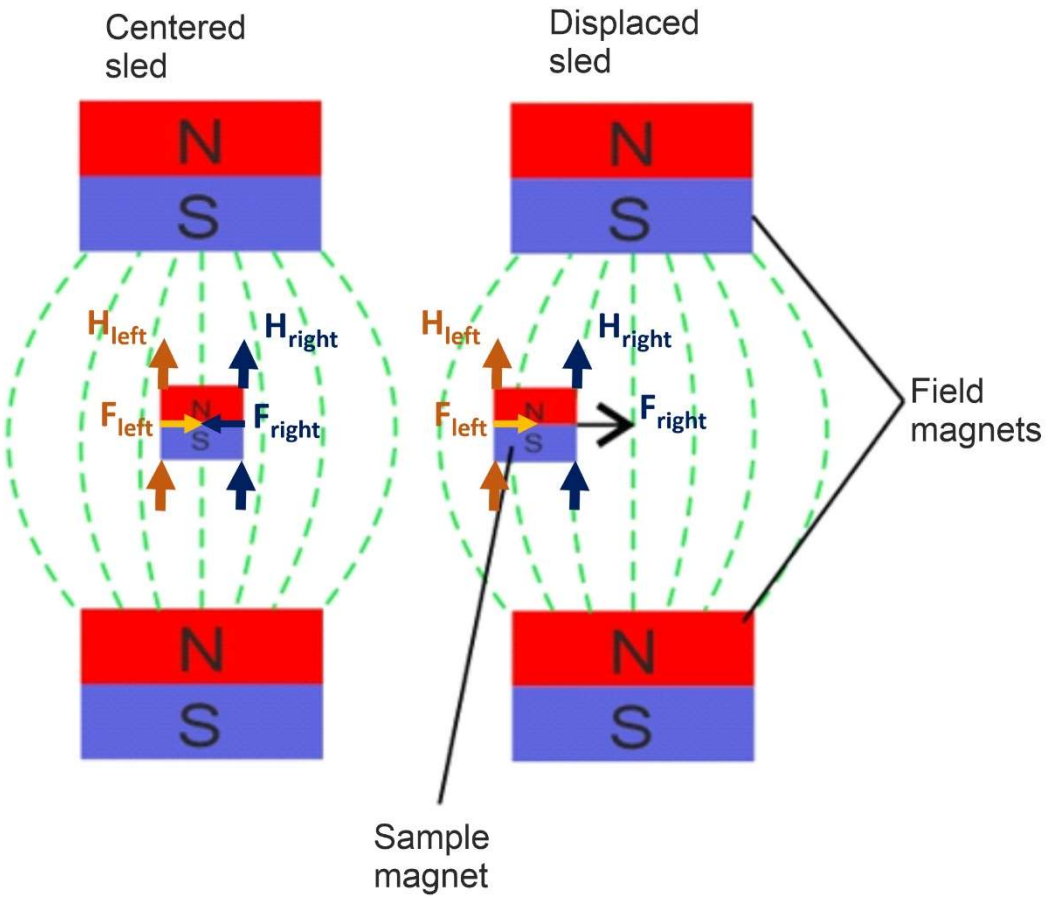

Figure 18: Principle of the shear stress device. Schematic of magnet orientation for stress application. Displacement of the sled relative to the sample creates and increasingly inhomogeneous magnetic field around the sample magnet. Green dotted lines indicate magnetic field lines. For a centered sled: Magnetic field strength $H_{left} = H_{right}$ force equilibrium ($|F_{left}|=|-F_{right}|$, opposite directed forces, SF=0), no movement. For a displaced sled: Magnetic field strength $H_{left} < H_{right}$ no force equilibrium ($F_{left}<F_{right}$, same direction of forces, SF>0), movement into center. $F=\mu_0 .PH$. μ_0 =- magnetic constant. P = pole strength. Courtesy of Dr. Ronald Springer

Placed into the device is the magnetic sample lid exposed to constant forces. If the sled is centered, the forces are equal in all directions. If the sled is displaced, a pulling force acts in the displacement direction (figure 18).

The shear stress device consisted of an aluminum baseplate and a movable sled containing two field magnets (Figure 17). The base plate of the device was milled from a 4 mm aluminum plate and held 35Ø mm cell culture dishes. A 3D-printed sled holding the two neodymium magnets (30x5x10 mm) ran along notches in the baseplate via four ball bearings. The magnets were lowered through the bottom of the base plate, ensuring that the center of their magnetic field was positioned exactly 1 mm above the sample's magnet. Movement of the sled is enabled by a tensed Bowden cable and antagonistic springs (figure 19). The Bowden cable is

connected to a high-precision step motor that is controlled via a programmable motor control unit. This setup allows for the placement of the device into a microscope table or cell incubator while the sled-driving elements are placed separately. The device, therefore, allows for the use of microscope incubation chambers during experiments, ensuring that samples can be stably tempered at 37 °C during experiments while avoiding vibrations caused by motor movement to disturb image acquisition.

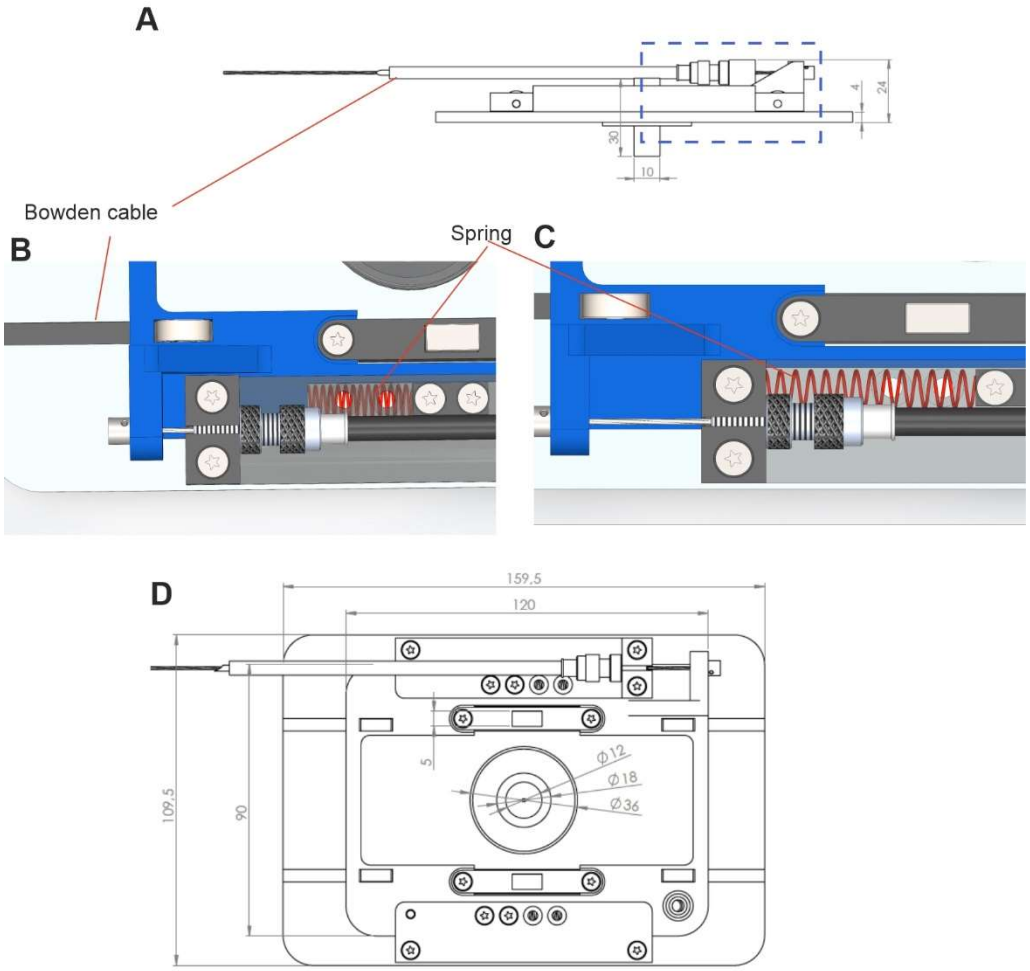

Figure 19: Technical principle of sled movement. (A) Schematic of the shear stress device from the side (mm). The Blue dotted line denotes the position of the spring in the device that is compressed (B) by pulling on the Bowden cable. The release of tension at the Bowden cable allows the Spring to expand (C) and push the sled back to its original position. (D) Schematic of the shear stress device from the top (mm). Images adapted from technical schematics by Jens Konrad.

To utilize force application via magnetic coupling, EHS-derived hydrogels are equipped with a magnetic sample lid (Figure 20 A). Magnetic sample lids were created by attaching a 1 mm^3 neodymium magnet to a 13Ø mm cover glass. Theoretically should movement of the device's sled results in a pulling force acting on the magnetic lid in the same direction.

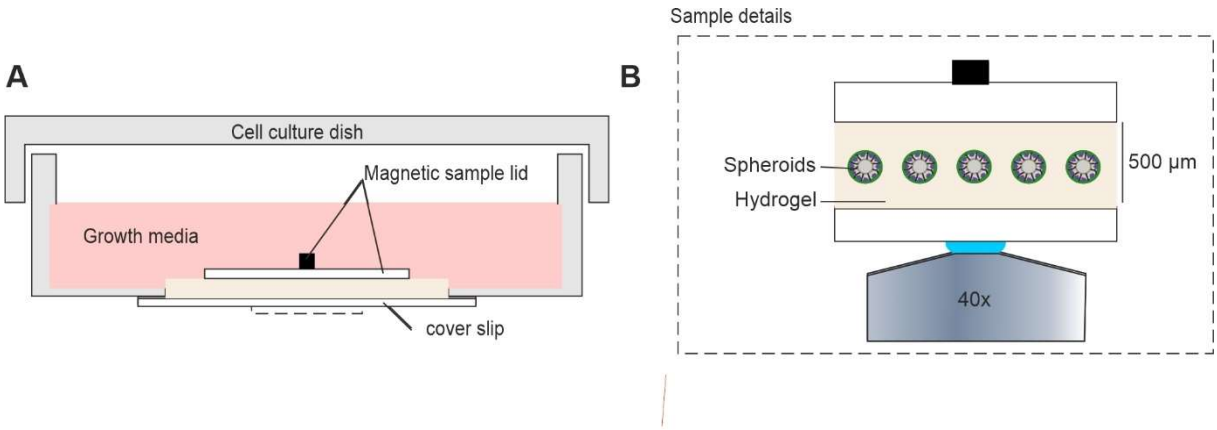

Figure 20: Hydrogel sample setup for shear stress application. (A) Detailed view oa a shear stress sample. (B) Magnification of the highlighted area (dashed line) in (A). Adapted from [204]

As this force is translated to the gel via the magnetic lid's cover glass, it results in the shear straining of the gel and embedded spheroids. Accordingly, there should be no magnetic pull on the sample lid as long as it is precisely positioned in the center of the sled's magnetic field.

This design allowed for the contactless application of mechanical stress minimizing torque on the sample. Samples can therefore be prepared and sealed in a sterile environment, greatly decreasing the danger of bacterial or fungal contamination, a common problem when working with cell culture models[205].

Further, the design allowed access to the sample with an objective mounted in an inverse microscope, enabling live cell imaging (LCI) to study cellular behavior during stress application (figure 20 B). This feature is crucial for investigating dynamic cellular mechanoresponses such as changes in motility or morphology.

The setup also allowed the sample to be immunocytochemically treated after stress application. Imaging of immunocytochemically labeled target cellular structures via fluorescence microscopy is a versatile technique indispensable to cell biological research. In a mechanobiological context, it allows for visualization of protein localization and expression levels that indicate cellular differentiation or facilitate sensation and transduction of mechanical cues.

Moreover, a confocal microscope allows imaging of a focal plane of interest with a high axial resolution. Thereby acquired fluorescence imaging data of multiple focal planes allows for the reconstruction of 3D objects.

2.10.2 Sample preparation for shear stress experiments

All samples for shear stress application were prepared with an EHS-subtrate-microsphere mixture for analysis of gel deformation by incorporation of FluoSpheres® carboxylate microspheres (0,2 µm, 660/680) into EHS gels. FluoSpheres® were stored in methanol at 4°. To discard the methanol, the microspheres were washed washed by mixing 20 µL of microspheres with 980 µL of ice-cold PBS before centrifugation at 13.000 g for 10 minutes. After discarding the supernatant, the microsphere pellet was suspended in 1 mL of ice-cold PBS and pelleted at 13.000 rcf for 10 minutes. The pellet was finally suspended in 20 µL PBS before being carefully suspended in 1mL of ice-cold Geltrex, avoiding bubble formation in the mixture.

Samples for shear stress application to MCF10A spheroids were prepared as described in chapter2.9.4, utilizing a microsphere-EHS substrate suspension, and cultivated normally until desired developmental status of spheroids was reached. 30 to 60 minutes before stress application experiments, the media was discarded and samples were placed in a magnetic positioner. After letting residue media evaporate for 10 minutes under a sterile bench, 50 µL of ice-cold microsphere-EHS substrate suspension was pipetted on top of the samples gel before carefully placing a magnetic sample lid onto the suspension with non-magnetic stainless-steel tweezers. An instantaneous rotational reorientation of the sample lid direction was observed to confirm the correct alignment of the sample lid in the magnetic positioner's magnetic field. The magnetic north-south axis was marked at the cell culture dishes edge before placing the magnetic positioner, still holding the sample, in a cell culture incubator for 25 minutes. To avoid interference of magnetic fields, magnetic positioners were placed as far away from each other as possible inside the incubator if multiple samples were prepared at once. After the EHS-substrate solidified, 3 mL of AM- containing 25 mM HEPES were added by pipetting directly to the middle of the magnetic lid. To impede media evaporation during experiments and seal samples in a sterile environment, sample dishes and lids were wrapped with Parafilm at least 3 times.

2.10.3 Stress application and stress sample fixation

For shear stress application, samples created as described in chapter 2.10.1 were placed into a shear stress device. For this, the sled of the device was first driven to a central position, as indicated by overlapping holes in the device's sled and base plate. The sample was subsequently carefully lowered into the device's sample holder while ensuring the magnetic orientation of the magnetic lid matches the sleds magnets. For stress application, the sled was moved to the desired amplitude with a speed of 4 mm/s via a computer-controlled step

motor. For the determination of the resulting strain, image stacks of microsphere or actin signal were acquired once in the “neutral” position of the sled as reference and once at a given amplitude to determine the resulting displacement as described in chapter 2.2.8. After cyclic stress application for 22 hours, samples were fixed by treatment with 1mL of a fixation solution for spheroids in EHS-gels for 20 minutes before quenching for 5 minutes 1mL quenching solution. After washing with 1 mL glycin solution, the samples were sealed with Parafilm and stored in CB buffer at 4°C until immunocytochemical treatment.

2.10.4 Step motor control

The step motor driving the sled was connected to a custom motor control unit designed and produced by Mr. Werner Hürttlen. The control unit was connected to a netbook running custom motor control software programmed by Mr. Werner Hürttlen. The software allows for programming the control unit with a defined drive protocol controlling step motor movement speed, amplitude and dwell time. For stress application, the software was calibrated to a centered sled position. For cyclic stress application, the sled position was calibrated to a position -5 mm apart center. Driving to amplitudes of 10 mm consequently allowed for sled movement from -to 0 mm to 5 mm (Figure 38).

2.10.5 2D pattern matching and tracking for displacement analysis

In-house developed software created by Dr. Ronald Springer was used to determine the displacement of microspheres and actin signal of MCF10A spheroids embedded in EHS-gels based on fluorescent images via pixel (px) pattern matching.

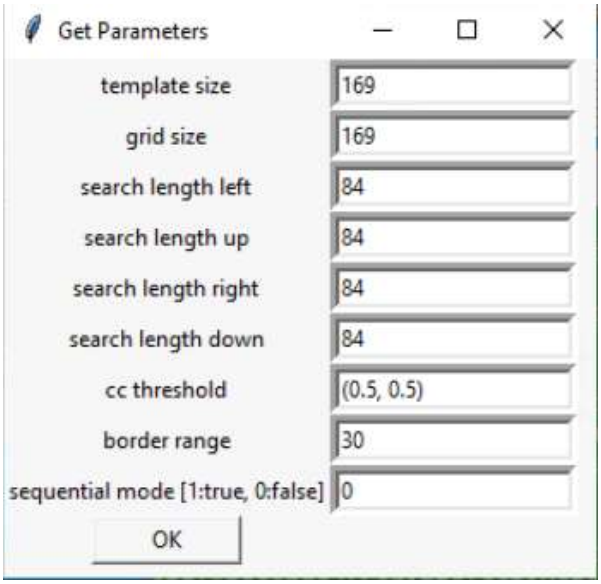

Figure 21: 2D template matching software for displacement analysis. Image of the parameter window for 2D template matching.

The software uses normalized cross-correlation for pattern matching [176,206]. The software "DetermineDVFInEachSliceV9" was a python 3 script requiring two .czi files of equal dimensions (figure 21).

Given two image files, the software analyzed the displacement of signal between each corresponding image for position, channel and Z-Slize. First, images were smoothed by a Gaussian filter with a sigma value of 0,5. A reference image (unstrained) was then divided into square templates of defined size (template size, in px) arranged in a grid of defined size (grid size, in px). Template overlap could be determined by defining different values for grid size and template size. Normalized cross-correlation was then used to perform intensity-based image registration for each template in a second image (strained). To reduce calculation load and avoid cross-correlation artifacts, a search distance could be defined for all directions. The default value for the normalized cross-correlation threshold was set to 0,5. A border area could be defined, which would be excluded from analysis (border range, in px). A sequential mode could be activated to increase the search distance for each analyzed Z-Slice (not used in this work). The cell channel could be defined if two signal channels were acquired (spheroids actin & microsphere signal). This channel was then subjected to additional global contrast analysis to avoid magnification of weak bleed-through of microsphere signal due to local contrasting and define templates containing actin signal. Only these templates were consequently used for displacement analysis of the defined "cell" channel. As microspheres were found to be incorporated into spheroids through cultivation, these templates were not analyzed for microsphere displacement.

If not stated otherwise, image stacks for shear strain analysis were acquired in fast airy mode at 0.7 x optimal resolution (as calculated by the Zen Black software) at 11 planes with 5 µm height difference between planes. After analyzing the two image files, a .xlsx file is written, saving the used parameters and the displacement calculated for each template. If not stated otherwise, the following parameters were used for 2D pattern matching: template size = 79 px (< 4-day spheroid cultivation) to 119 px (> 4-day spheroid cultivation), grid size = equal template size, search length left = 84 px, search length up = 84 px, search length down = 84 px, search length right = 300 px, cc threshold = 0.5 for both channels, border range = 30 px, sequential mode = 0).

2.10.6 Linear regression and statistical analysis

For the determination of strains in hydrogels and spheroids, the median template displacement (x) for each imaging plane (y) calculated as described in 2.2.3 was used to perform a linear regression (ordinary least squares method) with the python 3 module statsmodels. The median displacement for each imaging plane was determined after calculation of vector lengths (*1*). Strain (%) was calculated by dividing the increase in lateral displacement by the relative height difference. Therefore, an increase in lateral displacement of 10 µm for a difference in height of 100 µm results in 10% shear strain.

$$(1) Vector\ length = \sqrt{(x^2 + y^2)}$$

The python 3 module scipy.stats was employed to perform two-tailed nonparametric Mann-Whitney *U*-tests and two-sample Kolmogorov-Smirnov tests. The *p-values* of the Mann-Whitney *U*-test indicated in this work were defined as ****: $p < 0.0001$; ***: $0.0001 \leq p < 0.001$; **: $0.001 \leq p < 0.01$; *: $0.01 \leq p < 0.05$; n. s. $p \geq 0.05$; Only if the p-value of the corresponding Kolmogorov-Smirnov test was below 0.05 was significance indicated. If no significance (n.s.) was indicated, both tests resulted in $p>0.05$. The scipy.stats module was also used to calculate 95% confidence intervals.

2.10.7 Magnetic lid fabrication

Magnetic lids were produced by attaching 1 mm cubic neodymium magnets with PDMS (1:10; oil: crosslinker) to 13Ø mm #1.5 cover glasses. For cyclic stress application, magnets were encased by filling the middle third part of a 200 µL pipette tip placed on top of the magnet with PDMS. After silicone crosslinking, the glass bottom below the magnet was cut out (~3Ø mm) with scissors before being attached with PDMS to a 12Ø mm punched-out and flattened titanium mesh. For this, the encased magnet was dipped in PDMS and placed in the center of the titanium mesh, filling and sealing cracks in the cut-out cover glass and avoiding spreading of PDMS into the mesh holes by direct application of liquid PDMS to the mesh. Cover glass magnetic lids were disposed of after usage. For reuse of titanium mesh magnetic lids, they were placed in 2M NaOH over night to dissolve EHS-substrate residues. To dilute any remaining NaOH that diffused into the PDMS casing of the magnet, the meshes were placed into 0,5 L of Milli-Q water overnight before being dried for 30 minutes in a 60 °C heating cabinet.

2.10.8 Rheological analysis

All rheological analysis were performed by Susan Babu (DWI, RWTH). Shear moduli measurements of pure and diluted (70% Geltrex, 30% DMEM/F12) hydrogels were performed on a DHR three Rheometer from TA instruments at 37°C using a cone and plate geometry of 20 mm diameter, with a 2° cone angle and at 51 µm truncation gap. To prevent water evaporation, a solvent trap was used during measurements. Recording of time sweep measurements was done at 0.5 Hz frequency and 0.5% strain for 30 min. Dropping of the loss tangent (tan (δ)) value below 0.1 was interpreted as the point of gelation. All subsequently measured after gelation were averaged to determine the storage modulus.

2.10.9 Dextran tracer assay

For analysis of dextran diffusion into EHS-stubstrate, confocal time-series imaging was employed. Samples were produced by casting an EHS-gel from 150 µL EHS-substrate with embedded microspheres (for details, see chapter 2.10.2). Magnetic sample lids were attached to the liquid gel before incubating samples in a humidified cell culture incubator for 25 minutes. Samples were overlayed with 3 mL AM- immediately after gelation of the EHS-substrate. For imaging, the incubator XL unit was tempered to 37°C. For the experiment, sample media was completely exchanged for 1 mL AM- containing 200 µg/mL 10 kDa Texas red conjugated Dextrans (Stock solution: 10 mg/mL, Prepared by Dr. Aljona Gaiko-Shcherback [207]). Time series imaging of Texas red signal every minute was started immediately (<1 min) after adding the medium. All images were acquired with the same detector gain and laser intensity. For the determination of relative intensity, the mean absolute intensity of an imaging position was determined within a region of interest (100 x 100 µm) for each timepoint with the Zen Black software and for the reference image. Each intensity value of the time-series was then normalized with the absolute signal intensity of the reference.

2.11 3D microsphere tracking in PEG-hydrogels

All Z-stack imaging for microsphere displacement analysis was performed with a Zeiss LSM 880 with an airy scan detector equipped with an Incubator XL and a Zeiss LD C-Apochromat 40x/1.1 W Corr M27 objective. For details on the creation of pNIPAM-bearing PEG-hydrogel samples, see appendix.

2.11.1 Embedding MCF10A spheroids into PEG-hydrogels

MCF10A spheroids were transferred into poly ethylene glycol (PEG) hydrogels produced by Susan Babu (DWI, RWTH Aachen) to determine displacement vector fields in hydrogels of defined stiffness. The protocol for PEG-gel production was followed as published [208]. Multi-arm PEG precursors were conjugated with a non-degradable peptide. EHS-substrate was added to all precursor mixtures for a final protein concentration of 6 mg/mL. The final polymer content (wt%) was adapted for gels of different stiffness (45 Pa: 1.25%; 200 Pa: 1.75%; 400 Pa: 2.25%).

Fluorescent microspheres were embedded into the gel by washing the microspheres as described in 2.10.1 before combining the microsphere-PBS (1 µL) solution with the PEG-precursor solution and placing the mixture into an ice-filled ultrasonic bath for 30 minutes. Spheroids were cultivated for 11 days as described in 2.9.4 and extracted from hydrogel as described in 2.9.5. Spheroids were not placed onto cover glasses but transferred into a PEG-precursor/microsphere solution in 10 µL ice-cold medium. Factor XIII was added to the PEG-precursor/microsphere/spheroid mixture before creating 25 µL gel droplets placed on #0 cover glass bottom cell culture dishes to trigger crosslinking of the PEG-precursors. After 25 minutes of gelation in a cell culture incubator, 1.5 mL AM- was added to the cell culture dish. For immunocytochemistry, samples were fixed as described in chapter 2.9.5.

2.11.2 3D pattern matching and tracking for displacement analysis

Three-dimensional (3) pattern matching for determination of microsphere displacement was performed with a python3 script created by Dr. Ronald Springer named "DetermineDVF3DMultiprocessing.py" (Figure 22). The software utilized the same normalized cross-correlation-based approach to pattern matching as described in 2.10.5 [176,206]. For this analysis, the software uses image stacks saved as multidimensional .tiff-File. The first time point is used to create 3D cuboid templates for subsequent pattern matching at every additional time point. Templates were created by dividing 3D imaging data into cuboid patterns of desired dimensions (template size XY/Z). The software-determined displacement of microspheres between multiple time points by cross-correlating patterns in a given volume (search length x/-x/y/-y/z/-z) for every time point. 3D drift correction was performed similarly by the determination of template displacement in the 8 corners of the image stack and either using the median or mean displacement to shift image stacks, creating a new .tif file.

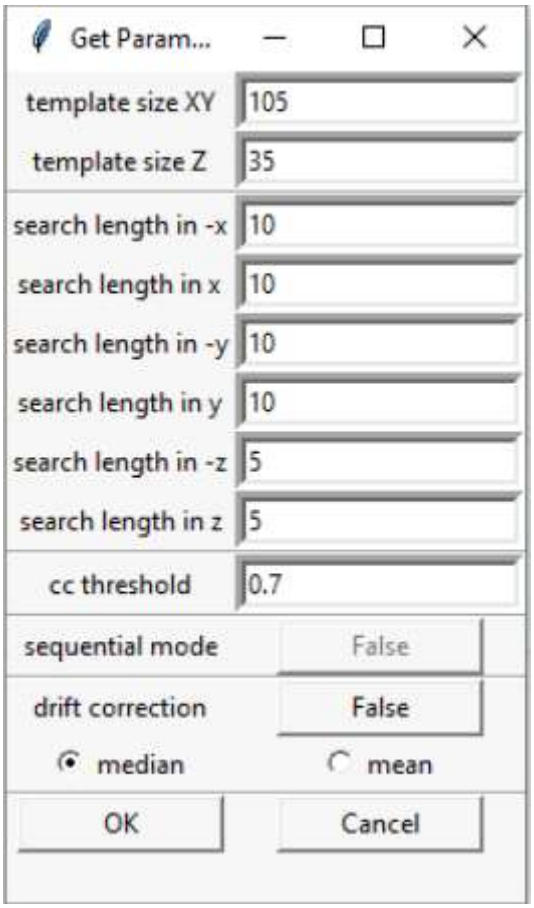

Figure 22: 3D template matching software for displacement analysis. Image of the graphical user interface of DetermineDVF3DMultiprocessing.py.

Non-spheroid-derived deformations were corrected for by affine transformation with the python3 script “DoAffineCorrectionto3DData.py” created by Dr. Ronald Springer (for details, see appendix).

2.11.3 3D vector graph creation and bar charts

All 3D vector graphs were created with the python3 script “Quiver3DResultsV2.py” developed together with Dr. Ronald Springer. The script reads the positional information of templates and the corresponding determined displacement of an excel file created with “DetermineDVFin3D.py”. Displacements are depicted as vectors originating in the center of their template. The vectors are color coded for their length in pixels relative to the vector with the highest pixel length.

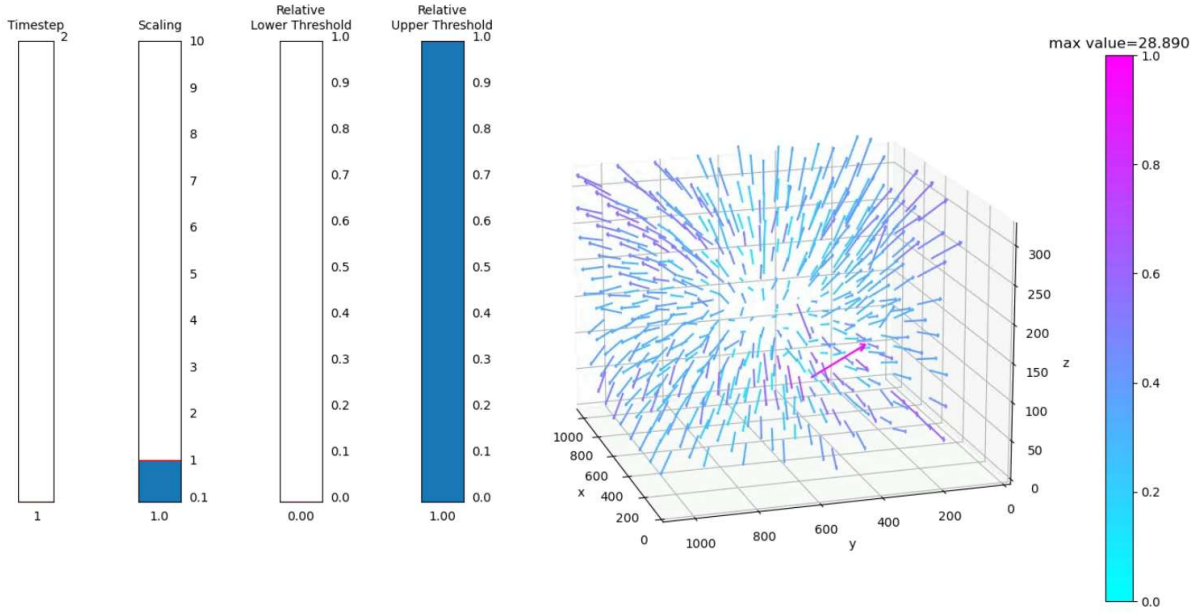

Figure 23: 3D vector graph creation. The graphical user interface of the Quiver3DResults software.

The graphic user interface of the software (figure 23) allows for interactive changing of timestep to be shown from the dataset, scaling of vectors and thresholding vectors by relative length. All graphs presented in this work were created with a scaling of 1 (true scaling of vector) a relative lower threshold of 0 and a relative upper threshold of 1 (all displacement vectors are shown) if not stated otherwise.

For bar charts, vector length was calculated (formula 2) for each displacement vector determined for a given analysis with “DetermineDVFin3D.py”. The height of bars in bar chart

represents the total sum of all vector lengths for the whole analyzed volume for a given analysis.

$$(2)\ Vector\ length = \sqrt{(x^2 + y^2 + z^2)}$$

For outlier detection, vector lengths for each displacement vector were calculated (*2*) and sorted from lowest to the highest value. The first quartile (Q_1) was the highest value in the lowest 25% of values and the third quartile (Q_3) was the lowest value in the lowest 75% of values. The interquartile range (IQR) was determined by subtracting Q_1 from Q_3. Values smaller than Q_1-5 x IQR or bigger than Q_3+5 x IQR were deleted.

2.12 Immunocytochemistry

Spheroids fixated in EHS-substrate or transferred onto cover glasses were immunocytochemically treated to fluorescently label cellular components. If not stated otherwise, washing steps were performed with 1 mL CB buffer at room temperature for 5 minutes on a rocker at 10 rpm. To facilitate antibody diffusion into the cells, plasma membranes were permeabilized by treatment with 1% triton-X-100 in CB for 20 minutes. After washing thrice, unspecific binding sites were blocked with 200 µL 5% milk powder and 1% goat $F(ab')^2$ in CB buffer at room temperature for 2 hours. Primary antibodies were diluted 1:200 in dilution buffer to treat samples overnight at 4°C on a rocker at 10 rpm. After washing thrice, the secondary antibodies were similarly diluted to treat samples for 45 minutes at room temperature. To avoid bleaching of fluorescent secondary antibodies, light exposure was avoided from this step forward. DAPI or DRAQ5 staining was applied additionally to stain DNA. After washing thrice, samples were stored at 4°C in 1 mL CB buffer.

2.13 Confocal laser scanning microscopy

All microscope images were acquired using a Carl Zeiss LSM 880 with an airy scan detector and a Zeiss LD C-Apochromat 40x/1.1 W Corr M27 objective. Fluorophores were excited with lasers of varying wavelengths (405 nm, 488 nm, 561 nm and 633 nm). Emitted light was filtered with specific combinations of Band- Long- and Short-pass filters to select the range of wavelengths that pass through to the detector unit. The detector unit was an airy scan detector, a collection of 32 concentrically arranged GaAsP-detector elements, each acting as its own pinhole with a diameter of 0,2 airy unit. Similar to structured illumination microscopy techniques are the excitation and detection-point spread function (PSF) for individual detector units shifted during imaging. The Zen Black software allows for the composition of an image

using acquisition data of all 32 detector units by pixel reassignment. This technique increases lateral resolution compared to standard confocal microscopy techniques while simultaneously increasing axial resolution due to the small size of the pinholes.

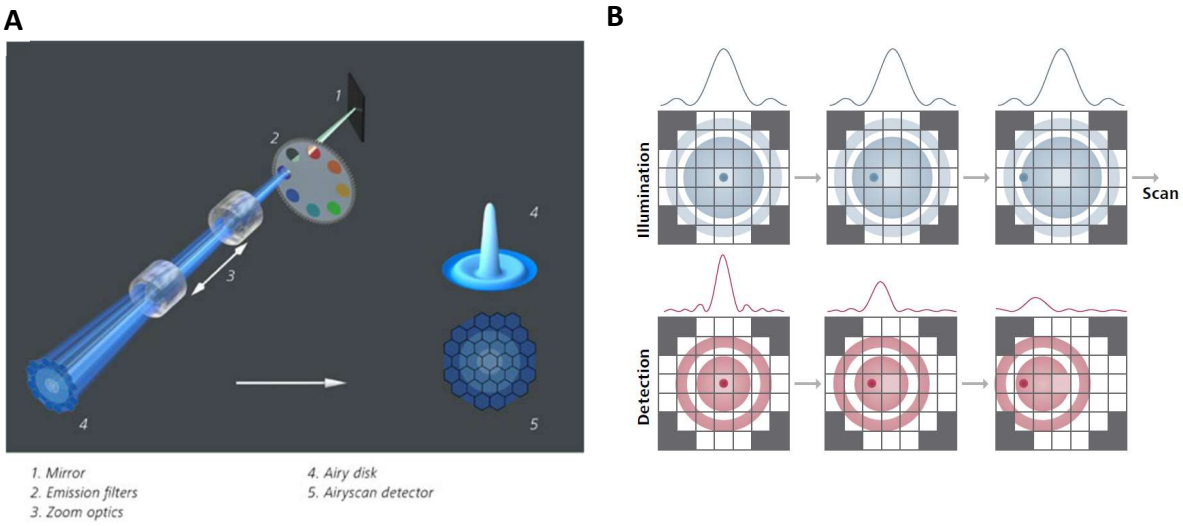

Figure 24: The airy scan detector principle. (A) Schematic of the light path inside the airy scan detector. (B) Principle of shifted illumination and detection utilized by the 32 GaAsP-detector array. Adapted from [279,280]

All micrographs of immunocytochemically treated spheroids presented in this work were acquired with the Airy scan detector in signal-to-noise ratio (SNR) -mode, optimal resolution in x,y and z as automatically calculated by the ZEN Black software. The pinhole was set to 0.2 Airy units and optimal illumination of the detector unit was maintained during imaging. Image data from microspheres in hydrogels or LCI of MCF10A LiveAct-RFP spheroids was acquired in the Fast-Airy mode (resolution was 1024 x 1024 px). The Fast Airy mode allows for the acquisition of 4 lines at once by projecting an elliptical illumination pattern (elongated in y) onto 16 of the GaAsP-detector units. While this minimized resolution gain by use of an Airy scan detector, it vastly increased the imaging speed necessary to avoid gel creep during shear stress experiments. All raw Airy scan data was processed in 2D mode with automatically detected strength.

2.14 Cell culture dish preparation

For the cultivation and transfer of MCF10A spheroids, cell culture dishes were produced from blank plastic dishes and cover glasses. The 35Ø mm blank dishes contained a 18Ø mm hole comprising an inner well. To the bottom of such blanks was PDMS (1:10; oil: crosslinker) spread around the hole with a syringe. Dependent on the intended use for the cell culture dishes, cover glasses (22 mm x 22 mm) of various thicknesses were attached to the bottom of the dishes by pressing them into the PDMS. After ensuring the dishes hole is continuously sealed by PDMS, samples were placed into a heating cabinet at 60°C for at least 16 hours to cure the silicone.

3 Results

This work was concerned with investigating mammary epithelial mechanoresponses in a physiological context. Of interest was how normal breast epithelium reacts to externally applied solid shear stresses and how force generation is modulated by substrate stiffening. In detail, how does the differentiation state of breast epithelial cells modulates their mechanoresponse to externally applied mechanical shear stresses? Further, how exactly are cell-derived forces of well-differentiated epithelial cells modulated by increasing stiffness in 3D matrices?

To answer these questions, state-of-the-art 3D cell culture models had to be employed to allow for tissue scale reconstruction of the breast gland *in vitro*. Therefore, the MCF10A 3D cell culture model was employed to analyze mechanoresponsive processes in nature-like spheroids recapitulating normal mammary epithelial architecture and differentiation.

However, no tools allowing for the application of solid shear stress to such 3D cell culture constructs. First, this work addresses this lack of tools by developing a technique to apply defined physiological stresses to natural hydrogels and embedded mammary epithelial spheroids. Secondly, this device was used to analyze the shear strain response of MCF10A spheroids based on developmental status. Lastly, a 3D TFM approach based on confocal microscopy was developed that allows tracking of cell-force derived deformations in 3D matrices.

3.1 A novel magnetic shear stress device for the application of physiological stress to breast epithelial spheroids

Grasping the influence of mechanical stress on cellular differentiation and tissue development in the breast gland requires investigation of cellular behavior in response to defined mechanical loads. To make sound assumptions about the natural behavior of mammary epithelial cells to such stresses further requires these investigations to be made under the most feasible physiological conditions possible. Therefore, several requirements for developing a novel approach to apply defined stresses to breast epithelial cells in a nature-like context. First, the cell culture model had to resemble natural breast gland architecture and cellular differentiation. Secondly, these cells must be embedded into a 3D matrix resembling the ECM of mammary tissue in protein composition and mechanical stiffness. Third, the strain acting on the cells had to resemble naturally occurring solid shear strain in amplitude and

frequency. Finally, the approach had to facilitate observations on potential short and long-term mechanoresponses of stressed cells.

All these conditions were met by a simple yet effective concept apparatus named the shear stress device (for details, see chapter 2.10). This innovative tool utilizes magnetic coupling to create a force parallel to the surface of a hydrogel, theoretically resulting in shear strain.

The concept of the technique was thought of by Prof. Rudolf Merkel and Dr. Erik Noetzel-Reiss at the Institut für Biologische Informationsprozesse 2: Mechanobiologie (IBI-2) at the Forschungszentrum Jülich (FZJ). The prototype device and all following iterations were designed and constructed by Jens Konrad (IBI-2, FZJ). Pilot experiments were conducted by Dr. Jenny Gehlen and B. Sc. Sven Gerlach (IBI-2, FZJ).

As part of this work, was this concept device tested and thoroughly optimized trough systematic analysis and adaption. The optimized device was then utilized to investigate the mechanical properties of MCF10A spheroids and their cellular reaction to prolonged cyclic shear straining.

My publication, “ECM-transmitted shear stress induces apoptotic cell extrusion in early breast gland development” was created as part of my Ph.D. project and summarized the main findings regarding the shear stress device.

3.1.1 Shear strain in hydrogels, technical optimization and tests for sample stability

Before applying stress to breast epithelial spheroids, it was necessary to characterize gel deformations created with the shear stress device. Therefore, it had to be tested whether stress application with the device resulted in shear strain in EHS-gels (figure 25). For this, the displacement of fluorescent microspheres was tracked in 3D to determine EHS-gel deformation.

To test this, far-red fluorescent microspheres were incorporated into a liquid EHS substrate (for details, see chapter 2.10.2). The EHS substrate microsphere mixture (100 µL) was then used to cast an EHS-gel and attach a magnetic lid. This sample was placed into the device with a centered sled position.

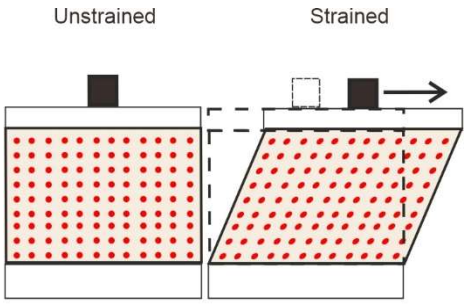

Figure 25: Principle of hydrogel deformation during shear stress application. The schematic highlights the principle of shear deformation. Sled movement creates shear stress, resulting in shear strain in the hydrogel. Tracking of individual microspheres (red dots) incorporated into the gel allow for tracking of gel deformation.

The microspheres were then imaged with a confocal fluorescence microscope during sled displacement. It was observed that the microspheres were displaced in synchrony to sled movement within a single focal plane. The movement was observed to occur mostly along sled displacement direction. Thereby was confirmed that sled displacement results in gel strain. To confirm this strain was a shear strain, it was necessary to track microsphere displacement in 3D by acquiring 2D images at multiple focal planes (Z-Stack).

The position of the fluorescent microspheres was subsequently imaged throughout the 300 µm thick unstressed EHS-gel. After stress was applied by 5 mm sled displacement, the position of the microspheres was captured again in 3D. Superimposing the 3D positional information of the microspheres before and after sled displacement revealed that the lateral (X-Axis) displacement of microspheres in stressed gels increases with increased distance from the bottom of the gel (Figure 26). Thereby was confirmed that the devised setup of the shear stress device and magnetic lid-equipped samples works as intended and creates pure shear strain in the hydrogel.

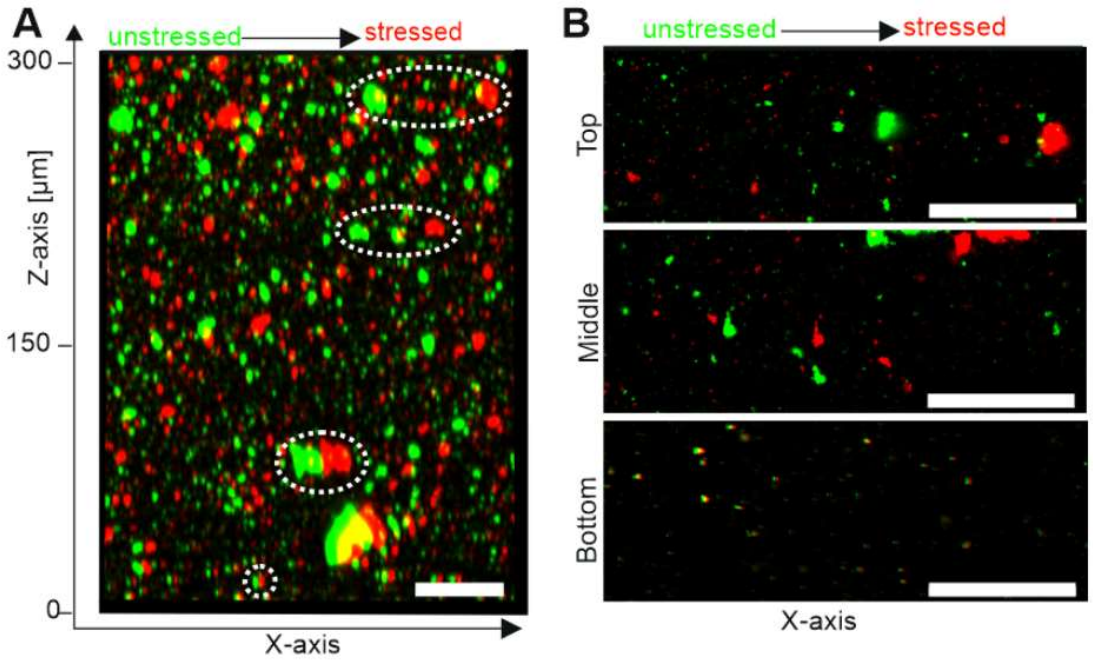

Figure 26: Sled displacement creates shear strain in hydrogels. A microsphere laden EHS-gel (100 µL) was shear strained by 5 mm sled displacement. (A) Fluorescent microsphere position was captured by Z-stack imaging in the gel before and after stress application. Imaging stacks were superimposed to demonstrate microsphere displacement upon stress application. White ellipses show well discernible bead aggregate displacements at different heights. (B) Representative micrographs of single focal planes from A show bead displacements parallel to sled movement axis (x-axis). Image stacks were acquired in signal to noise ratio mode with optimal Z-resolution over a distance of 300 µm at 0.7 x optimal pixel size (X and Y) as calculated by Zen Black software. Scale bars = 50 µm. Image stack acquisition time (~20 minutes) Adapted from [204]

Notably, microsphere displacement was also noticed when the gel was stressed constantly stressed. This observation was believed to be caused by gel creep. Supported by a previous study observing gel creep in EHS-gels, future experiments were planned accordingly to avoid this effect [209].

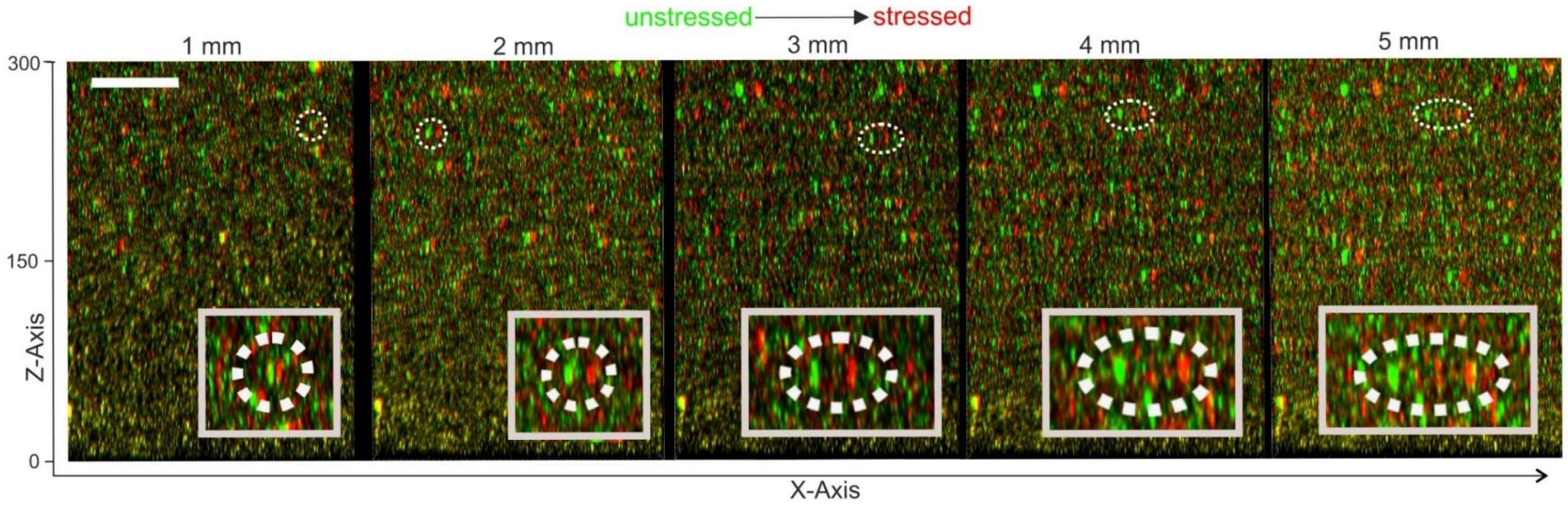

Figure 27: Strain amplitude is dependent on sled displacement amplitude. A microsphere laden EHS-gel (100 µL) was shear strained by 1 to 5 mm sled displacement. Fluorescent microsphere position was captured by Z-stack imaging in the gel before and after stress application. Imaging stacks were superimposed to demonstrate microsphere displacement upon stress application. Image stacks were acquired in fast airy mode with optimal Z-resolution over a distance of 300 µm at 0.7 x optimal pixel size as calculated by Zen Black software. White ellipses show well discernible bead aggregate discplacements at similar heights. Images were created with imaris 3D viewer tool. White boxes show the elipses in magnification Image acquisition time ~5 minutes. Scale bar = 50 µm

Correspondingly, imaging of microspheres in strained gels was performed with priority on imaging speed rather than resolution for subsequent analysis (~5-8 minutes instead of ~20 minutes per Z-Stack) in all future experiments. To further analyze whether sled displacement correlates with strain amplitude, visual microsphere tracking was performed again at sled displacements of 1 mm, 2 mm, 3 mm, 4 mm and 5 mm, resulting in an increase in strain for each increment of sled displacement (Figure 27). Notably, the displacement at 5 mm was substantially lower in this analysis, which was performed at increased imaging speed.

Detachment of sample lids was frequently observed (~50%) in samples are placement into the shear stress device. In case of detachment, the magnetic lid was always pulled towards one of the magnets of the device's sled. The most likely reason for this observation was a decentered position of the magnet. More clearly, the sample's magnetic lid was not placed correctly at the sample's center, which caused inequal magnetic attraction forces on the sample magnet toward the field magnets. It was indicated that the manual preparation of samples resulted in high heterogeneity, which was viewed as highly problematic for future strain characterization. A magnetic positioner was devised by me and created by Jens Konrad to approach this problem and ensure consistency during sample preparation. The 3D-printed magnetic positioner held two cuboid magnets (NeFeB, 30x10x5 mm) positioned 4 cm apart and above the sample (Figure 28). This setup should create a constant upwards pull on the magnetic lid toward the middle of the sample via magnetic coupling, ensuring its cantered position during EHS-substrate gelation. As this approach effectively prevented sample destruction, all samples described in the following have been created utilizing the magnetic positioner.

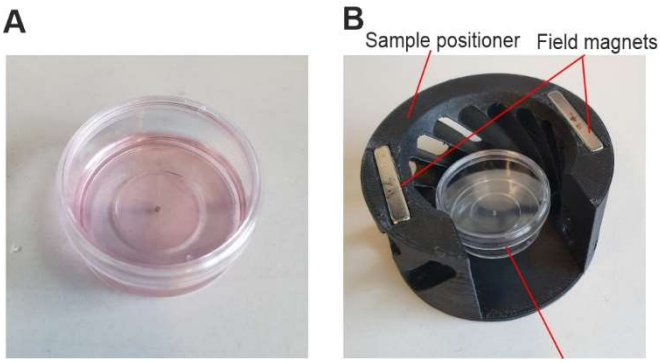

Figure 28: Sample creation (A) Photograph of a sterile ready-to-use sample. (B) Photograph of a sample placed into the magnetic positioner. Adapted from [204].

Defining the homogeneity of produced strain in HES-gels was crucial for further strain characterization as inhomogeneity could directly affect the intended analysis of strain responses in cell culture constructs. Also, strain linearity had to be analyzed.

3.1.2 Quantification of solid shear strain in EHS-gels

To characterize the homogeneity and linearity of shear strain within hydrogels, an approach to accurately determine strain computationally had to be developed.

Determining the lateral displacement of gel-embedded microspheres at multiple focal planes of the gel appeared as the most precise solution. However, manual measurement of lateral displacement is inaccurate on a micrometer scale. For this purpose, image analysis software was developed by Dr. Ronald Springer to determine lateral microsphere displacement upon gel straining accurately (for details, see chapter 2.10.5).

The software allowed for cross-correlation-based image analysis to track microsphere displacement in EHS substrates upon stress application.

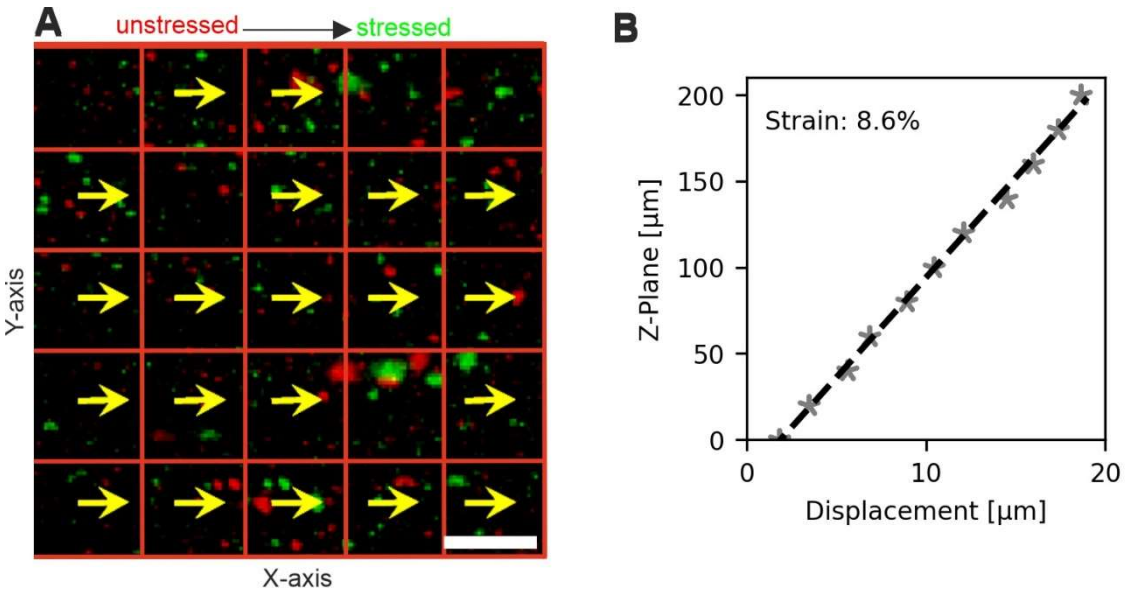

Figure 29: Computational analysis of microsphere displacement. (A) Representative image of determined microsphere displacements for templates (200 x 200 px) in an individual focus plane with s search length of 100 px in y,-y and -x and 200 in x direction. Yellow arrows show determined displacement vectors (true scaling). Cross-correlation threshold was 0.5. (B) Shear strain in a gel was determined via linear regression (dashed line) of media displacements calculated for each focal plane (A). Value "0 µm" indicates the first plane of the recorded image stack (absolute gel height >300 µm). The local strain was calculated from the slope of the regression line. Image stacks were acquired in fast airy mode win 20 µm intervals on the Z-axis at 0.7 x optimal pixel size as calculated by Zen Black software. Adapted from [204]

In practice, fluorescent microsphere-laden hydrogels were produced and shear strained as described in 3.1.1. Z-Stack imaging was again performed to capture microsphere positions in strained and unstrained gels. In all further described analyses, “stress application “ refers to moving the sled 5 mm from the device's center if not stated otherwise. To increase analysis speed and avoid gel creep, only 10 Images were taken over a gel height of 200 µm. The software was then used to automatically determine the microsphere displacement for each imaging plane (Figure 29 A). Each imaging plane's average resulting displacement vector length was then used to perform linear regression analysis.

The strain was deducted from the steepness of the regression line determined with the ordinary least square method (Figure 29 B). This analysis revealed a strain amplitude of 8.6% with a coefficient of determinations (r^2)>0.99 for linear regression for the local strain depicted in Figure 29. Thereby was shown that shear strain in the hydrogel was near perfectly linear. All local strain measurements described in the following were performed this way. Measurements that resulted in an r^2 below 0.7 were excluded from statistical analysis.

The software allowed for the determination of strain, providing a tool to increase throughput and enabling further analysis of strain homogeneity within and across samples.

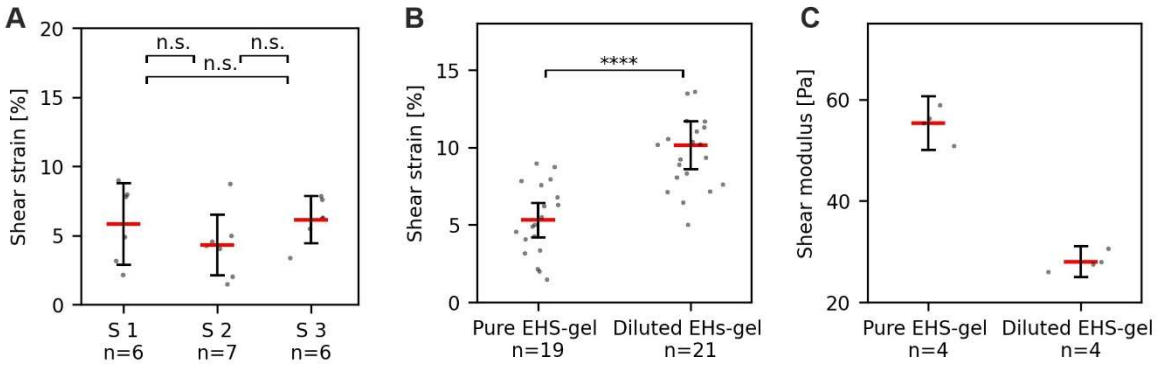

Figure 30: Shear strain in pure and diluted EHS-gels. (A)Three samples (S 1-3) of pure EHS-substrate were shear strained by 5 mm sled displacement and local strain was determined for n positions. n=number of local strain measurements for each sample. The threshold for linear regression was $r^2 > 0.7$. Local measurements (B) Scatter plots of shear strain measured at n positions across 3 individual sample in pure and diluted hydrogels at 5 mm sled movement, i.e., identical shear force. The threshold for linear regression was $r^2 > 0.7$. (C) Shear moduli of pure and diluted hydrogels as determined by rheology. . n = total number of measurements. Scatter plots: Red bars: mean, bars 95% confidence interval. For statistical tests, the Mann–Whitney U-test was used with: **** = $p < 0.0001$, * = $p < 0.05$, n.s. (not significant) = $p>0.05$. Adapted from [204]

Employing the new software, three individual samples (100 µL EHS-substrate / sample) were analyzed for their strain amplitude at 5 mm sled displacement (figure 30 A). The difference in measured strains (Means: S1=7.2; S2=9.6; S3=6.4) was found to be insignificant between samples. However, 95% confidence intervals (CI) for determined local strains within samples were large (CIs: S1=2.9 to 8.8%; S2=2.1 to 6.5%; S3=4.4 to7.8%). Therefore, strain within a sample is heterogenous, but average strains across samples is similar.

Next, strain production with the device was characterized by applying stress to EHS gels of lower stiffness. Applying the same force to a gel of lower stiffness should result in higher strain values proportional to its stiffness. To test this, strain measurements were performed on hydrogels produced with diluted EHS-substrate (70% EHS-substrate, 30% DMEM F/12, 100 µL /sample).

Dilution of EHS-substrate resulted in a significant strain increase at equal sled displacement of 5 mm from 5.3% to 10.1% (92% increase, CIs: Pure EHS-gel=4.2 to 6.4%; Diluted EHS-gel=8.6 to 11.7%) (figure 30 B). The shear modulus of pure and diluted EHS-gel was determined via rheometry. Rheometric measurements were kindly performed by Susan Babu (DWI-Leipniz Institute for Interactive Materials, RWTH University (for details, see chapter 2.10.8). Rheometric analysis revealed a decrease of storage modulus from 55 Pa (CI= 50.1 to 60.7 Pa) in pure EHS-gel to 28 Pa (CI= 25.0 to 31.0 Pa) in diluted EHS-gel (decrease to 50.9%) (figure 30 C). In accordance with Hooke´s Law is the product of shear strain and EHS-gel shear modulus identical as it should be the case at equal applied force. This product is the applied shear stress at 5 mm sled displacement. This result showed that the shear stress device could not only be utilized to strain ultra-soft hydrogels but also to determine differences in substrate stiffness. Moreover, assuming a poisons ratio of 0.5, as is common for a soft, incompressible material, the shear modulus of 55 Pa for pure EHS-substrate results in a Young´s modulus of 165 Pa (3) [210]. This result is well in line with the reported Young´s modulus of 167 Pa for EHS-substrate [4].

(3) $E = 2G\ (1 + v)$

E= Young´s modulus; G = Shear modulus; v = Poissons ratio

In essence, it was shown that the shear stress device could be used to create reproducible solid shear strain in hydrogels of varying stiffness. Further, the software developed by Dr. Ronald Springer was verified to allow for the precise determination of strain amplitude in microsphere-laden hydrogels.

3.1.3 Strain in hydrogel-embedded MCF 10A spheroids

The goal for developing this device was to enable studies on the effect of solid shear stress on breast epithelial tissue *in vitro*, mimicking as many aspects of the mechanical environment of the mammary gland as possible.

To this end, EHS-gels were utilized to characterize shear stress device-generated strain in hydrogels. This was done as EHS-gel stiffness and biochemical composition closely resemble natural mammary tissue and allow for generation of physiological breast epithelial spheroids with the MCF10A cell culture model cell line.

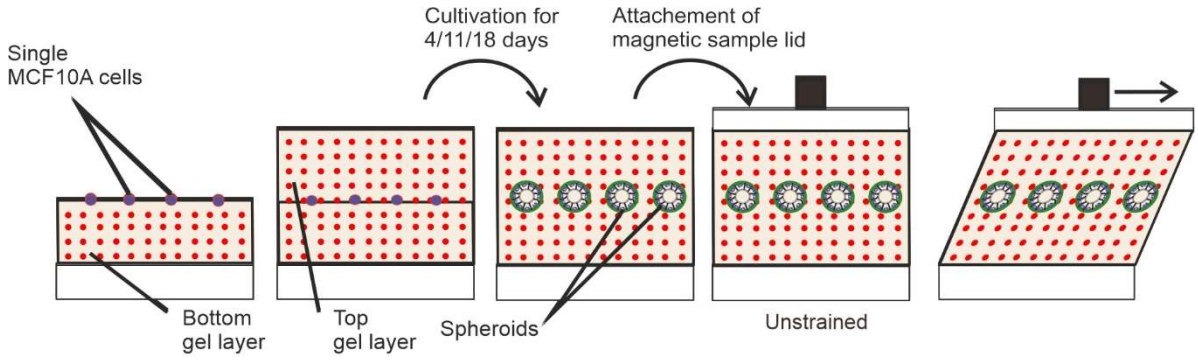

Figure 31: MCF 10A spheroid cultivation in hydrogel sandwich. Schematic of sample creation for shear straining of MCF10A spheroids. Single MCF10A cells are embedded in between two layers of EHS-gel. Samples are then equipped with a magnetic sample lid for shear stress experiments. Adapted from [204]

For stress application to breast epithelial spheroids, a LiveAct-RFP-transduced MCF10A cell line was used. This cell-line was produced by Dr. Aljona Gaiko-Shcherbak via viral transduction of wild-type MCF10A cells with a LiveAct-RFP vector. The LiveAct-RFP fusion protein produced by these cells contains a peptide that binds to filamentous actin without interfering with cytoskeletal dynamics and a red fluorescent protein (RFP). Thereby is live cell imaging (LCI) of actin dynamics enabled, allowing for analysis of cellular morphology and motility during stress application.

Single MCF10A LiveAct RFP cells were embedded in the middle of two layers (100 µL bottom and 50 µL top layer) of microsphere-laden EHS-gel (figure 31) followed by standard 3D cultivation protocols established in our group (for details, see chapter 2.9.4). Earlier work

showed that MCF10A cells undergo a progressive development resulting in lumen-bearing spheroids with a physiological BM and differentiated, polarized epithelium [70]. First, it had to be ensured that the new two-layer cultivation approach, or the expression of LiveAct-RFP fusion protein, did not alter the well-defined MCF 10A spheroidal development process. MCF10A LiceAct-RFP spheroids grown in between two EHS-gel layers were transferred to glass cover slides (for details, see chapter 2.9.5) for immunocytochemical treatment (for details, see chapter 2.12) before analysis via confocal imaging (for details, see chapter 2.13) (Figure 32).

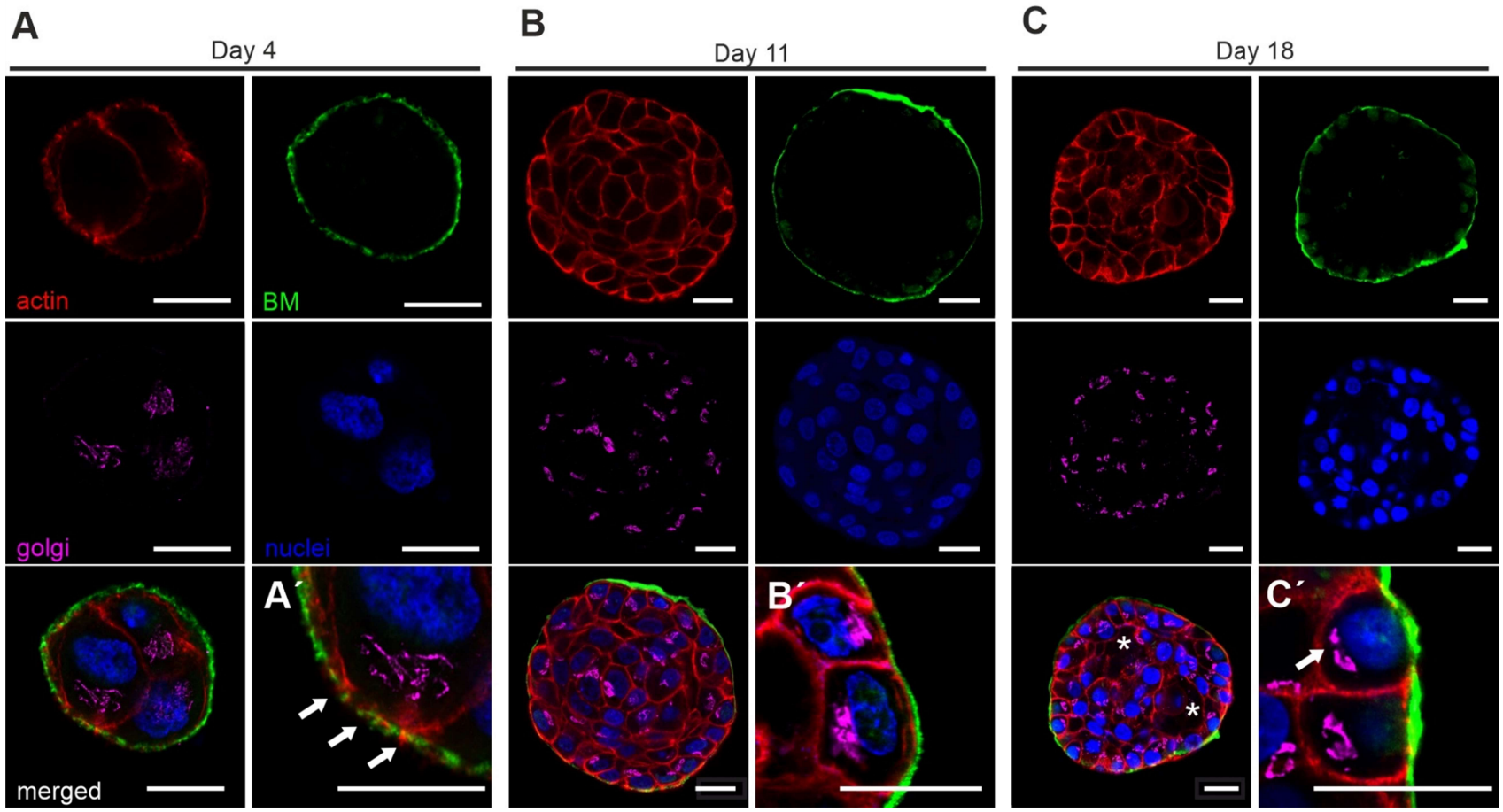

Figure 32: **MCF10A cells undergo normal development in hydrogel sandwich.** (*A-C*) Representative micrographs of spheroids cultivated over 4 to 18 days in between two EHS-gel layers as shown in Figure 31. Spheroids were transferred onto cover glasses, foxed and immunofluorescently stained. Confocal images were acquired in the equatorial plane of spheroids demonstrating BM formation (collagen type IV, green), cellular orientation of the Golgi apparatus (GM130, magenta), the actin cytoskeleton (F-actin, red) and cell nuclei (DRAQ-5, blue). White asterisk highlight partial lumen clearance. (A´) Magnification of A highlights the presence of a thin BM penetrated by actin protrusions (B'). Magnification of B highlights a developed BM and cellular orientation of the Golgi-apparatus. (C') Magnification of C highlights complete basoapical polarization of the outer cell layer. Scale bars = 20 µm. Adapted from [204]

The MCF10A LiveAct RFP cells cultivated in between two EHS-gel layers underwent normal spheroidal development (for details, see chapter 1.2.3) as indicated by a BM formation, cellular polarization and lumen development (Figure 32). In detail, the actin signal was observed to be cortical, while the collagen IV signal confirmed a basal BM formation toward the EHS-gel. As described for young spheroids with a thin, low-developed BM, actin-rich protrusions were frequently observed on day 4 of cultivation (Figure 32 A´) [34]. Spheroids were mostly polarized on day 11 of cultivation, as indicated by intracellular apical Golgi and basal nuclei orientation (Figure 32 C´). At day 18 of cultivation, the outer cell layer of spheroids was fully polarized (Figure 32 D´) and partial lumen clearance was evident by the combined absence of F-actin, nuclei and Golgi – signal (Figure 32 D, asterisk). In essence, two-layer EHS-gel cultivation and LiveAct RFP expression did not change the spheroidal development of MCF10A. Therefore, the two-layer cultivation system could be used to grow MCF10A LiveAct RFP spheroids with physiological features. All further described MCF10A spheroids were derived from the LiveAct-RFP transduced cell line and are hereafter referred to as spheroids.

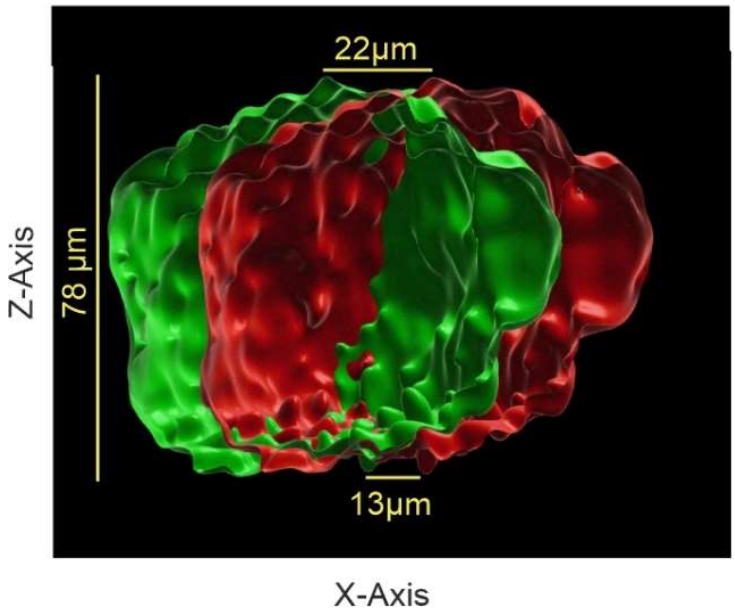

Figure 33: Solid shear strain in hydrogel embedded MCF 10A spheroids. Superimposed surface renditions for actin signal in an unstressed (green) and stressed MCF10A LiveAct RFP spheroid. Surface rendition was performed with Imaris with the build in automated creation routine. Images were created with imaris 3D viewer tool. Image stacks were acquired in fast airy mode with optimal Z-resolution over a distance of 100 µm at 0.7 x optimal pixel size as calculated by Zen Black software. Adapted from [204]

Spheroids cultivated for 11 days were exposed to ECM stresses by 5 mm sled displacement in the shear stress device. Strain in spheroids was determined via Z-Stack imaging of the LiveAct RFP (actin) signal. Imaging data of a spheroid before and after stress application was superimposed and surface renderings were created from the captured actin signals (Figure 33). Measurement of displacement of distinctive features of surfaces revealed an increase of displacement with height, confirming shear strain in the spheroid. Next, strain in spheroids was determined quantitatively to analyze their mechanical behavior.

3.2 Computational determination of strain in spheroids

The same image analysis approach described in 3.1.3 was utilized to analyze strain in spheroids cultivated for 11 days quantitatively. Therefore, the displacement of actin signal upon stress application was determined via cross-correlation-based template matching at multiple focal planes (Figure 34 A). Subsequent linear regression of mean displacement determined for each focal plane revealed shear strain amplitude in spheroids (Figure 34 B). Simultaneous acquisition of actin and fluorescent microsphere signal allowed for determining strain in spheroids and their surrounding matrix (Figure 34 C). All subsequent measurements regarding shear strain in spheroids and hydrogels were performed like this.

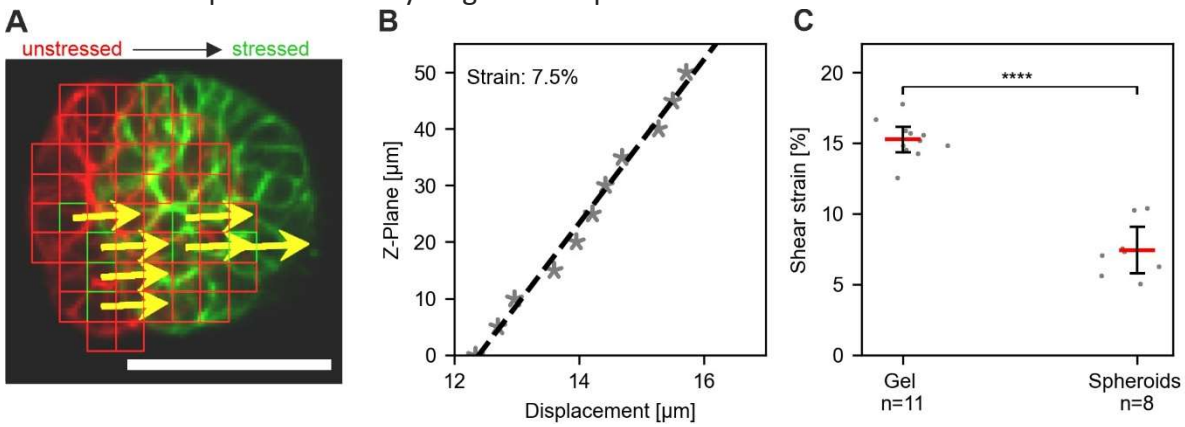

Figure 34: Computational analysis of microsphere displacement. MCF-10A Liveact RFP spheroids were cultivated in between to EHS-gel layers for 11 days before stress application(A) Representative image of determined actin displacements for templates (39 x 39 px) in an individual focus plane with s search length of 100 px in y,-y and -x and 300 in x direction. Yellow arrows show determined displacement vectors (true scaling). The cross-correlation threshold for pattern matching was 0.5. Scale bar = 50 µm (B) Linear regression (dashed line) of displacement at multiple focal planes was used to determine the shear strain within the spheroid. Each data point represents the median displacement of all detected displacement vectors in the respective plane. Value 0 µm: indicates the first plane of the recorded image stack (absolute gel height >500 µm). The local strain was calculated from the slope of the regression line. (C) Scatter plots of shear strain measured at n positions in spheroids and the surrounding EHS-gel. The threshold for linear regression was $r^2 > 0.7$. For statistical tests, Mann–Whitney U-test was used with: **** = $p \leq 0.0001$. Adapted from [204]

For spheroids, the local strain could be determined with an $r^2 > 0.7$ for fewer positions than in the gel (gel: n=11; spheroids: n=8). This was attributed to cellular movement in between the acquisition of the unstressed and stressed image stack (~5 minutes). Thus, actin patterns changed due to cell movement, which hindered successful pattern matching. Still, this analysis revealed that average measured strains in MCF 10A spheroids were significantly lower than the strains measured in the surrounding gel. In detail, the average strain amplitude in spheroids was 7.5% (CI: 55.7 to 9.1%), while the average strain in the gel measured at the same positions was 15.3% (CI: 14.3 to 16.1%). From this was deducted that spheroids were resistant to EHS-gel transmitted solid shear strain. Of note, the linearity of strain in the EHS-gel as shown in figure 29 was maintained, indicating a seamless connection between the two hydrogel layers.

3.1.5 Shear strain resistance depends on the spheroidal developmental stage

Previous work has described the MCF 10A BM as a mechanical barrier that stiffens and thickens during maturation [72]. Therefore, it was theorized that the mechanical resistance of MCF 10A spheroids is dependent on the developmental status of the spheroids and, thereby, the maturation stage of their BM. Spheroids' mechanical resistance was analyzed by measuring shear strain in spheroids and hydrogels after 4, 11 or 18 days of cultivation (Figure 35).

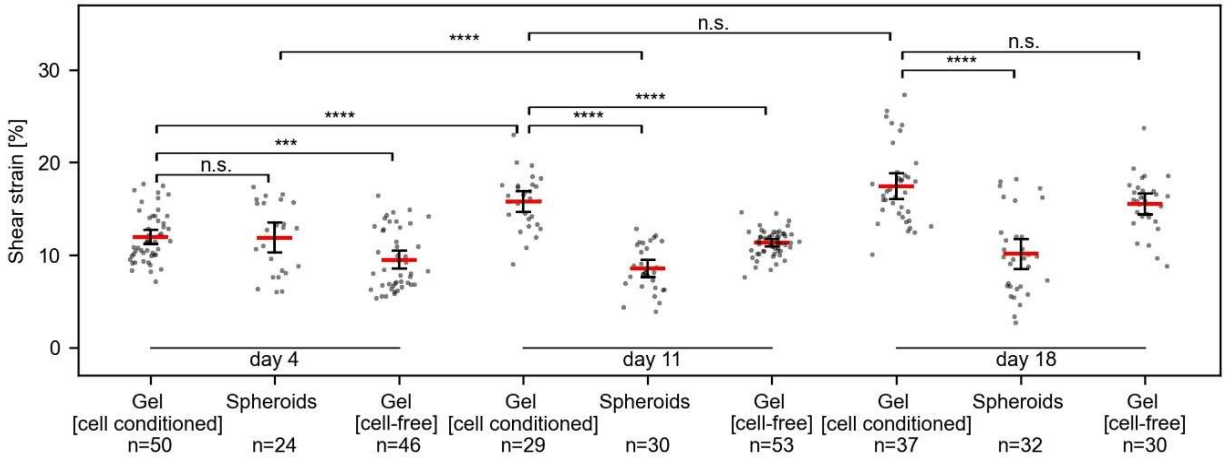

Figure 35: Breast spheroids gain shear strain resistance with advanced basoapical polarization. Scatter plots summarize the measured shear strain in hydrogels MCF10A spheroids with different maturation stages, hydrogels populated by spheroids (cell-conditioned) and cell-free hydrogels. Strain was measured at 5 mm sled displacement. N = total number of measured positions for three individual gels. Scatter plots: bars: median with 95% confidence interval. For statistical tests, Mann–Whitney U-test was used with: **** = $p \leq 0.0001$, *** = $p \leq 0.001$, * = $p \leq 0.05$. Adapted from [204]

Based on this analysis, several interesting observations could be made. Regarding the initial hypothesis of strain resistance correlating with spheroid maturation state, spheroids' strain decreases significantly from day 4 to day 11 of cultivation (mean of 11.9% to 8.5%). This trend also applies to strain measurements in spheroids at day 11 and day 18 of cultivation, even though the increase is not significant (mean of 8.5% to 10.1%, n.s.).

The difference in strain measured for spheroids and their surrounding gel was found to be significant on day 11 (means of 8.5% and 15.8%) and day 18 (means of 10.1% and 17.4%) of cultivation but not on day 4 (means of 11.8% and 11.9%) of cultivation. These results suggested that a mechanical resistance of MCF 10A spheroids is indeed developed during spheroid maturation.

Strikingly, a cultivation time-dependent increase in strain amplitude was observed in EHS-gels (mean of 11.9%: day 4; 15.8%: day 11; 17.4%: day 18). As described in chapter 3.1.4, strain amplitude in EHS-gels is dependent on the stiffness of the gel. Based on these observations, it was concluded that the increase in strain during cultivation resulted from a decrease in the stiffness of EHS-gels. This was believed to be the result of ECM remodeling processes performed by the embedded spheroids. Therefore, no cultivation-time-dependent increase in strain should be observed in cell-free gels.

However, cultivation time-dependent strain increase was also observed in cell-free gels. Here, a significant increase of strain was measured between day 4 (mean 9.5%) and day 11 (11.3%) as well as between day 11 and day 18 (15.3%) of cultivation. On day 4 and day 11, the difference in strain amplitude was also found to be significant for cell-free and cell-conditioned gels. How this could be explained will be discussed in detail in chapter 4.

To summarize, spheroids were observed to develop a strain resistance correlating with BM development and cellular differentiation. After this characterization and verification, cellular reactions to solid shear strain were studied.

3.1.6 Cell viability and diffusion analysis

It has been shown that by using the novel shear stress device, it was possible to create and characterize solid shear strain in hydrogels and in embedded MCF10A spheroids. Further, the mechanical resistance of spheroids was analyzed regarding their developmental state.

Next, I analyzed the cellular reaction of spheroids to prolonged cyclic solid shear stress using live cell imaging (LCI) and immunocytochemistry. For this, optimal cell culture conditions during prolonged stress application had to be verified first.

Performing experiments with living cells over prolonged periods, e.g., 24 hours, requires care regarding cell viability. During such experiments, it has to be ensured that inadequate cell culture conditions do not compromise normal cell function and metabolism. To test whether optimal cell culture conditions are met within samples prepared for shear straining, a control sample was imaged for a period of 24 hours. The sample was created by cultivating spheroids in between two EHS-gel layers, as described in chapter 3.1.3. After the attachment of a magnetic cover lid, samples were covered in 3 mL AM- media supplemented with 25 mM HEPES and sealed with Parafilm to ensure a stable pH and a humidified environment for 24 hours. Samples were then placed into the shear stress device without the sleds´ magnets. Spheroid viability was analyzed by confocal imaging of the actin signal at the beginning (0 h) and the end (24 h) of a 24-hour period (Figure 36). During this time, the microscope's incubation chamber was tempered at 37 °C.

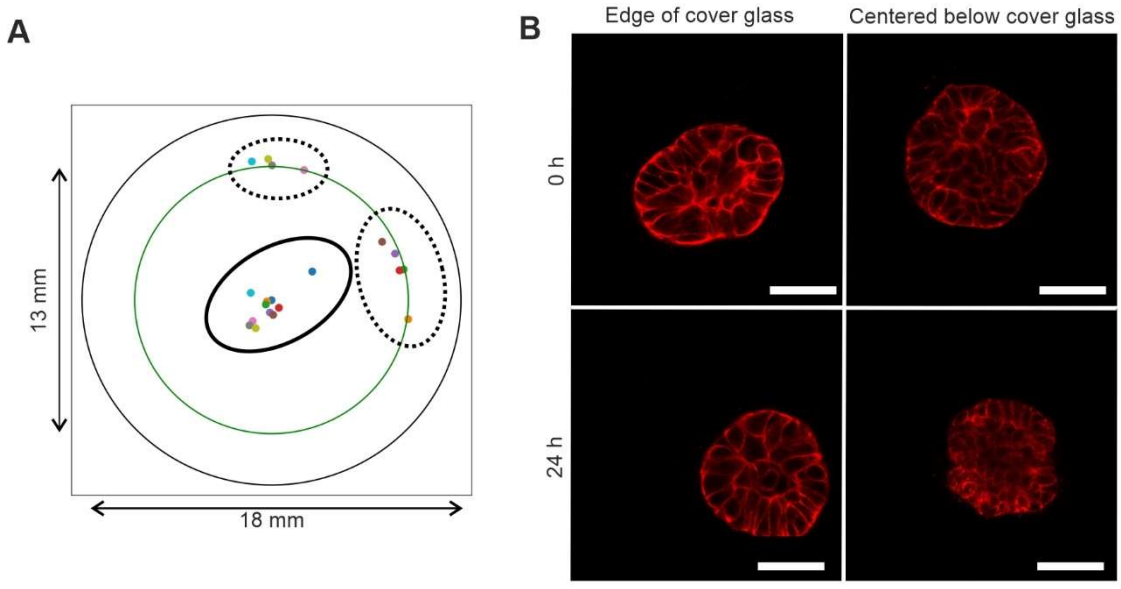

Figure 36: The magnetic lid affects cell culture conditions. Samples of MCF10A LiveAct RFP spheroids (day 11 of cultivation) embedded in EHS-gel equipped with a magnetic lid were imaged for 24 h to observe cell viability. (A) Depicts position of analysed spheroids in the 18 mm geltrex filled inner well of a sample dish. The green circle represents the area covered of EHS-gel covered by the magnetic lid. The positions were chosen to be directly centred under the magnetic lid (ellipse) attached to the top of the gel or at its edge (dashed ellipses). (B) Micrographs of spheroids imaged directly after attaching the magnetic lid to the sample (0 h) or after 24 h. The same spheroid is shown, respectively, at 0 h and 24 h. Scale bars = 50 µm.

At the beginning of the experiment (0 h), spheroids displayed normal morphology described by cellular cortical actin that indicated a continuous cell-cell connection and a smooth surface at the cell-ECM interface. Interestingly, it was observed that spheroids beneath the magnetic lid rounded off and displayed a fading actin signal after 24 hours that was less clearly lining the cell-cell interfaces and was increasingly diffuse. The actin signal at the cell-ECM interface was not smooth anymore but changed to small protuberances. While this change may appear subtle, it was a strong indicator of a suboptimal, potentially lethal environment for the cells. Spheroids positioned outside the perimeter of the magnetic lids cover glass or at its edge however displayed a normal phenotype. In essence, the general sample preparation does not seem to affect normal spheroid morphology, but the magnetic lid does.

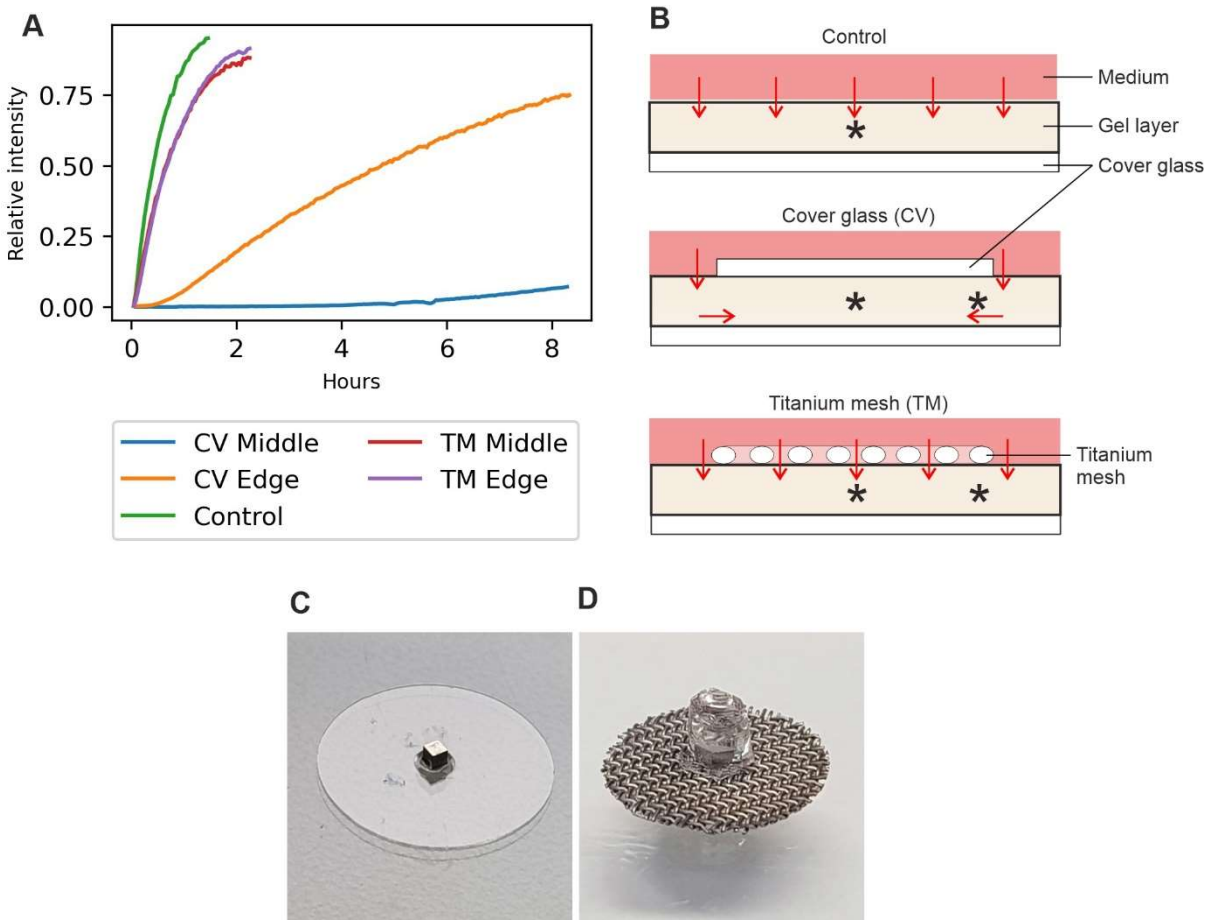

Figure 37: Dextran diffusion into EHS-gels is slowed under a magnetic lid. (A) The average fluorescence intensity of of Texas-red conjugated dextran tracer was determined over time in EHS-gels covered by a magnetic lid made with a cover glass, a magnetic lid made with titanium mesh or not covered (control). (B) Schematic depict position for image acquisition of A and a proposed path for soluble diffusion from the medium into the EHS-gels (red arrows) for each condition. (C) A magnetic lid made with a cover glass (D) A magnetic lid produced with a titanium mesh. The magnet is coated with PDMS. C & D Adapted from [204]

These observations indicated that the diffusion between the fluid in the EHS-gel and the overlayed media was blocked by the magnetic lid. This limits the exchange of nutrients and metabolic by-products of the cells resulting in evidently inadequate cell culture conditions below the cover glass. Simply, solvent exchange between gel and media is limited to the area outside the perimeter of the cover glass. Testing this theory, EHS-gel samples with or without a magnetic lid were created to investigate whether the cover glass diminished the diffusion speed of components from the media to the gel. For this, samples were overlayed with medium containing dextran tracers (10 kDa, 200 µg/mL) conjugated with the fluorophore Texas. Their diffusion from the medium to the EHS-gel was tracked by fluorescence imaging of Texas red signal every 2.5 minutes within the EHS-gel at ~150 µm at multiple positions. The average fluorescence intensity for each image was then normalized with the average fluorescence intensity of Texas red signal in a 200 µg/mL dextran solution on a cover glass (for details, see chapter 2.10.9).

Thus, dextran tracer diffusion into the gel was determined by capturing the relative increase in Texas red signal (figure 37 A).

This semi-quantitative analysis confirmed that the diffusion of the dextran tracer was vastly slower if the gel was equipped with a magnetic lid. Intuitively, the fluorescence intensity of dextran tracers in the gel was higher at the edge of the cover glass than at its center, indicating that the dextran tracers enter the gel at the edge of the cover glass, creating a concentration gradient with its lowest concentration at the center (figure 37 B). This observation perfectly explains why spheroids directly under the cover glass displayed signs of unsuitable cell culture conditions.

To solve this problem, the cover glass of the magnetic lid was exchanged for a titanium mesh with 20% open area. Repeating the diffusion measurement in a gel equipped with a titanium mesh-magnetic lid revealed a substantially faster diffusion of the dextran tracers into the gel compared to cover glass-magnetic lid samples (figure 37 A & B). These diffusion measurements were only rudimentary and did not fully capture the diffusion characteristics of dextran tracers into the hydrogels. Still, they showed titan meshes utilization for magnetic lid restores diffusion speed almost completely.

To further avoid sample preparation from negatively affecting cell culture conditions, it was decided to cover the magnetic lids magnet with a PDMS layer. This was done to circumvent

the possibility of toxic effects stemming from the magnet's Ni-Cd-Ni coating, which was submerged in media during experiments.

EHS-gel samples with MCF10A spheroids cultured for 11 days were subsequently equipped with a magnetic titanium mesh. Fluorescent imaging of these spheroids over 24 hours showed that normal cellular morphology was maintained even for spheroids directly beneath the magnetic lid. Thereby, optimal cell culture conditions in shear stress samples were established by employing a magnetic lid produced with a titanium mesh.

3.1.7 Cyclic stress triggers mechanoresponse in undifferentiated spheroids

The motor control unit driving the magnetic sled of the shear stress device is programmable with regards to drive amplitude, speed and dwell time, allowing for stress application protocols to be defined. As described in chapter 1.2 is, the breast gland constantly subjected to shear strain of varying amplitude based on breast support and activity.

So far, strains generated in gels with the shear stress device have been defined for up to 5 mm sled displacement, at which strains of up to ~20% have been observed (for details, see chapter 3.1.5). As these were seen as reasonably natural strain amplitudes in non-exercise situations, 5 mm sled displacement was used in cyclic straining experiments as amplitude. As for sled displacement speed, it was necessary to operate the motor at no more than 4 mm/s to avoid overheating, resulting in a frequency of 0.4 Hz for a full cycle from the neutral position to the maximum amplitude and back to the neutral position. While employing stress with this protocol (5 mm amplitude, 0.4 Hz, 0 s dwell time) to hydrogels, it was observed that embedded spheroids were moving out of the microscope's field of view within the first 2 hours of experiments.

This observation was attributed to viscoelastic creep. To balance this deformation of the hydrogel, it was decided to alter the stress protocol by applying the stress bidirectional. This was realized by starting the cycle at a sled position of - 5 mm from the neutral position but still moving to a +5 mm position (Figure 38). This adaption reduced the frequency to 0.2 Hz at 4 mm/s sled speed but solved the problem of spheroids moving out of the microscopes' field of view during experiments. As stress was applied bidirectionally, the mechanical load was not changed due to the lowered frequency.

The adapted protocol was hence employed during investigations on cellular reactions of mammary epithelial spheroids to mechanical straining. Henceforth, cyclic straining refers to cyclic sled displacement from -5 mm to +5 mm, relative from the centered starting positions, at 0.2 Hz (figure 38).

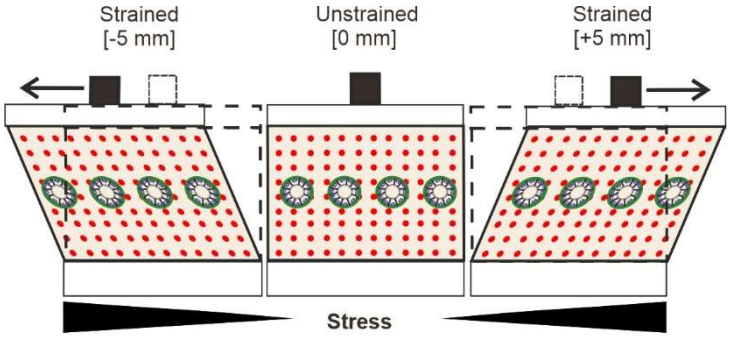

Figure 38: Cyclic stress application principle. Adapted from [204]

To investigate the dependency of mammary epithelial mechanoresponses on breast gland development, spheroids cultivated for 3 to 4 days or 10 to 11 days in EHS-gels were cyclically strained for 22 hours. The actin signal of spheroids was imaged before and after stress application to perform a visual analysis of cellular morphology and spheroidal organization. Control samples were produced identically but were not stressed with the shear stress device. The results are summarized in Figure 39.

The acquired fluorescence images revealed that cells of spheroids at day 3 or 4 of cultivation are <50 µm in diameter and consist of ~5-10 cells. Actin was localized to the cortex, seamlessly lining cell-cell and cell-matrix interfaces. In spheroids cultivated for 10 to 11 days, the cellular actin distribution appeared similar but the cellular organization was different. After 11 days of cultivation, the cells often organized into an outer cell layer of basoapical polarized, elongated cells. This morphology did not change due to stress application. 3-day-old spheroids on the other hand, displayed interesting changes in actin organization in response to cyclic straining. Here, stress application resulted in a round shape of cells. While cortical actin was not diffuse, it was also no longer lining cell-cell interfaces resulting in small gaps between cells.

Further, spheroids were often found to be no longer round but cells bulged out from the spheroid body.

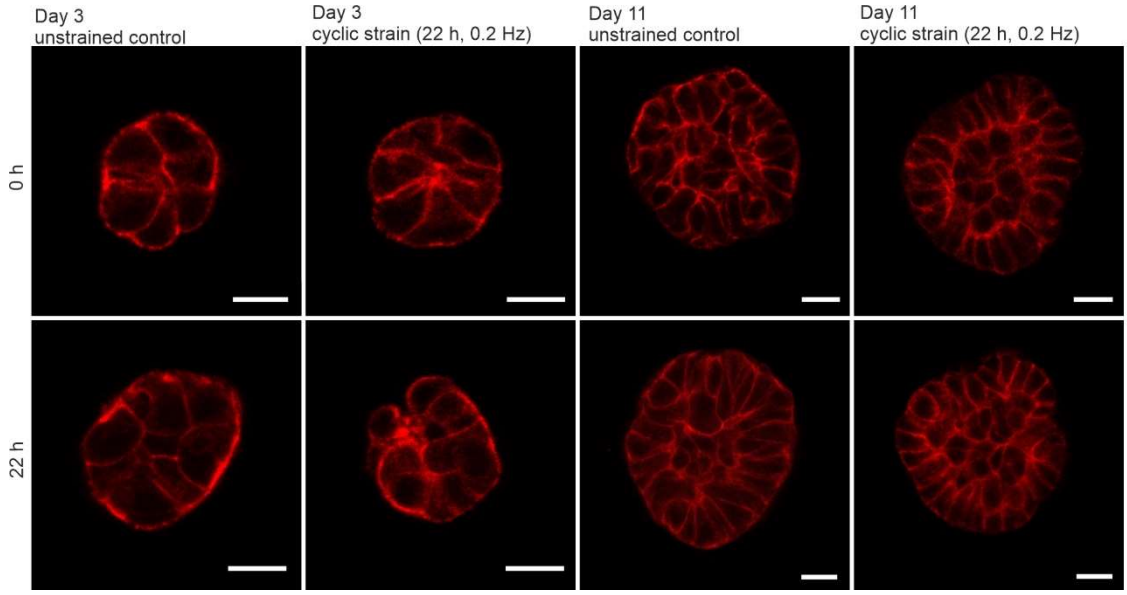

Figure 39: MCF 10A spheroid morphology is altered by cyclic shear stress application. MCF10A LifeAct RFP spheroids were cultivated for 3 and 11 days before being subjected to cyclic strain for 22 h (0.2 Hz, -5 to +5 mm, 0.2 Hz). Representative images of the spheroids before (0 h) and after (22 h) stress application or controls not subjected to mechanical loads with the shear stress device. The same spheroid is shown respectively for all conditions at their equatorial plane. All scale bars = 20 µm.

These observations indicated that cell-cell contact and cell-BM contact might have been reduced in undifferentiated spheroids cultivated for three days in response to cyclic shear straining. In differentiated spheroids cultivated for 11 days, this effect seemed to be completely absent.

While these results indicated that the mechnoresponsitivity of MCF 10A spheroids depends on cellular differentiation, more substantial evidence was necessary to form a concrete hypothesis on the matter. LCI was therefore employed next to define the timeframe of the observed morphology changes of undifferentiated MCF 10A spheroids in response to prolonged cyclic stress.

MCF 10A/Liveact RFP spheroids were cultivated for 3 or 10 days before applying cyclic stress for 22 h. During stress application, the actin signal was captured every 30 minutes at the equatorial plane of spheroids with a confocal microscope.

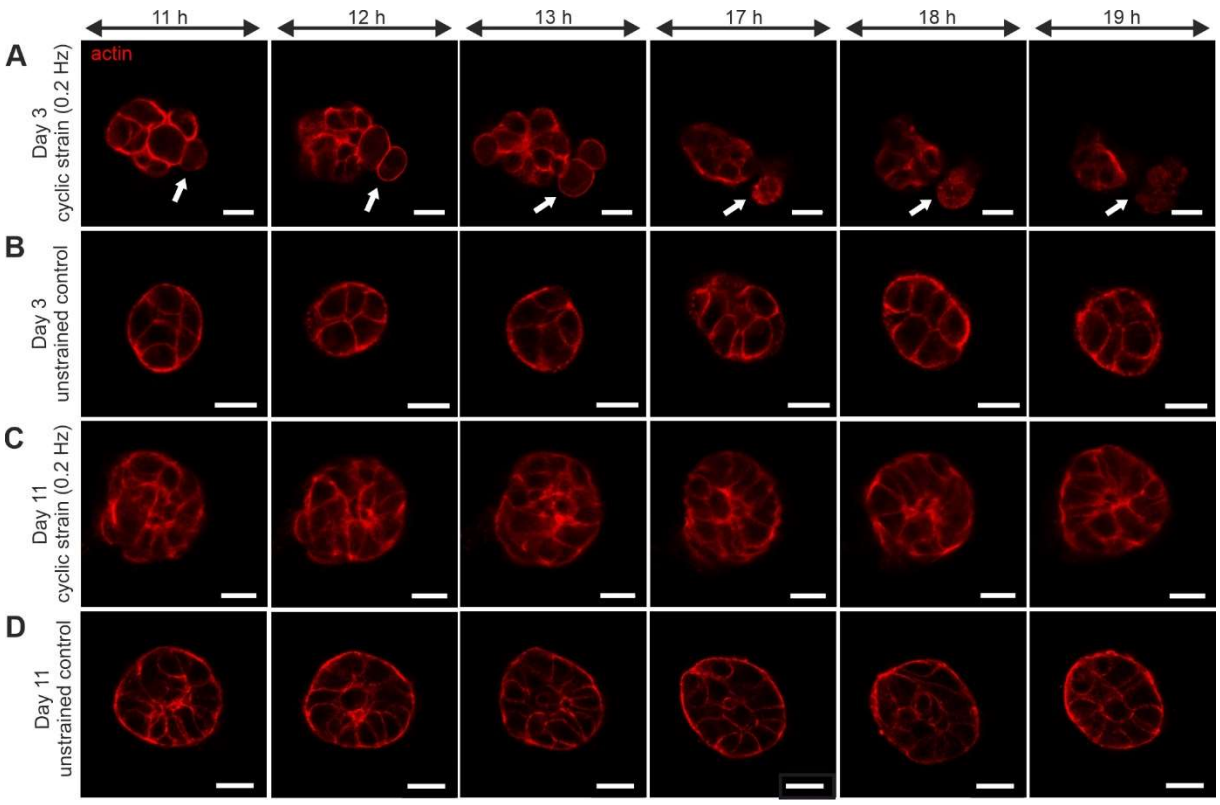

Figure 40: Long-term cyclic shear strain triggers cell extrusion in very early developmental stages of breast spheroids. MCF10A Lifeact RFP spheroids were cultivated for 3 and 11 days and then subjected to cyclic straining. Actin signal of spheroids was captured every 30 minutes at the equatorial plane during stress application. (A) Image series of an undifferentiated spheroid during cyclic straining. White arrows indicate cells that are extruded from the spheroid body. (B) Corresponding image series of a representative undifferentiated spheroid not subjected to cyclic straining (C) Time series of a representative differentiated spheroid during cyclic straining (D) Time series of a representative differentiated spheroid not subjected to cyclic straining. All scale bars = 20 µm. Adapted from [204]

Supporting the previous observations, no changes in morphology were noticed for spheroids cultivated for 10 to 11 days in response to stress application (Figure 40 C). This was also found to be true for unstressed spheroids regardless of differentiation state (Figure 40 B & D). Moreover, these spheroids appeared to perform a rotational motion, which is reported to be normal behavior for MCF 10A spheroids in EHS-substrates [211]. These findings further prove that sample preparation does not appear to have any adverse effects on gel-embedded cells during the experimental period. Any alteration in normal behavior can therefore be addressed as a direct effect of mechanical stress application.

As observed before, loss of spheroidal structure and round morphology of cells was observed in undifferentiated spheroids subjected to cyclic straining. More strikingly, it was found that some spheroids extruded single or pairs of cells from the spheroid in the equatorial plane

(2/18 spheroids observed). Further, the actin signal of extruded cells completely faded within hours after ejection (Figure 40 A). This indicated apoptosis, a programmed cell death process in which F-actin cleavage is a hallmark feature [212]. Both movement of spheroids in the gel out of the focal plane, focus drift and gel deformations can obscure LCI data as observed spheroids move out of the field of view. It was likely that cell extrusion events occurred not only in the observed focal plane but at any other position on the spheroids. Due to technical limitations, the occurrence of cell extrusion events could not be accurately determined by LCI of single focal planes. Instead, it was decided to employ immunocytochemical treatment to analyze the occurrence of apoptosis after stress application.

3.1.8 Cyclic shear stress triggers apoptotic cell death in MCF10A spheroids

Cells extruded from MCF 10A spheroids under cyclic strain completely lost their actin signal within several hours after ejection. This observation was attributed to being most likely an apoptotic event. Apoptosis is a form of controlled cell death in which F-actin is cleaved by proteolytic caspase proteins. To verify apoptotic events, the presence of active Caspase-3 (cleaved Caspase-3; cC-3) in the vicinity of spheroids was analyzed (table 10).

Table 10: Quantification of cC-3 positive spheroids after stress application.

Sample	cC-3 Positive spheroids	cC-3 Negative spheroids	% Positive spheroids	Mean hydrogel strain
Day 3/4 stressed	39	16	71	8.2%
Day 3/4 unstressed	8	46	14	-
Day 10/11 stressed	6	45	12	10.2%
Day 10/11 unstressed	8	54	13	-

Samples shear strained as described in 3.1.8 were therefore fixed after cyclic stress application and were immunocytochemically treated for fluorescent labeling of cC-3 (for details, see chapter 2.12).

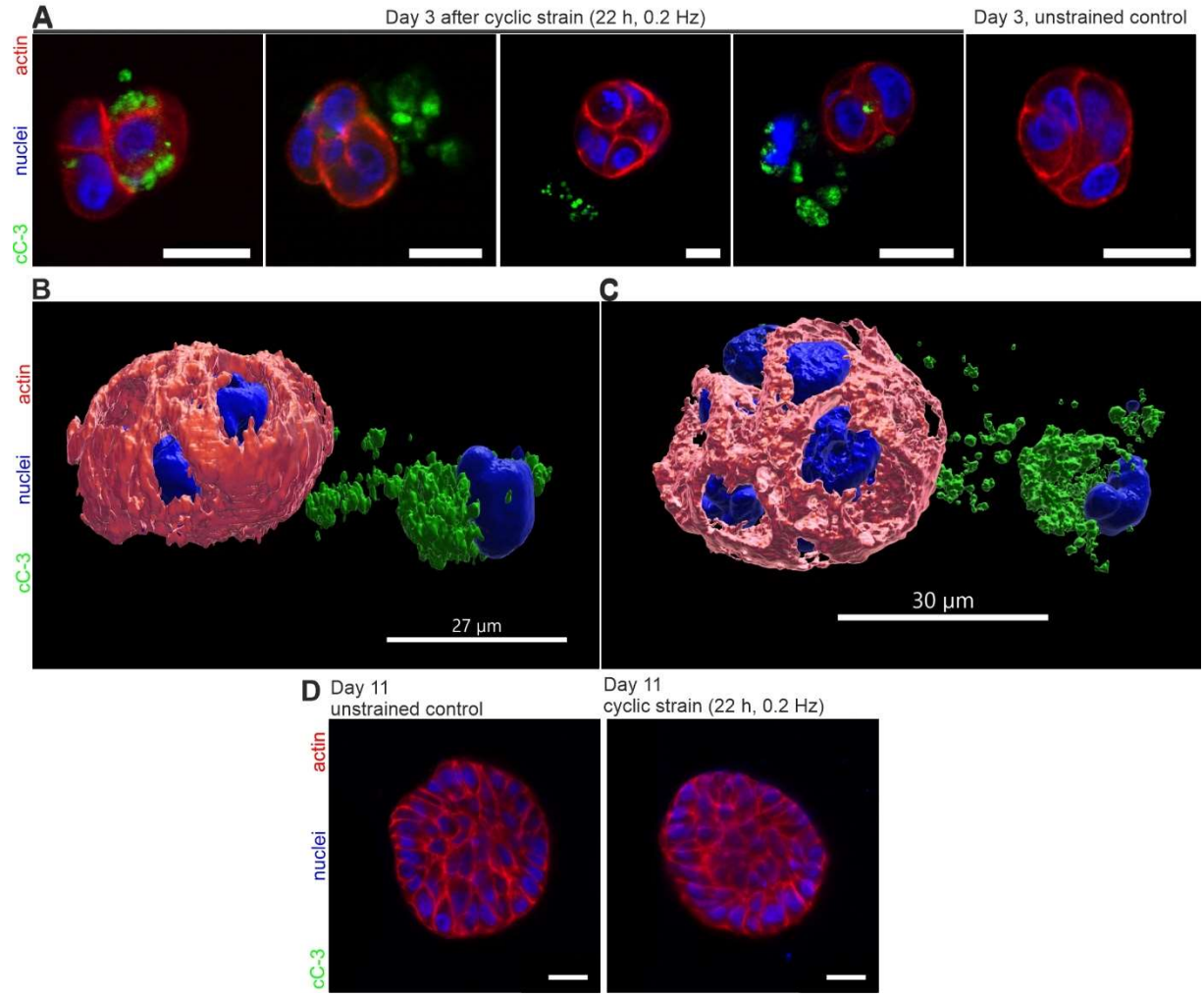

Figure 41: Cyclic strain triggers apoptosis in early spheroid development. MCF10A LiveAct RFP spheroids were subjected to cyclic strain for 22 h after cultivation for 3 or 11 days. All micrographs depict the equatorial plane of spheroids. (A) Micrographs of four individual spheroids cultivated for 3 days before stress application. Samples were fixed and immunofluorescently labeled (for details, see chapter 2.12) against cleaved Caspase-3 (cC-3) protein after 22 h of cyclic straining. A representative spheroid for an unstrained control is also shown. All scale bars =20 µm. (B & C) 3D surface reconstruction of an image stack of a spheroid subjected to the same treatment as spheroids in A at day 3 of cultivation. B shows the spheroid from the side while C shows the spheroid from the top. 3D surface reconstruction was performed with Imaris. (D) Spheroids cultivated for 11 days treated equally to A. Scale bars = 20 µm. Adapted from [204]

The presence of cC-3 signal was interpreted as an apoptotic event. Interestingly, the signal of cC-3 was found frequently in the vicinity of stressed spheroids at day 3 or 4 of cultivation (71%) (Table 10) (figure 41 A-C). In unstressed controls of spheroids cultivated for 3 to 4 days, cC-3 signal was found less often (14%). Therefore, cyclic shear straining resulted in a drastic increase of apoptotic events in undifferentiated spheroids at day 3 to 4 of cultivation. For differentiated spheroids cultivated for 10 to 11 days, no increase in apoptotic events was observed in response to cyclic shear straining. Here, 12% of spheroids were observed to be

positive for cC-3 signal after cyclic straining while 13% of spheroids were found to be cC-3 positive in unstressed controls.

The cC-3 signal was, as expected, often found to be condensed into smaller than a cell, round bodies which often contained or were close to nuclear signal indicated by DAPI staining. This observation fits well to the description of apoptotic bodies [213]. Interestingly, it was also observed occasionally (~25% of 55 spheroids) that both cC-3 signal and fragmented nuclei were in contact with the remaining spheroidal body. These observations indicated that extruded cells underwent apoptosis. They also suggest that cell extrusions are much more frequent than initially observed. However, it remains unclear whether cells start apoptotic signaling cascades before or after extrusion from the spheroid.

Taken together, both the changes in cellular spheroidal shape during stress application as well as the apoptotic cell extrusion in undifferentiated spheroids show that the mechanoresponse of the MCF10A cell line is dependent on spheroid developmental status and cellular differentiation. The meachano- sensing and transduction mechanisms involved in this mechanoresponse to cyclic shear stress, however, remain unclear.

3.1.9 Outlook: Mechanosensitive ion channels in MCF10A spheroids

This chapter summarizes the preliminary results on investigations on the possible mechanosensitive element that drives cell extrusion of MCF10A spheroids in response to cyclic shear strain. Thus, these investigations are ongoing and not final.

Blocking of mechanosensitive ion channels alleviates shear strain response

As will be discussed in chapter 4, multiple signaling pathways that drive epithelial cell extrusion are directly or indirectly connected to the activation of mechanosensitive ion channels (MSCs). Therefore, the potential role of MSCs for cell extrusion as a mechanoresponse in MCF10A spheroids was investigated.

Table 11: Quantification of cC-3 positive spheroids after $GdCl_3$ treatment.

Sample	cC-3 Positive spheroids	cC-3 Negative spheroids	% Positive Spheroids	Average EHS-gel strain
3 day stressed (n=2)	34	29	54	11.2%
3 day stressed +20 µM $GdCl_3$ (n=2)	1	59	2	12.4%
3 day unstressed +20 µM $GdCl_3$ (n=1)	4	26	13	-

Several pharmacological compounds can be used to block mechanosensitive ion channels selectively [214]. Among those is $GdCl_3$ which is used to block mechanosensitive ion channels unspecifically with variable affinity by dissipation of Gd^{3+} in aqueous solution [215]. To test whether the mechanoresponse of spheroids was dependent on any mechanosensitive ion channels, $GdCl_3$ was employed. Undifferentiated spheroids were cyclically shear stressed under the conditions described in 3.1.8. The media of treated samples contained 20 µM $GdCl_3$ while the respective amount of water was added as solvent control to untreated samples. After stress application, samples were fixated and immunocytochemically treated to quantify apoptotic events. As expected, 54% of spheroids in untreated shear-strained samples were found to be positive for cC-3 (table 11). The Percentage of cC-3 positive spheroids in shear-strained samples was dramatically reduced by $GdCl_3$ treatment. Therefore, blocking mechanosensitive ion channels was highly effective in stopping apoptotic cell extrusion in stressed spheroids. These results indicated that MSCs are the driving element in the here-described apoptotic cell extrusion. However, repetition of the experiments should be conducted before drawing definitive conclusions.

Piezo1 expression levels are modified by cellular differentiation

Alteration of the MSC protein Piezo1 expression levels of MCF10A cells was analyzed regarding the developmental stage of spheroids. For this, spheroids were analyzed for the presence and localization of Piezo1 at different development stages via immunofluorescence labeling of Piezo1 protein (Figure 42).

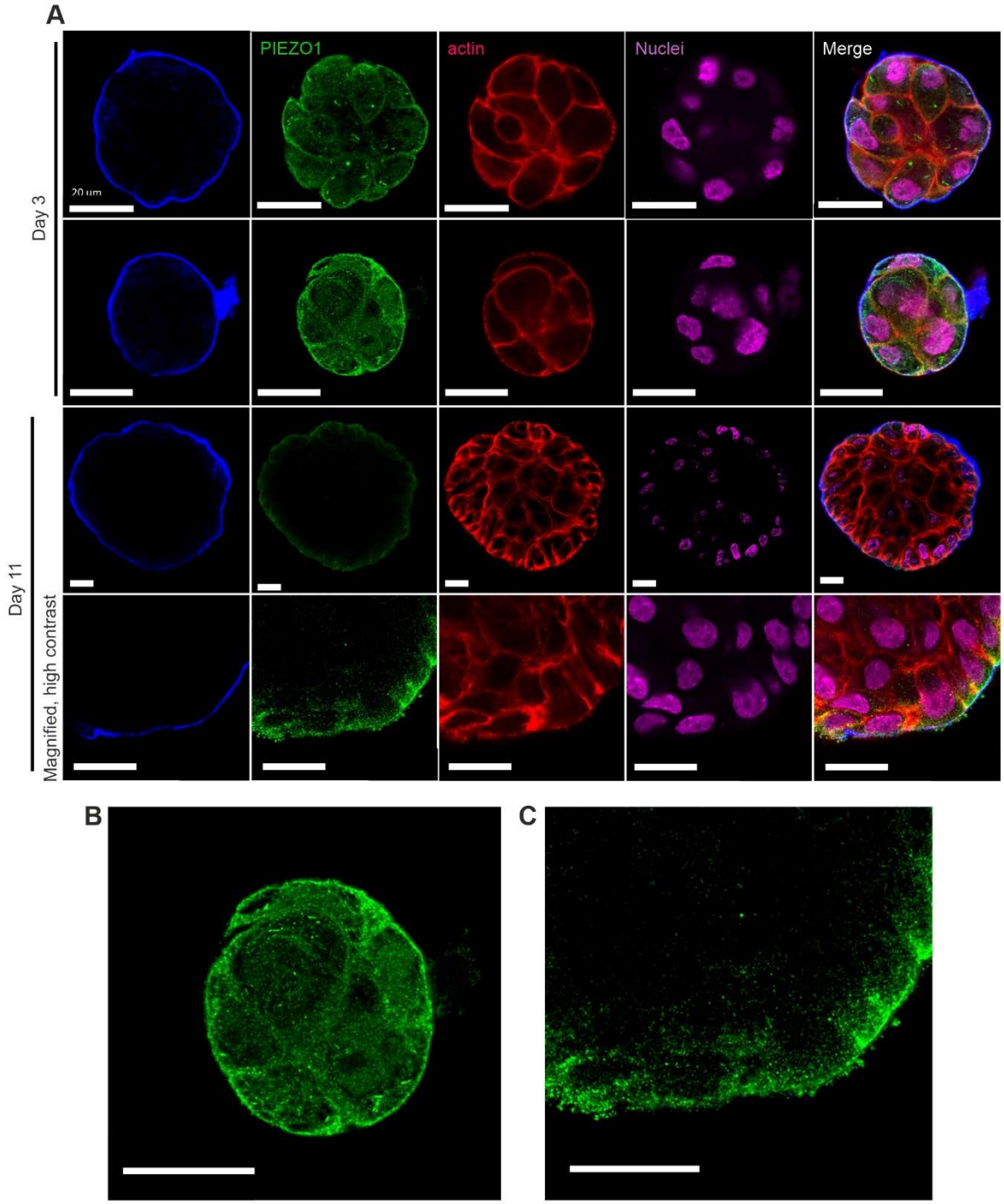

Figure 42: PIEZO1 localization changes during spheroid cultivation. MCF10A LIveAct-RFP spheroids were cultivated for 3 or 11 before transfer onto glass cover slides for fixation and IF-staining of the BM (collagen IV, blue) actin (red), Piezo1 (green) and nuclei (magenta). Cross sections at the equatorial plane demonstrate PIEZO1 (green)in undifferentiated (day 3) and differentiated (day 11) spheroids. (A) Two spheroids cultivated for 3 days display different localization of Piezo1. At day 11 of cultivation, spheroids display a much weaker Piezo1 signal. Magnification in the last row of images shows a magnified are of the spheroid with high contrast. (B) Magnifications of Piezo1 channel of second spheroid at day 3 shown in A. (C) Magnification of Piezo1 channel of spheroid at day 11 shown in A. Scale bars = 20 µm.

The BM and nuclei were simultaneously fluorescently labeled and imaged to confirm the developmental stage of spheroids and the differentiation state of cells. According to the descriptions in 3.1.3, did spheroids display representative cellular organization and cellular morphology as well as BM development for their maturation stage.

Piezo1 signal was overall observed to be weaker in 11-day-old spheroids than in 3-day-old spheroids. After three days of cultivation, spheroids had Piezo1 signal clearly lining the cell-BM interface and often (~50%) also the cell-cell interfaces. Also, an intracellular Piezo1 signal was present in every cell. After 11 days of cultivation, no cellular Piezo1 signal was detected anymore except for the most outer cell layer, which lined the cell-ECM interface in speckles.

To summarize, these results indicate that Piezo1 expression is reduced in increasingly differentiated spheroids. However, these results are preliminary and not final.

3.2 Quantification of spheroid-derived 3D matrix deformations

In order to gain a detailed comprehension on how matrix stiffening affects breast epithelium, it is necessary to identify and measure the forces that mammary epithelial cells generate. A common approach for the investigation of cell-generated forces during adhesion and migration on 2D elastomeric substrates is TFM as described in 1.3.2. Tools to measure traction forces of breast epithelial spheroids in 3D matrices are however still missing.

To perform TFM in 3D matrices, three conditions have to be met. First, the material properties of the matrix need to be well characterized. Second, matrix displacement needs to be measured with high resolution. Third, retrieval of forces from matrix deformations. Working towards a 3D TFM approach, breast epithelial spheroids were embedded into matrices of known mechanical properties together with Prof. Dr.-Ing. Laura De Laporte by M. Sc. Susan Babu from the DWI - Leibniz-Institute for Interactive Materials at the RWTH Aachen. Next, 3D microsphere software was developed together with Dr. Ronald Springer (IBI-2, FZJ) to perform high-resolution measurements of microsphere displacement in 3D.

3.2.1 The effect of PEG-based hydrogels on spheroidal organization

To accurately calculate the force generation of mammary epithelial spheroids based on microsphere displacement, it is crucial to know the deformed matrix's mechanical properties precisely. EHS-derived matrices are an essential material for studies of 3D tissues and are still the only 3D matrix that provides MCF10A cells with the microenvironment that promotes proper spheroidal development and cellular differentiation. However, due to its degradability, it is volatile regarding its mechanical properties. As described in chapter 3.1.5, EHS-gel mechanics change with cultivation time. For this reason, it was necessary to utilize non-degradable, biocompatible hydrogels to serve as the microsphere-laden 3D matrix in which the MCF 10A spheroids were to be embedded. Further, this matrix should be fine-tuneable in terms of stiffness and cell adhesion site composition to allow precise imitation of the natural breast gland ECM and tumor-like conditions, enabling a wide range of possible investigations. A suitable hydrogel was found in the form of Poly (ethylene glycol) (PEG) –gels produced at the DWI - Leibniz-Institute for Interactive Materials at the RWTH Aachen in the laboratory of Prof. Dr.-Ing. Laura De Laporte by M. Sc. Susan Babu [171,208]. These 8-Arm PEG gels polymerize within 20 minutes by the addition of Factor XIII, forming a polymer from precursor molecules that allow for precise manipulation allowing high control over the stiffness, degradability and integrin binding sites composed of peptides (for detail, see appendix).

To conduct comprehensive studies on the force generation of breast epithelial spheroids in PEG-gels, it was necessary to determine whether gel conditions were suited for MCF 10A cultivation. Thereby, whether differentiated spheroids behave normally or display an altered morphology when embedded in PEG-gels. For this purpose, MCF 10A spheroids cultivated for 11 days in EHS gel were transferred into PEG-gels with 45 Pa and 170 Pa stiffness (shear modulus determined via rheometry by Susan Babu) resembling normal breast tissue stiffness and tumor-associated matrix stiffening (for details, see chapter 1.2). In all following experiments, modification of PEG-precursors with specific integrin binding sites was not done to minimize experimental variables. To accommodate missing integrin binding sites, EHS-substrate was added to the PEG-precursor mixture at a non-gelling concentration (6 mg/ml) before the addition of factor XIII.

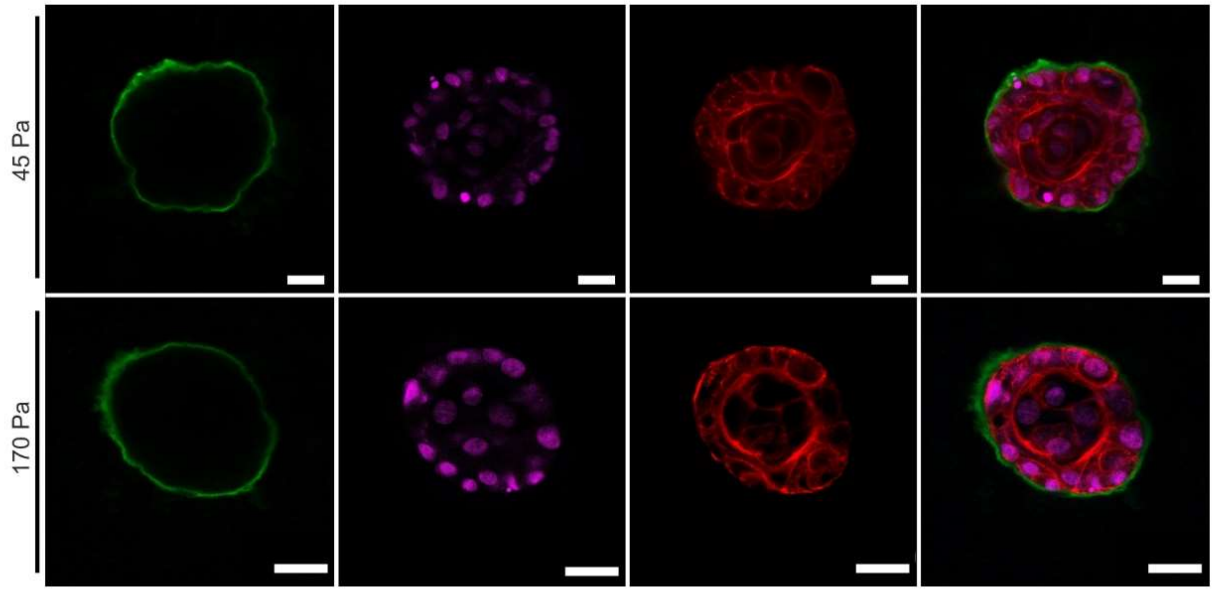

Figure 43: MCF10A spheroid cultivation in PEG-gels. MCF10A LiveAct-RFP spheroids were cultured in EHS-gel for 11 days before being transferred into PEG-gels of either 45 Pa or 170 Pa PEG-gels containing 6 mg/mL EHS-substrate. After three days of cultivation in PEG-gels, samples were fixated and immunocytochemically treated (for details, see chapter 2.12) for labeling of the BM (collagen IV, green), nuclei (violet) and F-actin (red). Micrographs show representative spheroids imaged at their equatorial plane. All scale bars = 20 µm.

Images shown in Figure 43 demonstrate that cultivation for three days in PEG-gels does not drastically alter the developmental process of MCF 10A spheroids. Spheroids even continued with their regular maturation schedule as indicated by beginning lumen clearance which was absent in the spheroids before their transfer into the PEG-gels. As spheroids displayed normal morphology, they could be analyzed regarding their force generation in PEG-gels.

3.2.2 Determining 3D displacement vector fields

Microsphere tracking was chosen for the determination of matrix deformation for this 3D TFM approach. For this purpose, fluorescent microspheres were added to PEG-gel precursor solutions with the same protocol as was used to incorporate microspheres into EHS-substrates (for details, see chapter 2.10.2). For tracking microspheres, a tailored image analysis software based on a normalized cross-correlation pattern matching was created by Dr. Ronald Springer (IBI, FZJ) (for details, see chapter 2.11.2). The software first separated a reference 3D imaging data set of fluorescent microspheres into 3D cuboid templates of definable size. In a second image, the pattern of each template is then searched for at a given range. If a matching pattern was found, a displacement vector was calculated. This results in a matrix of template positional information and average displacement between time points, which can be conveniently displayed in a 3D vector graph (for details, see chapter 2.11.3).

The applicability of this approach was first tested with force-generating Poly-N-isopropylacrylamide (pNIPAM)-microgels embedded into PEG-gels. These pNIPAM-laden PEG-gel samples were produced and provided by Susan Babu (DWI) (for details, see appendix). . pNIPAM-microgels are thermoresponsive and undergo shrink at temperatures above 25 °C [216]. The pNIPAM-gels of approximately 70 µm in diameter were embedded into microsphere-laden PEG-gels (10 Pa Storage modulus; 0.2Ø µm microspheres) (Figure 44 A). To ensure that forces generated during volumetric changes of the pNIPAM-gels are transmitted to the surrounding PEG-gel, covalent binding between pNIPAM and PEG-gel was performed.

These pNIPAM-microsphere-laden PEG-gels were subjected to temperature changes with simultaneous imaging of 3D microsphere position in the PEG-gel surrounding a pNIPAM microgel. The temperature was controlled via the incubation chamber of the microscope and was measured with a thermal diode placed into the PEG-gel covering medium. Readout of the temperature was performed with a thermal diode (connected to a thermal camera) placed into the buffer that covered samples. First, 3D positional information of microspheres in the gel surrounding one pNIPAM-gel was captured at 25.1°C via Z-Stack imaging. Imaging of pNIPAM-gel was facilitated by fluorescent labels incorporated into the gels. The temperature was then increased to 30.8°C before the microspheres were imaged again.

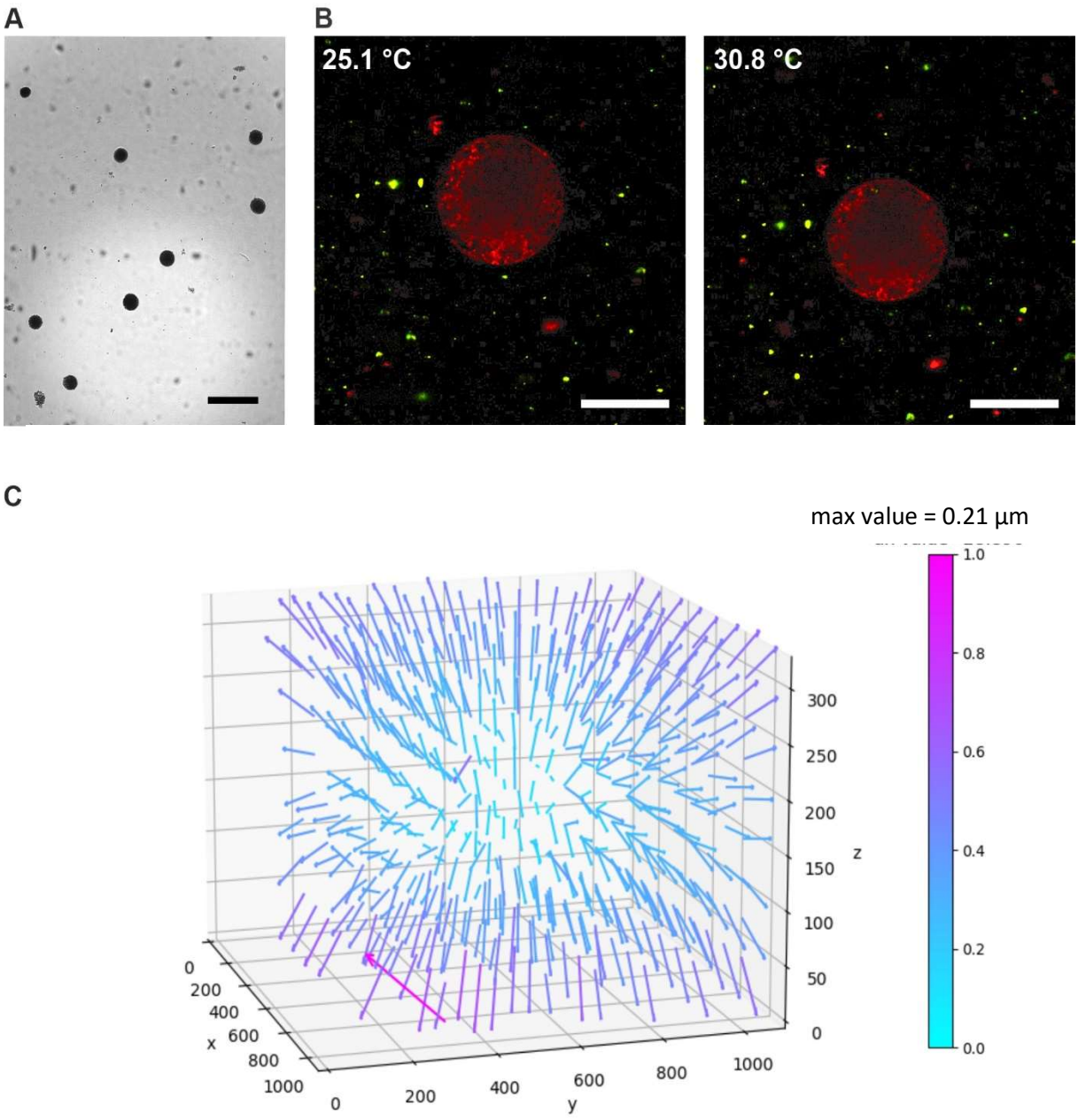

Figure 44: pNIPAM-gel expansion deforms the surrounding PEG-gel. (A) Transmitted light microscopy image of pNIPAM-microgels embedded in PEG-gels (Courtesy of the DWI). Black dots represent pNIPAM-microgels. Grey dots most likely are microsphere aggergates. Scale bar = 250 µm. (B) Micrographs of NIPAM-gel (red) at 25.1°C and 30.8°C embedded into PEG-gel (10 Pa) with incorporated fluorescent microspheres (green). Scale bars = 50 µm. (C) 3D vector graph of calculated microsphere displacement due to pNIPAM shrinkage from 25.1 °C to 30.8 °C . Vectors are inverted as displacement was calculated from the gel at 30.8 °C to 25.1 °C. Image data parameters: Pixelsize (X/Y/Z) 0.18, 0.18, 0.36 µm. Microsphere displacement analysis parameters: Template size (XY): 119 px; Template size (Z) 35 px; Search lenght (X/-X/Y/-Y/Z/-Z):30,30,30,30,15,15 [in px]; Cross-correlation threshold: 0.7; Vector length is color coded for relative length in comparison to the longest displacement (max value in px). Vector Scaling = 1.

Shrinking of the pNIPAM-gel was confirmed by determining the diameter of the microgel at its equatorial plane 25.1 °C (~71 µm) and 30.8 °C (~66 µm)(figure 44 B). These temperature changes caused notable drift of the field of view during image acquisition. This is to expect as thermal drift during microscopy is a common occurrence [217]. While manual readjustment was performed before Z-stack imaging of microspheres after pNIPAM shrinking, it was noticed that both imaging data sets were shifted in all dimensions by up to 50 µm. For analysis, drift correction was performed utilizing the cuboid pattern matching approach for 3D microsphere displacement in all eight corners of the 3D data set (20x20x20 µm cuboid) 100 µm apart from the data sets´ borders. The datasets were then shifted by the average displacement calculated for the eight cuboids. Subsequently, the software described in 2.11.2 was utilized to analyze the microsphere displacements caused by the volumetric change of a PNIPAM-gel. Displacement was calculated from 30.8 °C to 25.1°C.

The resulting 3D vector graph shows that the pNIPAM volumetric change caused a radial symmetric displacement of microspheres that is propagated through the PEG-gel (figure 44 C). Moreover, the displacements are increasing progressively over distance. On closer visual inspection of the vector graph, it appears that the deformation and/or expansion of the whole gel causes additional microsphere displacement. This was indicated by an increase in displacement with distance to the centered pNIPAM gel and a slight offset of opposite vector direction and length on opposite sites of the pNIPAM-gel. This indicated a temperature-dependent volume change of the PEG-gel or a swelling effect due to osmolarity changes of the media as a result of evaporation. Further, microsphere distribution in the PEG-gel was observed to be inhomogeneous. The microspheres aggregated to form larger (~2-5 Ø µm) accumulations. Also, the largest calculated displacement does not fit the neighboring displacement vector direction. This was believed to be an analysis artifact caused by a low density of microspheres resulting in an unspecific template pattern.

To summarize, the calculated displacement vectors intuitively describe the gel deformations, allowing for basic analysis of data sets. Visualization of 3D displacement vectors also allows for the visual identification of analysis artifacts by identification of vectors with large differences in scale or direction, e.g., twice the length or at a 90° angle, compared to displacement vectors of neighboring volumes. Thereby was shown that the displacement vectors accurately describe expected gel deformations around a radially contracting spherical

object. In essence, this result shows that the principle of 3D TFM that was imagined is feasible. While analysis artifacts appeared, was the overall calculated displacement vector field determined precisely and reliably.

3.2.3 MCF10A spheroids deform their surrounding matrix tangential to their surface

As a reliable 3D microsphere tracking approach was successfully established, breast epithelial spheroid-derived deformation of PEG-gels could be determined. Accordingly, it was next tested how MCF 10A spheroids deform their surrounding matrix when embedded into microsphere-laden PEG-gels. In line with previous studies showing with 2D TFM that cells and spheroids placed on planar surfaces generate increased forces with an increase in surface stiffness, it was hypothesized that an increase in 3D matrix stiffness would lead to higher force generation in MCF 10A spheroids.

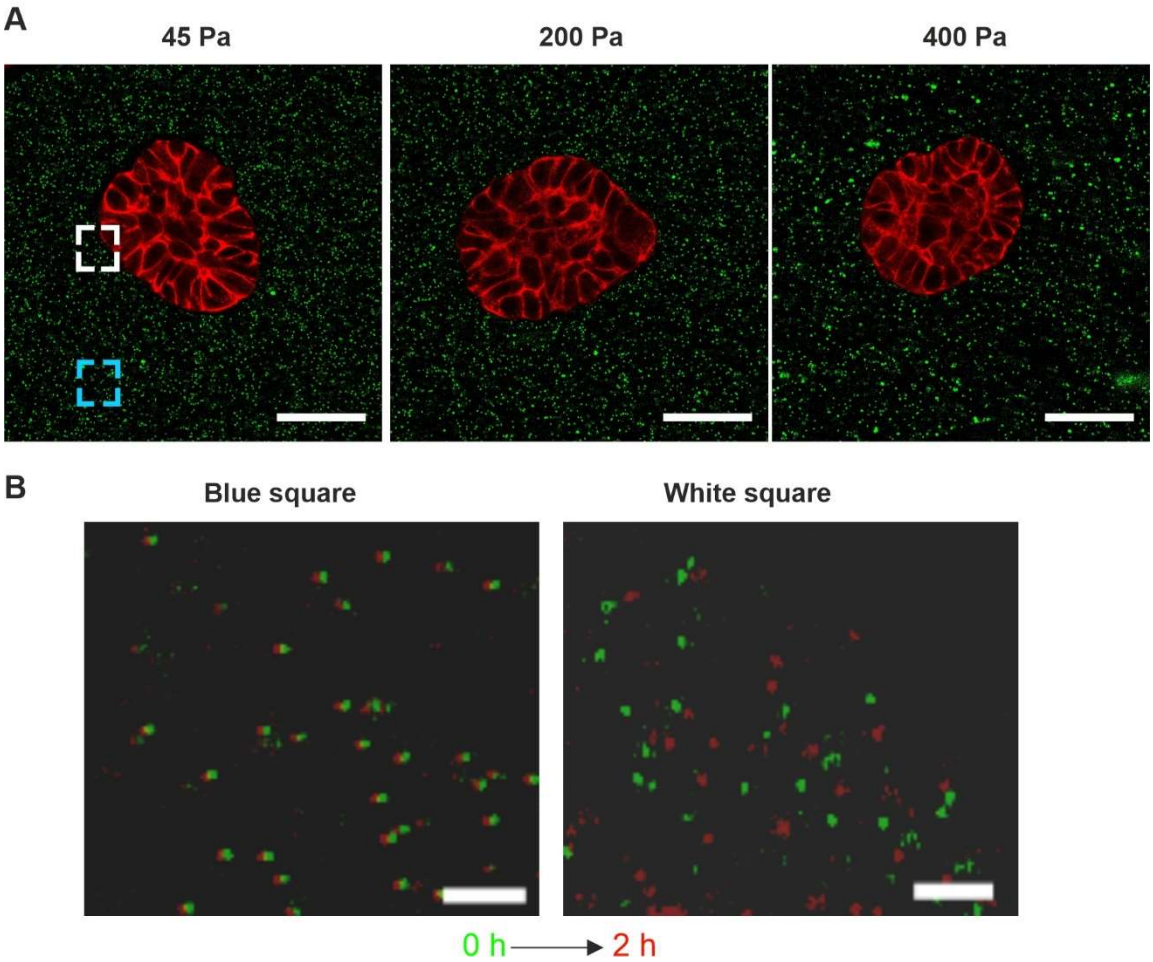

Figure 45: MCF10A spheroids show normal morphology in PEG-gels. MCF10A LiveAct RFP spheroids were cultivated for 11 days in EHS-derived substrates before transfer into PEG-gels of varying stiffness in preparation for microsphere displacement measurements. (A) Micrographs show representative spheroidal organization and morphology (actin, red) at equatorial plane and homogeneous microsphere distribution (green). Scale bars = 50 µm. (B) Magnified images of areas indicated in A. Images of microsphere position at the start of Z-stack imaging (green) and 2 hours later (red) were superimposed. Scale bars = 5 µm

MCF10A LiveAct-RFP spheroids were transferred into PEG-gels of either 45 Pa, 200 Pa or 400 Pa stiffness at day 11 of cultivation to test this hypothesis (for details, see chapter 2.11.1). For better dispersion of fluorescent microspheres, the precursor microsphere mixture was also treated for 30 minutes in an ultra-sonic bath in ice-cold water.

For each of the three PEG-gels, two spheroids were chosen to be analyzed. Additionally, one spheroid-free position was also analyzed as a control. This was done to account for non-spheroid-derived gel deformations, as was indicated to occur during pNIPAM-gel analysis. For each of these nine dedicated spheroid and spheroid free gel positions, a 3D image stack of the microspheres was acquired every 2 hours for a total of 12 hours. Imaging started ~30 minutes after embedding of spheroids into PEG-gels.

Visual analysis of spheroids at the equatorial plane revealed normal spheroidal organization and cellular morphology (Figure 45 A). Also, the distribution of microspheres improved to previous experiments. The microspheres were homogeneously spread out and scattered in all three gels, only rarely aggregating in the 400 Pa gel.

Visual analysis of microsphere displacement of the raw imaging data revealed a lateral drift of <1 µm within 2 hours of imaging. This observation was also made for spheroid-free positions (Figure 45 B). Displacement of microspheres of up to ~3 µm in the immediate vicinity of the spheroid, confirming MCF10A spheroids subject their surrounding matrix to significant forces (Figure 45 B).

Microsphere displacements were determined with the software described in chapter 3.2.2, after correcting for drift with the same software. The resulting displacement vectors were displayed in a 3D graph with their origin at the center of the template defined at the reference Z-Stack (for details, see chapter 2.11.3). Vector graphs of spheroid-free controls revealed that gel deformations are present even in the absence of direct cell forces.

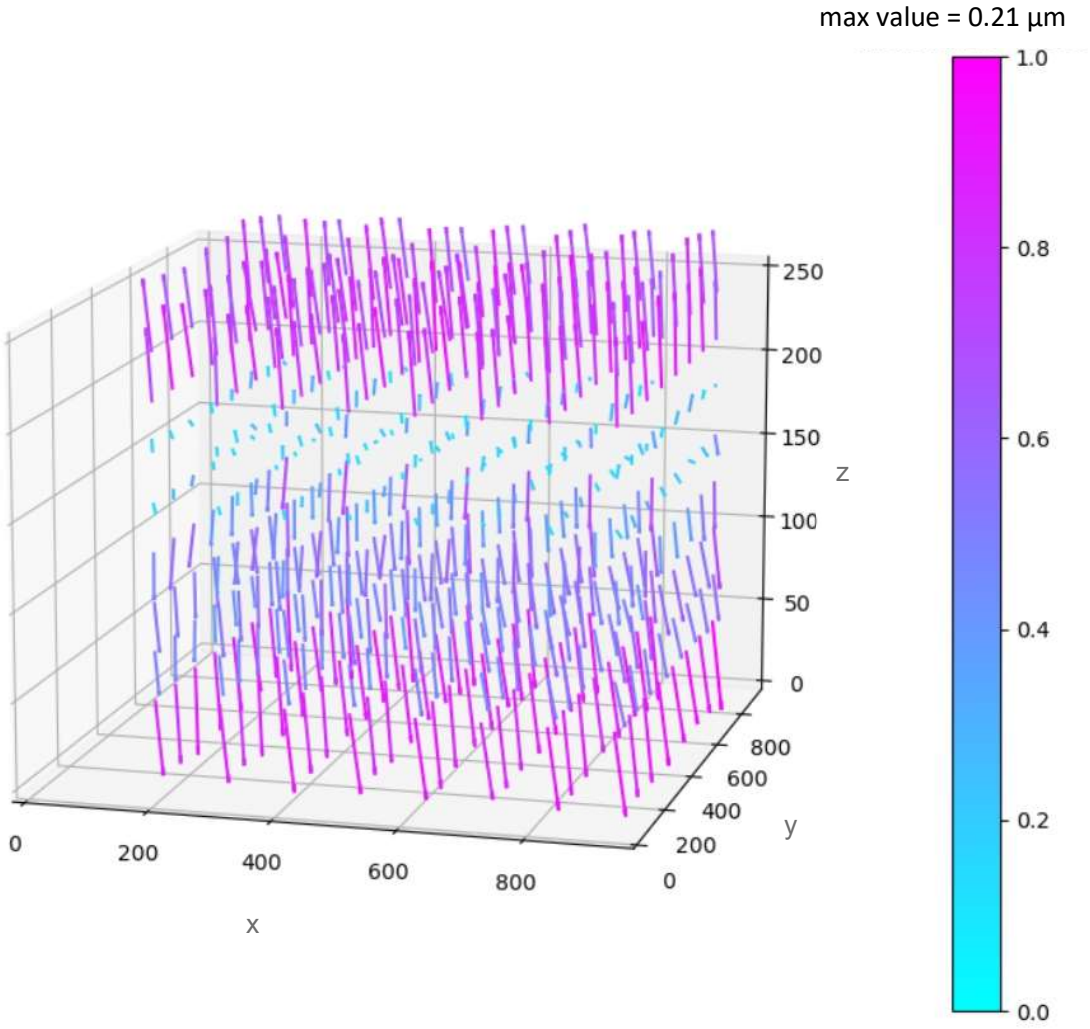

Figure 46: 3D displacement vectors reveal PEG-gel deformation independent of spheroid presence. 3D vector graph of displacement vectors calculated for microspheres in a PEG-gel (400 Pa) in absence of a force generating spheroid after 12 hours. Axis dimensions in pixel. Image data parameters: Pixel size (X/Y/Z) 0.2, 0.2, 0.29 µm. Microsphere displacement analysis parameters: Template size (XY): 100 px; Template size (Z) 70 px; Search length (X/-X/Y/-Y/Z/-Z):100,100,100,100,70,70 [in px]; Cross-correlation threshold: 0.7. Vector scaling = 4. Vector length is color coded for relative length in comparison to the longest displacement (max value in px).

All displacement vectors pointed towards a central plane at ~150 px height (Figure 46) and appeared to increase in length over time. This observation was made for all nine positions analyzed across the three PEG-gels. Since all displacement vectors had the same orientation, this was unlikely to be caused by an experimental uncertainty but was rather the result of a deterministic process.

To analyze the magnitude of this effect, the lengths of all displacement vectors were summed up for each time point to estimate the total matrix deformation (for details, see chapter 2.11.3). This was done for comparison of total deformation in the PEG-gel surrounding a spheroid or within a cell-free volume (Figure 47). For both conditions, the total gel deformation increased every 2 hours. The average increase in summed-up displacement vector lengths every 2 hours was 36.4% in cell-free gel volumes and 31.8%. Thereby was revealed that spheroid-independent gel deformations are substantial and increase at similar rates at cell-free positions and in the vicinity of spheroids. This effect was credited to shrinkage of the PEG-gels as indicated by the direction of calculated displacement vectors in cell-free positions.

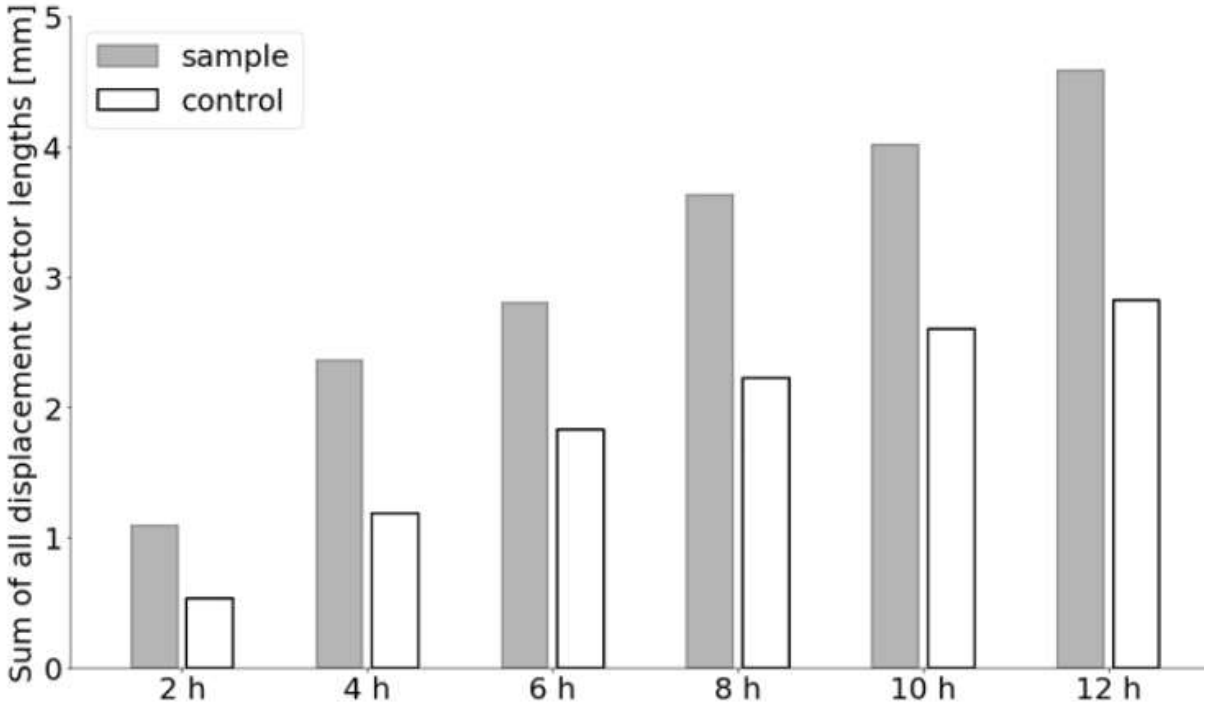

Figure 47: Non spheroid derived gel deformations are substantial. Bar chart depicting summed up vector length of microsphere displacement in a PEG-gel (400 Pa) at one position with (sample) and one position without a spheroid (control). Displacement vectors were calculated with the first image stack as a reference. Image data parameters: Pixel size (X/Y/Z) 0.2, 0.2, 0.29 µm. Microsphere displacement analysis parameters: Template size (XY): 50 px; Template size (Z) 35 px; Search length (X/-X/Y/-Y/Z/-Z):50,50,50,50,17,17 [in px]; Cross-correlation threshold: 0.7.

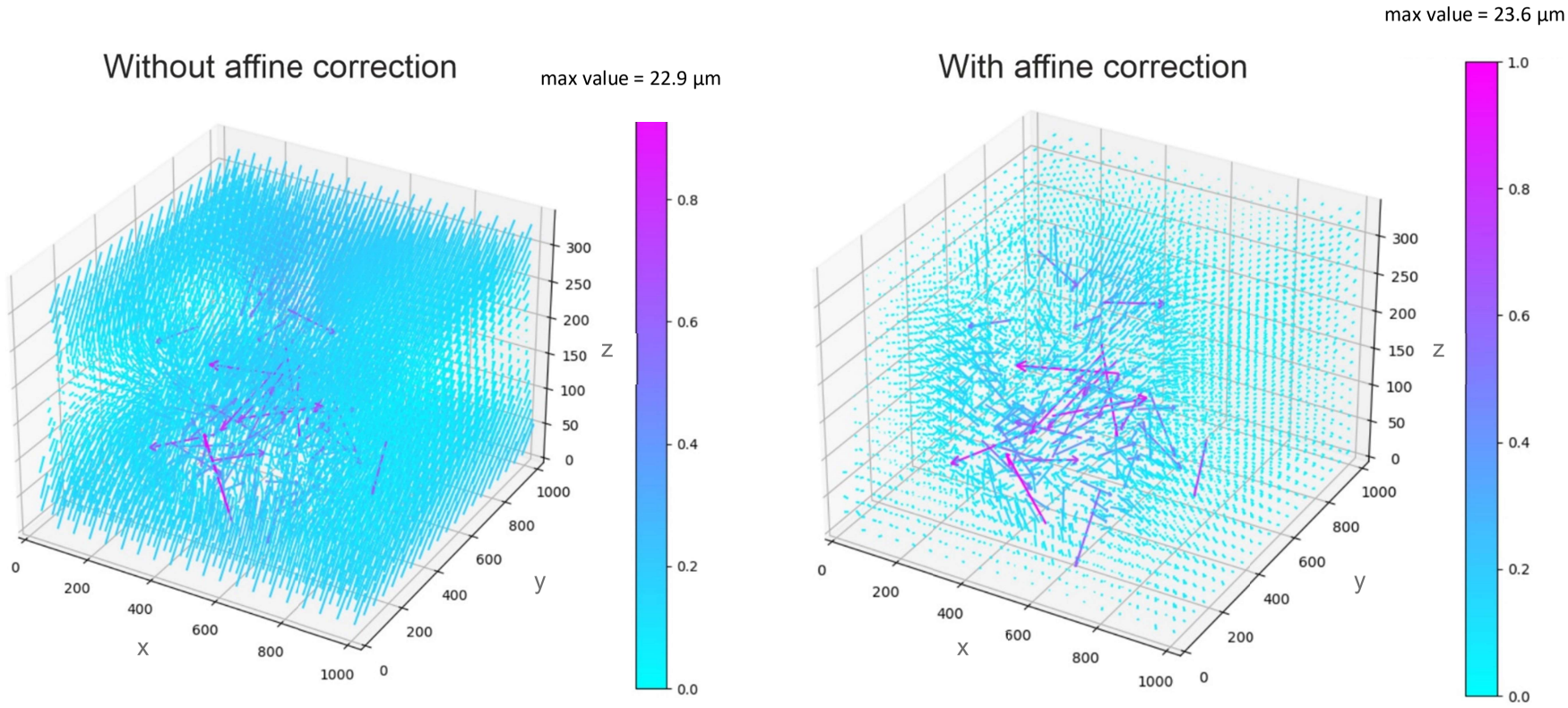

Figure 48: Affine correction of 3D microsphere data sets removes spheroid independent deformation component. Microsphere displacement in a PEG-gel (400 Pa) was determined near an embedded spheroid between the first acquired Z-Stack (0 h) and the last acquired Z-Stack (12 h). 3D vector graphs were generated from data with and without affine transformation of displacement vectors. Image data parameters: Pixel size (X/Y/Z) 0.2, 0.2, 0.29 µm. Microsphere displacement analysis parameters: Template size (XY): 50 px; Template size (Z) 35 px; Search length (X/-X/Y/-Y/Z/-Z):100,100,100,100,70,70 [in px]; Cross-correlation threshold: 0.7. Vector length is color coded for relative length in comparison to the longest displacement (max value in px) Vector scaling =6.

Such deformations distort a precise analysis of cellular force-driven gel deformation. Affine correction of the 3D displacement vector field was therefore performed by Dr. Ronald Springer to correct for non-spheroid-derived gel deformations (for details, see appendix). Here, rotation, torsion, translation and dilation of the whole displacement vector field are determined by the least square fit. The individual displacement vectors are then corrected for the overall deformation of the vector field in x, y and z.

Affine transformation almost completely separated the non-spheroid-derived deformation component from spheroid-derived deformations, as confirmed by visual analysis of 3D vector graphs (figure 48). After affine transformation, the spheroid's location in the center of the graph could be determined visually by the presence of relatively large deformation. Thus, affine transformation removed non-spheroid-derived deformations from the data.

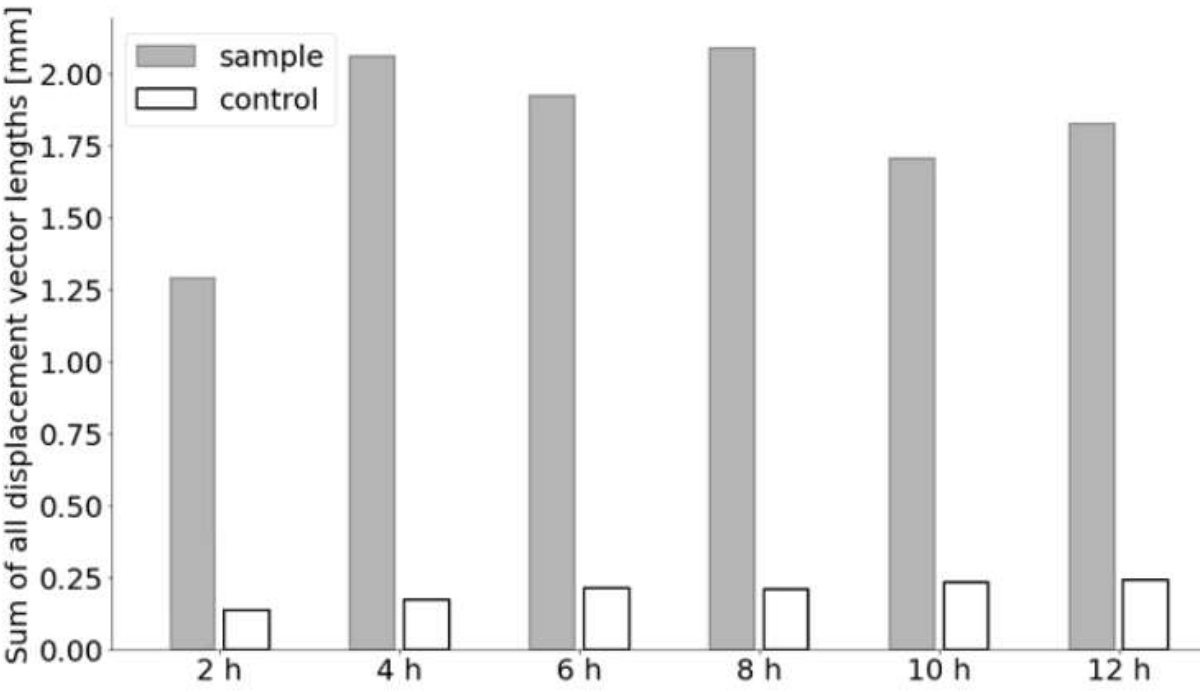

Figure 49: Affine transformation removes non spheroid derived gel deformations. Bar chart depicting summend up vector lengths of microsphere displacement determined in a PEG-gel (400 Pa) at one position with (sample) and one position without a spheroid (control) after affine correction. Displacement vectors were calculated with the first image stack as a reference. Image data parameters: Pixel size (X/Y/Z) 0.2, 0.2, 0.29 µm. Microsphere displacement analysis parameters: Template size (XY): 50 px; Template size (Z) 17 px; Search length (X/-X/Y/-Y/Z/-Z):50,50,50,50,17,17 [in px]; Cross-correlation threshold: 0.7.

Repeating analysis of total deformation by summing all displacement vector lengths supported these observations as deformation in cell-free PEG-gels was reduced drastically (figure 49). Sum of all vector lengths in cell-free 400 Pa gel after 12 h was 2.824 mm before affine transformation and 0.329 mm after affine transformation (2.495 mm difference, reduction to 8.4%). The corresponding value in PEG-gel surrounding a spheroid was reduced from 4,585 mm to 1.386 mm (3.199 mm difference). Total vector displacement vector lengths for cell-free positions ranged between 0.135 mm and 0.239 mm (mean: 0.238 mm) and were therefore clearly lower compared to the deformations in the vicinity of a spheroid with deformations from 1.013 mm to 1.386 mm (mean: 1.396). Interestingly, it was found that gel deformation only increased noticeably between 2 and 4 hours of the measurement (an increase of 0.636 mm). In the following hours the deformation changes in between time points were lower and even decreased (-0.27 mm at 4 to 6 h, +0.198 mm at 6 to 8 h, -0.274 mm at 8 to 10 h, +0.06 mm at 10 to 12h). Therefore, the deformation amplitude remained similar across time points after the first two hours of the measurement.

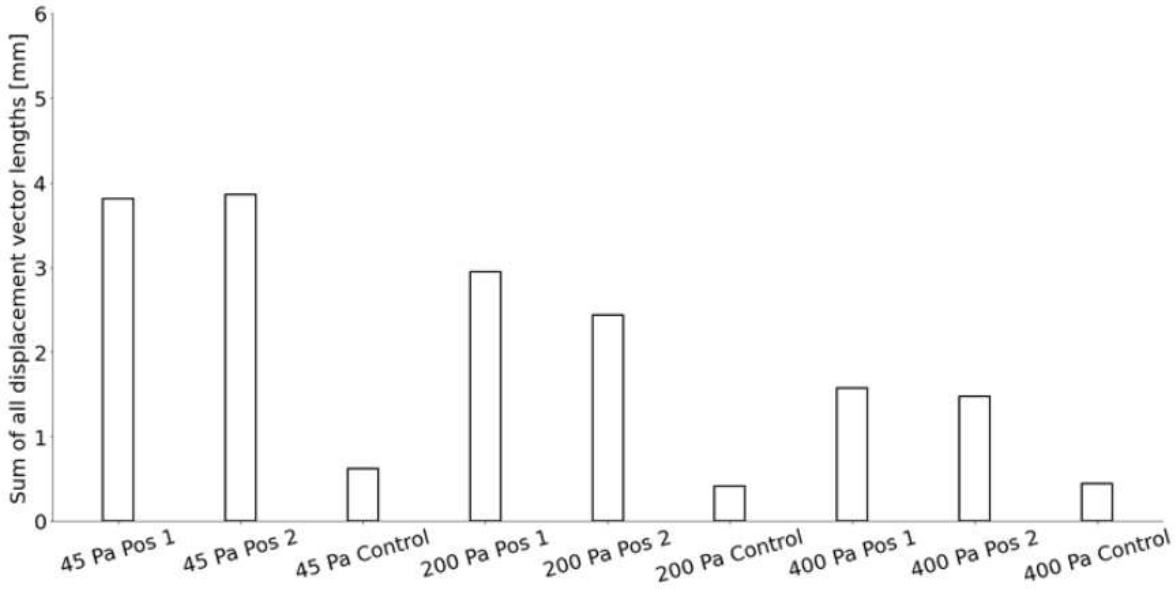

Figure 50: Spheroid-derived gel deformation depends on substrate stiffness. Displacement vectors for microsphere displacement in PEG-gels of varying stiffness (45 Pa, 200 Pa, 400 Pa) were determined either near an embedded spheroid (Pos 1, Pos 2) or at a spheroid free position of the same gel between the first (0 h) and last (12h) acquired Z-Stack. Affine correction was performed after displacement vector calculation. Bar height represents summed up vector lengths for each individual analyzed volume. Image data parameters: Pixel size (X/Y/Z) 0.2, 0.2, 0.29 µm. Microsphere displacement analysis parameters: Template size (XY): 50 px; Template size (Z) 35 px; Search length (X/-X/Y/-Y/Z/-Z):100,100,100,100,70,70 [in px]; Cross-correlation threshold: 0.7.

Comparison of deformation amplitudes in PEG-gels at all observed positions for all 3 gels revealed a dependency on gel stiffness (figure 50).

It was observed that the amplitude of deformation in PEG-gels surrounding a spheroid increases in gels of lower stiffness. In detail, the average sum of displacement vector lengths for both measured spheroids was 3.82 mm in the 45 Pa gel, 2.51 mm in a 200 Pa gel and 1.54 mm in the 400 Pa gel. Notably, are spheroid force-dependent deformations clearly discernible from deformations calculated for spheroid-free gel volume of the same dimensions with a 6 (45 Pa; cell-free: 0.617 mm; Pos1:3.805 mm) to 3-fold (400 Pa; cell-free: 0.446; Pos 1: 1.557) decrease in deformation amplitude. The amplitude of deformation determined for spheroid-free gel volumes was found to be similar after affine correction (45 Pa: 0.617 mm; 200 Pa: 0.413 mm; 400 Pa: 0.446 mm).

Visual inspection of 3D vector graphs after affine correction revealed that the largest deformations occur at the center of the observed gel volume, the position of the spheroid. However, large displacement vectors stood out as they were significantly longer (~10 fold) larger than neighboring displacement vectors and diverged from their general orientation (figure 48). As analysis artifacts, they were removed via interquartile range outlier detection ($>Q_3 + 5 \times IQR$) (for detail, see chapter 2.11.3).

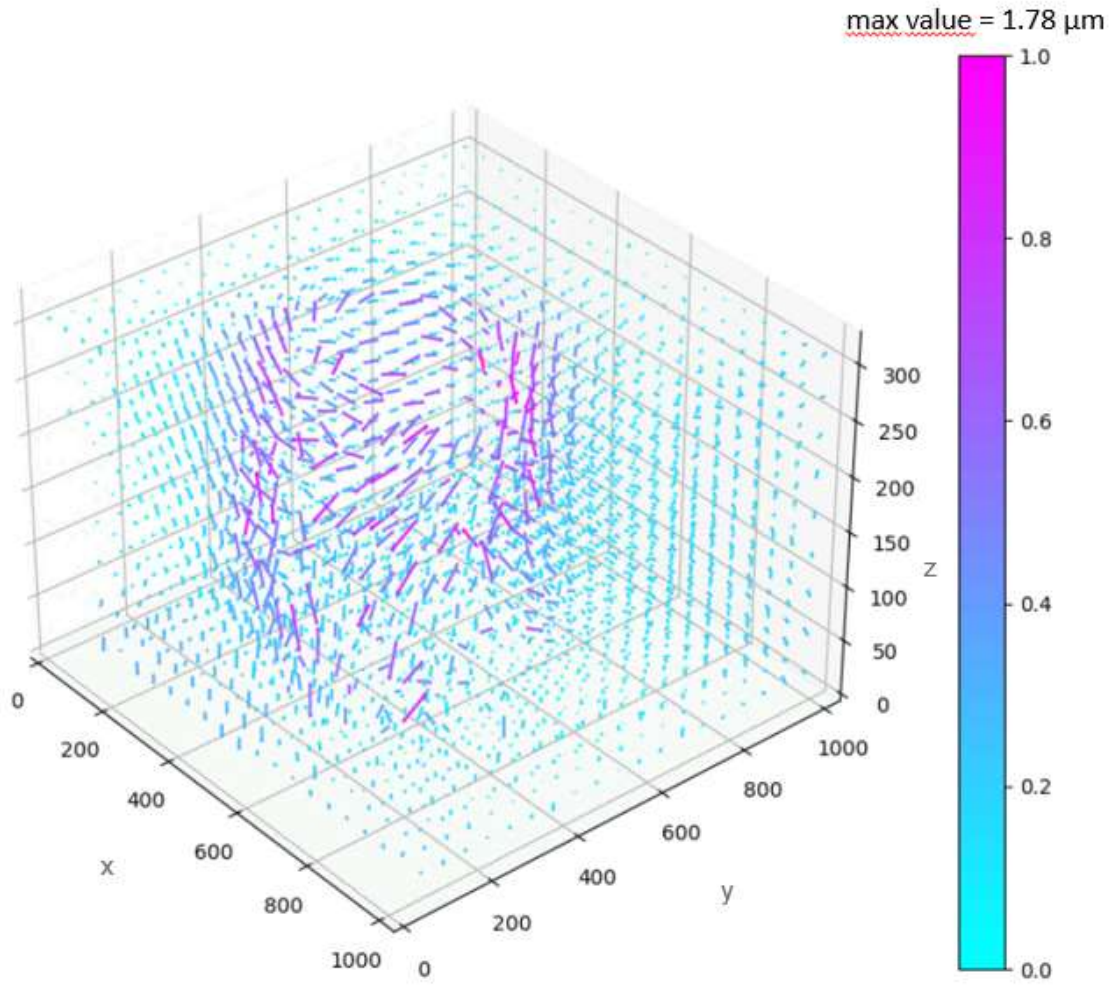

Figure 51: Spheroid-derived deformations in 3D PEG-gels. Microsphere displacement in a PEG-gel (400 Pa) was determined near an embedded spheroid between the first acquired Z-Stack (0h) and the last acquired Z-stack (12h). 3D vector graphs were generated from data after application of affine correction of displacement vectors and outlier detection. Image data parameters: Pixel size (X/Y/Z) 0.2, 0.2, 0.29 µm. Microsphere displacement analysis parameters: Template size (XY): 50 px; Template size (Z) 35 px; Search length (X/-X/Y/-Y/Z/-Z):100,100,100,100,70,70 [in px]; Cross-correlation threshold: 0.7. Vector length is color coded relative to longest displacement (max value in px).

After outlier removal, the spheroid-derived gel deformations could be represented accurately in 3D vector graphs by color-coded vector lengths (Figure 51). This was the result of a drastic decrease in the maximum vector length used as a reference for color coding (23 µm to 1.78 µm). Thus, outlier detection achieved the goal of removing large artificial displacement vectors, most likely resulting from false positive displacement detection. The absence of displacement vectors in the center of the graph clearly showed the position of the spheroid. It was observed that displacement vectors and, thereby, gel deformation are largest in direct contact with the spheroid's surface. Deformations were observed to occur mostly tangential to the surface of the spheroid, indicated that that the spheroid performed a rotational

movement. Also, deformations decreased drastically within ~30 µm distance of the spheroid's surface. Therefore, spheroid-derived deformation did not appear to be propagated over long distances and was overall well captured within the acquired volume.

To summarize, the here described approach for the determination of microsphere displacement in 3D matrices successfully captured breast spheroid-derived deformations in PEG-gels. The displacement vector data was further subjected to affine transformation and outlier removal to filter non-spheroid-derived gel deformations and artifacts. The resulting data revealed a stiffness-dependent change in gel deformation and showed that MCF10A spheroid-derived forces result in mostly tangential matrix deformation at the spheroid's surface.

4 Discussion

The breast gland is a mechanically active tissue that undergoes drastic morphological reorganization even in adulthood [16,114]. The role of hormonal cues during breast tissue development, homeostasis and reorganization are well studied [114,119,218]. However, how exactly mechanical cues such as ECM-stiffness and force exerted by the ECM on the mammary epithelium are involved remains poorly understood. To shed light on mammary epithelial mechanobiological regulations, cell spheroids are often employed as physiological models [163,168,219]. These models rely on normal, non-transformed cell lines, which undergo a progressive development in natural EHS-derived matrices imitating normal breast tissue adhesion sites and stiffness. The resulting spheroids depict many mammary epithelial *in vivo* features such as a hollow lumen, formation of a BM and basoapically polarized cells [70,155,220]. These state-of-the-art models are especially valued for investigations on breast epithelium in close relation to clinical applications such as malignant transformation [33,219]. Investigations on mechanobiological regulations of cells benefit from the analysis of cellular responses to external stress application and force generation in response to substrate modification. Utilizing such approaches in combination with physiological breast spheroids is currently impeded by a lack of tools.

This work aimed to study the impact of ECM-transmitted shear strain on the breast gland and investigation of cell-forces exerted on the ECM. This was done by developing and utilizing a novel shear stress device for the application of physiological stresses to mammary epithelial spheroids and a confocal microscopy-based approach to determine cell-force derived deformations in 3D matrices of defined mechanical properties.

Characterization of a novel solid shear stress device for straining of EHS-gels

A significant challenge of this work was to develop and characterize a novel device for applying solid shear stresses to hydrogels to imitate natural breast gland deformation *in vitro*. As it was intended to utilize the device for shear stress application to physiological breast epithelial spheroids, it was necessary to apply strains to EHS-substrate derived hydrogels as they allow for the cultivation of physiologically relevant MCF10A spheroids.

The device was designed to allow contactless stress application parallel to the surface of natural EHS substrates via magnetic coupling by moving a magnetic sled. Contactless stress application was beneficial as it allowed for the sterile sealing of samples and simplified

handling. Moreover, previously developed approaches for the application of shear stress to hydrogels using direct contact for force transmission resulted in hydrogel damage due to increased torque. Thus, this force application mode was crucial for hydrogels' stability during cyclic application of shear stress. As by design, the device allowed for simultaneous image acquisition with an inverse confocal microscope. The lateral displacement of gel-embedded fluorescent microspheres in relation to gel height could therefore be imaged to determine gel deformations, confirming the device produces solid shear strain directly dependent on sled displacement. An image analysis-based computational approach was developed with Dr. Ronald Springer for further characterization of the applied strain. Utilizing this approach allowed for the determination of strain amplitude which was found to be linear and homogeneous to a degree expectable for biological samples. Straining and analyzing softer, diluted EHS gels revealed that this approach is sensitive to changes in stiffness in super soft hydrogels (<60 Pa). Finally, the device was shown to allow for the subjection of physiological breast epithelial models to natural breast gland deformations *in vitro*. Thereby was the principle of stress application and detection of strain proven to be suitable for the reliable analyses of the impact of natural breast gland deformations, i.e., ECM shear strain, on breast gland morphogenesis. While other approaches for the application of stresses to cells in 3D matrices exist, no presently available tools enabled such investigations due to dependency on incompatible hydrogels or different strain modes [221–223].

In essence, the constructed device fulfilled all initially desired functions and produced strains in hydrogels conforming to the theorized stress application. Moreover, the device allowed for prolonged cyclic straining (22 h) of sterile samples with high reproducibility and simultaneous live cell imaging.

Strain measurements revealed structural inhomogeneity in EHS hydrogels

For determination of strain in hydrogels, the displacement of gel-embedded microspheres was determined via image analysis software. The cross-correlation-based pattern-matching software developed with Dr. Ronald Springer produced reliable results that were used for linear regression analysis. This approach allowed for quantitative analysis of local strain in hydrogels upon stress application. It was thereby possible to investigate strain homogeneity within individual hydrogel samples and across replicates.

Quantification of strain revealed interesting characteristics of EHS-hydrogels. The shear strain was directly dependent on substrate stiffness at equal sled displacement. In detail, the strain amplitude increased by 92% for a decrease in substrate stiffness to 50.1% at equal sled displacement. Therefore, analysis of strain amplitude allowed for the identification of stiffness alterations. This also indicates that the amplitude of applied stress was nearly identical, as strain is inverse proportional to substrate stiffness according to Hooke's law.

Strain amplitude variations within a sample were detected. Most likely, were these caused by local stiffness inhomogeneities of EHS-substrates. The elastic modulus of thin films of EHS-gel was found to range from 650 Pa to 1-2 kPa locally as measured by interferometry [224]. Of note, these values are dramatically higher compared to other studies determining the young´s modulus of EHS-substrates to be 170 Pa via indentation or the shear modulus of 55 Pa determined for this work [4](for details, see chapter 3.1.2). This difference is likely the result of a different measuring technique. Still, this study clearly shows that EHS-gel is a heterogeneous material. Thereby, locally stiffer areas are strained less, while average bulk stiffness remained similar across samples, resulting in non-significant differences in average strain amplitudes across samples (for details, see chapter 3.1.2). Of note, stiffness inhomogeneity is a natural characteristic of breast gland tissue [225]. These findings underlined the physiological relevance of EHS hydrogels as a surrogate matrix that resembles the stiffness range of healthy breast tissue since stiffness range has been shown to be a substantial trigger for breast morphogenesis *in vitro* [155].

It was also noticed that the average strain in hydrogels with embedded spheroids, cultivated for three days, changed at 5 mm sled displacement between chapter 3.1.5 (11.9%), chapter 3.1.8 (8.2%) and chapter 3.1.9 (11.5%). The shear stress application experiments described in these chapters were performed with three distinct EHS-substrate lots (meaning production batch). Thereby, the inconsistency of strain amplitudes is simply explained by lot-to-lot variations in protein concentration and composition common for EHS-substrate products [226]. For the EHS-substrate used in this work the protein concentrations varied from 16 mg/mL (LOT: 2248602, chapter 3.1.5) over 17.5 mg/mL (LOT:2327547, chapter 3.1.8) to 17.5 mg/mL (LOT: 2327543, chapter 3.1.9). Changing strain amplitudes were therefore attributed to alterations in mechanical properties of EHS-gel due to protein composition and concentration. This was well in line with the literature measuring Young´s moduli of three individual lots of the EHS-substrate Matrigel to range from 420 ± 290 Pa to 480 ±240 Pa by AFM indentation[227].

The possibility to recognize stiffness differences between different EHS substrates adds valuable information as a specific matrix stiffness is crucial for normal MCF10A spheroidal development [228]. Also, progressive gel deformations were observed to occur during prolonged or cyclic stress application to EHS-substrates (for details, see chapter 3.1.7 and 3.1.1). This was attributed to gel creep which was shown in previous studies to occur in EHS-substrates [209,229]. Linearity of strain in EHS-gels as described in chapter 3.1.3 however shows that gel creep does not affect the analysis. Moreover, strain linearity was maintained in spheroid-laden hydrogels which were produced from two individual layers of EHS-substrates. Thus, the two gel layers were seamlessly connected.

In essence, the developed computational approach to strain measurements is very precise and reliable as it enables the determination of strain changes. Thereby was shown that stress application by sled displacement produces linear shear strain in hydrogels in dependency of EHS-gel stiffness. Strains were shown to be reproducible, albeit variations in amplitude might occur depending on the mechanical properties of the substrate. Finally, gel creep or plane slipping effects did not interfere with strain analysis.

Mechanical resistance of breast epithelial spheroids

After the shear stress-derived strain in EHS hydrogel was successfully characterized, the next step was to determine whether the strain was transmitted to gel-embedded breast spheroids. Strain in spheroids and their surrounding hydrogel after 11 days of cultivation was successfully determined via image analysis-based displacement tracking over multiple focal planes (for details, see chapter 3.1.3). The results confirmed that spheroids are indeed strained (mean: 7.5%), albeit with a lower amplitude than their surrounding gel (mean: 15.3%). Further analysis revealed that the strain amplitudes decreased in spheroids cultivated for 11 days or longer compared to those cultivated for three days. This result implicated a gain of mechanical resistance for spheroids with gradual maturation.

As described in chapter 1.2.2 undergo MCF10A cells a progressive spheroidal development which results in drastic morphological and structural changes between day 3, day 11, and 18 of cultivation. One major aspect of this development is the formation of a BM, which starts on day 1 of cultivation [70]. The colleagues Fabris et al. analyzed the BM's mechanical properties by AFM measurement of decellularized BM shells [72]. Thereby was revealed that the basement

membrane thickens and stiffens, thereby increasing its mechanical strength throughout spheroidal development. Accordingly, it was concluded that the BM of MCF10A spheroids acts as a mechanical stabilizer of the epithelium, a generally accepted function for the BM *in vivo* [230–234]. Notably, the present work demonstrated, for the first time, that this mechanical stability of the BM shields the breast epithelium lining from ECM-transmitted mechanical stress.

As the MCF10A is valued as a physiological model for the breast gland epithelium, these results should also be discussed regarding the BM development of mammary epithelium *in vivo*. During glandular branching morphogenesis, the BM is thin (~104 nm) at the tips of terminal end buds (TEBs) and partially proteolytically depolymerized by the epithelial cells, which facilitates collective migration into the adjacent tissue [115]. Opposite of growth direction, the glandular cells adopt a ductal differentiation and form a thick-developed BM (~1.4 µm) [118,121,235]. Thus, BM development and cellular differentiation is synchronized *in vivo* and in the MCF10A spheroid model. The thin, porous and destabilized BM at the tip of the growing epithelium *in vivo* could therefore reflect the low-developed BM scaffold of undifferentiated 3 to 4-day-young MCF10A spheroids with low shear strain resistance. This correlation supports the notion that the MCF10A spheroid model is well-suited for the investigation of mammary epithelium development.

Besides the development of mechanical resistance, an additional effect was found that appeared with the prolonged interaction of spheroids with their surrounding matrix. Strain measurements of spheroid-bearing EHS-gels cultivated for 4, 11 or 18 days revealed strain increases that were significant in the first 11 days of cultivation. As already discussed, the shear stress device acts as a simple rheometer that allows determining even subtle changes of hydrogel stiffness. The observed gel softening can be explained by ongoing matrix remodeling of the developing spheroids. Taken together, it could be assumed that spheroids undergo a differentiation protocol similar to that of epithelial cells during branching morphogenesis and extensively remodel their ECM proteolytically during the early stages of development. In line with this, other groups and we have demonstrated that MCF10A spheroids produce and secrete MMPs under comparable normal ECM conditions [34,236]. Such remodeling activities could even be a driving factor that allows MCF10A cells to modify their mechanical niche. Moreover, it was shown that increased activity of MMP-9 leads to loss of polarized breast spheroid architecture [237].

Less pronounced gel softening was also found in cell-free gels, which cannot be explained by cellular ECM remodeling. However, the presence of functional MMP-2, MMP-7, and MMP-9 enzymes in EHS-gels has been reported [238,239]. The gel softening of cell-free EHS-gels could hence be the result of residual MMP activity within the EHS substrate. In this line of argumentation, the softening was further accelerated by spheroid-secreted MMPs. However, such an MMP-driven successive gel softening has to be proven experimentally, for instance, by shear straining gels treated with pharmacological broadband MMP inhibitor marimastat [240].

These findings clearly demonstrated the high sensitivity of the device in terms of determining stiffness changes in ultrasoft collagen IV- and laminin-rich hydrogels. This feature might be meaningful for future investigations on cellular matrix remodeling.

ECM-transmitted shear stress triggered apoptotic cell extrusion during early breast gland morphogenesis MCF10A spheroids

Undifferentiated MCF10A spheroids lacking basoapical polarization and covered by a thin BM were observed to extrude cells that appeared to undergo apoptosis in response to cyclic stress application, as was indicated by round morphology and fading F-actin signal. The presence of cleaved Caspase-3 (cC-3) signal within stressed spheroids and in the adjacent matrix confirmed apoptotic events. Quantitative analysis confirmed that cleaved Caspase-3 protein signal occurrence increased upon cyclic EHS-gel straining of 8.2% at 0.2 Hz for 22h (table 9).

In vivo, the breast gland is subjected to shear strain which was measured at its peak to be ~50% during exercise by Haake and Scurr [15]. In this study, strain values were highly dependent on breast support, walking speed and breast size. For example, breast strain was reduced to 1% by the support of a sports bra for a participant with breast size 32A. Therefore, it can be assumed that any range between 1% and 50% shear strain is within a physiological range. Thus, the 8.2% shear strain that caused the described mechanoresponse is well in line with the naturally occurring strain. Considering the breast move up and down during walking, as was reported by Haake and Scurr, cyclic stress application with the shear stress device (-5 mm to +5 mm) corresponds to normal breast deformations. The average walking cycle can be assumed to be ~1 Hz [241]. Therefore, the frequency of 0.2 Hz used to stress spheroids was lower. However, previous studies have shown fibroblasts cultivated on 2D substrates to exhibit mechanoresponsive behavior at cyclic stretch rates of 14% at a frequency of 0.3 Hz [242].

Fibroblasts are commonly found in the skin and would therefore be subjected to similar frequencies of mechanical stress during walking as the breast gland. Thus, are the mechanical loads applied to spheroids with the shear stress device well in line with physiological stresses occurring in the breast gland at frequencies that have been reported to trigger cellular mechanoresponses. Further, both the frequency and amplitude of strain can be increased for future investigations by employing a faster motor (meaning not limited to 4 mm/s due to overheating) to increase the frequency and increase the magnets' strength respectively.

An increase in apoptotic cell extrusion in response to cyclic shear stress was only evident in undifferentiated spheroids cultivated for 3 to 4 days but not in differentiated spheroids cultivated for 10 to 11 days with progressed basoapical polarization and a developed BM.

Stressed differentiated spheroids and unstressed spheroid controls displayed a baseline cC-3 positive spheroid rate of 13% ±2. Therefore, apoptotic cell extrusion is a process that occurs naturally in MCF10A spheroids independent of epithelial differentiation status and externally applied stress. As epithelial cell extrusion from MCF10A spheroids during cultivation has not been reported thus far, it is unclear how this is connected to normal breast gland behavior.

In vivo, apoptosis in the breast gland is associated with involution, the process of reorganizing lactating breast gland epithelium to restore pre-pregnancy mammary gland structure, which has been thoroughly reviewed in the past [243]. However, the spheroids observed in this work were progressively developing towards an alveolar architecture, not losing their structure. Strikingly similar to the apoptosis rates of unstressed spheroids reported in this work was shown that 14,5% of body cells were apoptotic in rodent mammary cells of the TEB [244]. *In vivo*, apoptotic cell death of apical cells during ductal morphogenesis drives lumen formation [245,246]. Here, cells with close proximity to the existing lumen rearwards of the TEB show the highest rates of apoptosis[244]. In MCF10A spheroids, lumen formation is also driven by apoptosis as demonstrated by the presence of cC-3 signal [70]. Here, the cC-3 signal was described to be detectable in the center of MCF10A spheroids. However, the cC-3 signal observed in this work was exclusively found outside the spheroidal body or directly at the cell-BM interface. Therefore, it is possible that the apoptotic events of unstressed and differentiated spheroids is the result of normal mammary spheroid morphogenesis. However, due to absence of an existing lumen that is present *in vivo* and not the cellular orientation might be obstructed resulting in basal, instead of apical extrusion of apoptotic cells.

Cells of undifferentiated spheroids were observed to undergo apoptotic events at increased frequency in response to mechanical straining. Apoptotic cell extrusion was also observed as a mechanoresponsive process crucial to epithelial homeostasis in lung epithelial monolayers *in vitro* and in the epithelial cell lining of zebrafish embryos gastrointestinal tract *in vivo* by Jody Rosenblatt and her group [103,127,247]. Interestingly, the opening of mechanosensitive ion channel Piezo1 has been described as a mechanosensor for epithelial cell crowding. Activation of Piezo1 channels led to the production of sphingosine-1-phosphate (S1P). S1P is a signaling lipid integrated into the cell lipid bilayer. Neighboring cells bind membrane-bound S1P by a specific receptor protein, which promotes the formation of an actin ring across multiple cells surrounding the S1P-presenting cell. The S1P-presenting cell is then extruded by actin contraction and undergoes anoikis. Anoikis is a specific form of apoptosis that is induced by a lack of survival signal from cell-ECM adhesions and cell-cell contacts[248–251].

This described mechanism could also be activated in shear-strained breast spheroids and mediate the apoptotic cell extrusion observed in this work. This would indicate that strain-induced Piezo1 opening led to active extrusion of cells, which subsequently underwent anoikis due to the loss of cell-BM contacts. The cell extrusion in zebrafish epithelium and lung epithelium monolayers, however, mainly occurred apically. In contrast, in this work cells were extruded from the spheroid cell cluster via the basal cell layer, hence directly opposite to what has been described for homeostatic epithelial cell extrusion[102,247,252]. Of note, the directionality of cell extrusion was found to rely on the structure and orientation of the microtubule network of cells and depends on expression levels of the tumor suppressor adenomatous polyposis coli (APC) [253]. Lack or mutation of APC was reported to result in basal, instead of wild-type apical cell extrusion in differentiated lung epithelium monolayers[253]. However, there was no observable orientation or polarization of cells in the case of undifferentiated spheroids that were observed to extrude cells. Therefore, cell extrusion in breast spheroids as a mechanoresponse could be reliant on Piezo1 activation; missing polarization of cells however lead to basal instead of apical extrusion.

Interestingly, in approximately 25% of caspase-positive spheroids, the apoptotic cell signal was located within the cell cluster, indicating apoptotic cell death without former extrusion event. Obstruction of cell extrusion might also be the result of missing basoapical orientation.

The opening of the mechanosensitive Piezo1 ion channels has also been reported to initiate apoptosis by facilitating rapid Ca^{2+} influx, thereby activating mitochondria stress responses and apoptotic cell death [254–257]. Further, basal extrusion was observed to rely on the activation of Mitogen-Activated Protein Kinase (MAPK) and phosphoinositide 3 kinase (PI3K)/protein kinase B (AKT)/mammalian target of rapamycin (mTOR) signaling pathways [258]. Piezo1 activation was shown to play a role in the regulation of both the MAPK and the AKT/mTOR pathway [259,260]. Therefore, multiple signaling pathways that lead to apoptosis or cell extrusion are regulated by Piezo1 activation.

The shear strain in differentiated spheroid was lower than in undifferentiated spheroids. As discussed, is this most likely caused by a more mature, stable BM shielding the spheroids from ECM-transmitted strain. Therefore, it is entirely possible that higher amplitudes of shear strain would cause differentiated spheroids also to extrude apoptotic cells. Testing this, however, would have required adjusting the magnet setup of the shear stress device and repeating all previous characterization analyses that were out of this work's scope. Instead, the role of mechanosensitive ion channels and, more specifically, Piezo1 activation was investigated.

Analysis of the contribution of shear-strain-induced Piezo-1 activation is the subject of ongoing and not yet final investigations (for details, see chapter 3.1.9).In first experiments, the blocking of stretch-activated cation channels was performed by pharmacological inhibition with $GdCl_3$ [261]. Treatment of undifferentiated spheroids with $GdCl_3$ inhibited the mechanoresponsive apoptotic cell extrusion to cyclic straining. These results strongly imply a role for mechanosensitive ion channels in this mechanoresponse in breast spheroids. However, $GdCl_3$ blocks MSCs unspecifically [214]. Therefore, a role for Piezo1 channels could not be specifically identified.

Piezo1 expression levels and localization were analyzed in regard to spheroid developmental state. Initial analysis revealed an apparent decrease in Piezo1 expression and a different intracellular localization. Piezo1 signal was found to aggregate in speckles which fits previously reported observations on the Piezo1 signal of immunocytochemically treated cells [257,262]. Piezo1 signal was observed to form a continuous lining at the cell-BM interface in undifferentiated spheroids. In differentiated spheroids, this lining is only present partially. Also was Piezo1 signal often found to aggregate at cell-cell interfaces in undifferentiated spheroids but never differentiated spheroids. These observations imply that the Piezo1

protein is more abundant in undifferentiated spheroids, where it is predominantly found in the plasma membrane.

As mentioned, further investigations are necessary to understand the role and regulation of apoptosis in the normal development of MCF10A spheroids which could have implications for the branching and ductal morphogenesis of the breast gland *in vivo*.

Measurement of 3D PEG-gel deformation by microsphere tracking

In the main part of my doctoral studies, I analyzed the mechnanoresponse of BM-covered breast gland spheroids to dynamic ECM-transmitted shear strain and how this response is regulated by cellular differentiation stages.

A second intriguing question was how breast spheroids respond to ECM stiffness alterations. ECM stiffness is an essential mechanical ECM cue that stimulates cell behavior and differentiation fundamentally[263–265]. During tumor progression, reciprocal signaling circuits result in alterations of ECM composition, therefore integrin binding site composition and tissue stiffening (for details, see chapter 1.2.1). 2D Traction force microscopy is a common approach to investigate how these changes in the mechanical microenvironment, e.g., increased substrate stiffness, alter cellular force generation [266,267]. Recent studies in our group found by utilization of 2D TFM that force generation of MCF10A spheroids placed on PDMS rubber substrates of varying stiffness (0.12 kPa & 12 kPa) increases on stiffer substrates which also promotes invasive events. [33]. Thereby was shown that breast epithelium senses and reacts to matrix stiffening that also occurs during tumor progression *in vivo*.

However, reliable mechanobiological approaches were missing to explore the cellular force generation and propagation within multicellular breast gland spheroids that interact with physiologically relevant 3D matrices. Therefore, a novel confocal microscopy-based approach was developed for the measurement of 3D matrix deformations to analyze force generation at the cell-ECM interface of multicellular and polarized breast gland spheroids.

This technique had to enable an analysis of breast spheroids with a defined developmental state to investigate cell-derived matrix deformations in the context of mammary gland development and cellular differentiation state. The spheroids had to be embedded in hydrogels tunable in regards to stiffness and integrin binding sites to analyze cellular responses specific ECM modifications. Finally, spheroid-derived matrix deformations had to

be detectable with high resolution and over time to effectively investigate dynamic cellular behavior.

Synthetic PEG-hydrogels prepared by the DWI were utilized for this approach as they allowed for precise stiffness tuning (10 Pa to 7 kPa shear modulus [208]) in a range that can be found in the normal breast gland (167 Pa) or in cancerous tissue (1200 Pa Young´s modulus) [4]. While this feature was not utilized in the presented work, can these PEG-gels be further modified by integration of specific integrin binding sites to mimic alterations in ECM composition. Further, PEG-gels were not degradable by MMPs. Therefore, the mechanical properties of the matrix could not be altered due to cellular remodeling as was observed for EHS-substrates. Of note, incorporation of MMP cleavage sites into PEG-gels is possible and of interest for investigations on dynamic remodeling processes, was however not done to ensure continuity of PEG-gel stiffness in long-term (12h) analysis of spheroid-derived matrix deformation.

These PEG-based hydrogels were first confirmed to be suitable as a 3D matrix surrogate for breast epithelial spheroids. For this, spheroids were cultured in EHS-substrates for 11 days before transferring them into PEG gels of varying stiffness. The basoapical polarization schedule with gradual BM-maturation is only triggered by laminin-rich EHS substrates (for details, see chapter 1.2.3). Therefore are EHS substrates still the gold standard for MCF10A breast spheroid morphogenesis *in vitro*. So far, no synthetic hydrogels are described that allow comparable maturation. To this end, MCF10A spheroids had to be grown in EHS-matrix and transferred into PEG gels. Differentiated spheroids cultivated for three days in PEG-gels were observed to maintain their normal spheroid architecture and cellular morphology. Notable, a stiffness increase of more than three-fold (45 Pa to 170 Pa) had no discernable effect on the spheroids. Thus, it was confirmed that optimal cell culture conditions are maintained when spheroids are transferred to and cultivated in PEG-gels for at least three days.

For analysis of PEG-gel deformations, fluorescent microsphere displacement tracking was utilized. PEG-gel embedded microsphere position was acquired with a laser scanning microscope (LSM) with an airy scan detector. This allowed for imaging at a 4-fold increased speed to conventional confocal LSMs while maintaining optimal optical resolution (0.2 x 0.2 x 0.29 µm pixel size). Imaging of microspheres in a volume of 210 µm (x) x 210 µm (y) x 101 µm (z) was thereby possible in ~2.5 minutes, thereby enabling analysis of dynamic cellular force

generation with high spatiotemporal precision. While the analysis in this work was performed in two-hour intervals is this a valuable feature for future investigations.

Cross-correlation-based image analysis software developed by Dr. Ronald Springer was utilized to determine microsphere displacement in PEG-gels by 3D cuboid pattern matching between time points. To test the reliability of this approach, matrix deformation around a Poly N-isopropyl acrylamide (pNIPAM) based thermoresponsive microgel embedded into a PEG-gel (10 Pa) was analyzed. Volumetric change of the pNIPAM-gel between 25 C and 30.8 °C resulted in the displacement of PEG-gel embedded microsphere. Visual analysis of computationally determining microsphere displacement vectors confirmed that the expected radial deformation of the PEG-gel is accurately captured. Further, the calculated displacement of the microspheres increased progressively with distance from the pNIPAM-microgel. Thereby was shown that the approach of microsphere tracking in 3D matrices by pattern matching software produces reliable results.

Gel deformations were analyzed in spheroid-bearing PEG-gels with Young´s moduli of 45 Pa, 170 Pa and 400 Pa in two-hour intervals. Non-spheroid-derived gel deformations which accumulated over time were successfully separated from spheroid-derived deformation by affine correction of the 3D displacement data with software developed by Dr. Ronald Springer. The resulting displacement vector fields were observed to contain single vectors which were significantly larger than their neighboring displacement vectors and pointed in different directions. They were most likely artifacts derived from the cross-correlation-based pattern-matching algorithm. In principle, the software calculates the similarity between two patterns and calculates a cross-correlation value (1 = identical pattern). For the analysis described in this work, a threshold was set to not include displacements calculated with a value below 0.7. This was done to account for deformations within a template that most likely occurred and slightly changed patterns between time points. Therefore, it is possible that the pattern-matching approach calculated displacements for similar regions, which are not the result of real gel deformations. Interquartile range outlier detection successfully removed extremely long displacement vectors. However, this needs to be considered to increase the accuracy of microsphere displacement for future experiments. For example, higher microsphere density could be employed to increase the information in the templates, making false pattern matching less likely.

After outlier removal, the spheroid-derived deformations could be visually analyzed in detail. Interestingly, gel deformations occurred almost exclusively at the surface of the spheroid and were not propagated far into the surrounding matrix (<30 µm). Displacement vector direction indicated that force was applied mostly tangential at the spheroid's surface. This is contrary to observations made by Mark et al., who observed radial symmetric displacement within a 3D hydrogel surrounding a cancer spheroid by 2D marker bead tracking [268]. As this work shows by analyzing pNIPAM-microgel volumetric changes, are radial gel deformations well trackable with the developed microsphere displacement determination routine. This indicates that normal and breast cancer spheroids display distinct force application patterns. Such a connection needs to be further investigated to shed light on how forces are generated and propagated in normal and cancerous breast tissue.

Interestingly, spheroid-derived matrix deformations were indicated to reach a plateau after four hours of measurement, indicating that deformations are more dynamic and shorter analysis intervals should be performed to analyze how actively the spheroids shape their 3D matrix. The amplitude of the whole spheroid-derived PEG-gel deformation was shown to be increasing at lower matrix stiffness. Reconstruction of the forces the spheroids applied to the gel was not yet achieved (for more information, see chapter 6). Definitive conclusions on the cell-derived forces could therefore not be drawn.

5 Summary

The mammary gland is a mechanically active tissue that is constantly subjected to shear strain [15]. During tumor progression, the mammary tissue undergoes reciprocal stiffening which ultimately leads to cancer cell invasion. How these mechanical cues are integrated on a cellular level to control structure, function and development on a tissue scale remains elusive. This work aimed to shed light on the mechanoresponse of the mammary epithelium to physiological ECM-transmitted shear strain and 3D matrix stiffness alterations. The tools to perform such investigations are still missing. Thus, novel tools for the investigation of cellular responses of breast spheroids in response to solid shear strain and matrix stiffness alterations were developed.

First, a shear stress device was developed that allows for shear straining of natural EHS-hydrogels and embedded mammary epithelial spheroids. The strain produced in EHS-gels and spheroids were thoroughly analyzed, demonstrating the linearity and reproducibility of strain. Shear strain quantification revealed significantly lower strain amplitude in spheroids compared to their surrounding matrix. This difference was shown to be dependent on their developmental stage. These results showed that basement membrane development and multicellular architecture increase the mechanical resistance of mammary epithelium.

The device was further utilized to cyclically strain spheroids while simultaneous live cell imaging of actin was used to analyze their morphology. Thereby was revealed that spheroids lacking a matured basement membrane and basoapical polarization lose cell-cell contacts and extrude cells. Apoptosis of extruded cells was further confirmed by immunocytochemical treatment of cleaved Caspase-3 protein. Ongoing investigations suggest MSCs and specifically Piezo1 to play a role in this mechanoresponse.

To analyze changing cellular force generation of breast spheroids in response to stiffening in 3D matrices, the development of a novel 3D-TFM approach was begun. This was done by identifying cell-derived deformation in 3D matrices over time by determination of fluorescence microsphere displacement. Utilizing this approach revealed that the amplitude of spheroid-derived gel deformations decreases with an increasingly stiffer matrix. Further, visualization of spheroid-derived matrix deformation revealed that forces are applied mostly tangential to the spheroid's surface.

Together, the novel biophysical tools developed in this work enabled for the first time to analyze breast epithelial mechanobiological response mechanisms in most physiological 3D cell culture models that interact with natural and synthetic ECM surrogates.

The developed devices will pave the way for novel experimental approaches to untangle how breast epithelial development and homeostasis is modulated by the multitude of mechanical signals such as ECM stiffness, ECM composition and force application.

6 Outlook

The novel shear stress device

The shear stress device was successfully established as a tool for applying physiological stresses to breast epithelial spheroids, which was further shown to trigger profound mechanoresponse in undifferentiated breast spheroids. Preliminary results of ongoing investigations in this regard indicate a role for MSCs. More specifically, spatiotemporal expression and localization levels of Piezo1 during breast epithelial spheroid development are indicated to govern apoptotic cell extrusion in response to cyclic shear stress. The role of MSCs, and especially Piezo1, should be further investigated. For this, the treatment of spheroids with pharmacological compounds such as $GdCl_3$ during cyclic straining should be repeated to clarify whether MSCs are the main mechanosensitive element that drives apoptotic cell extrusion. Following up on these investigations, compounds such as GsMTx4 or ruthenium red should be employed to block specific MSCs to narrow the list of potential MSCs that might play a role in the observed mechanoresponse.

Combined exposure of cells to multiple mechanical cues is a common approach to understanding how mechanical cues are interpreted in concert. Alteration of substrate stiffness and simultaneous mechanical stress application is a common approach, for example, [269–273]. Investigating breast gland regulation similarly with the shear stress device could result in interesting new insights, especially for understanding cancer cell mechanoresponses. This could be achieved by mixing collagen I with the EHS-substrate to increase matrix stiffness while maintaining an overall similar protocol [274].

Also of interest is how malignant cells behave under cyclic stress. For this, growth factor treatment could be used, which was shown to promote cancer cell-like behavior in MCF10A spheroids [33].

Surface creation from imaging data and finite element analysis for 3D TFM

By employing a novel image analysis routine, it was possible to determine spheroid-derived gel deformation in 3D. The amplitude of deformations was shown to be dependent on the stiffness of the substrate.

However, the deformation amplitude is only a fraction of the information needed to reconstruct the forces that created them. Calculating these forces requires, similar to 2D TFM,

precise Information on the mechanical properties of the deformed substance and an analytical approach to deduct the forces from the observed deformations.

The extensive expertise required to accomplish such a task was not available in the DWI nor the IBI-2. A new cooperation partner with comprehensive skill in this regard was found at the Lehrstuhl für Technische Mechanik (LTM) at the Friedrich –Alexander-Universität Erlangen in the laboratory of Prof. Steinmann. At the LTM, Dr. Budday and M. Sc. Jan Hinrichsen currently provide their knowledge to perform both thorough mechanical characterization of the PEG-gels and finite element analysis.

For finite element analysis, it is necessary to know precisely the origin of force generation to deduct the force amplitude from object deformation. However, repeated imaging of fluorescent proteins during prolonged LCI can cause major damage to cells [275].

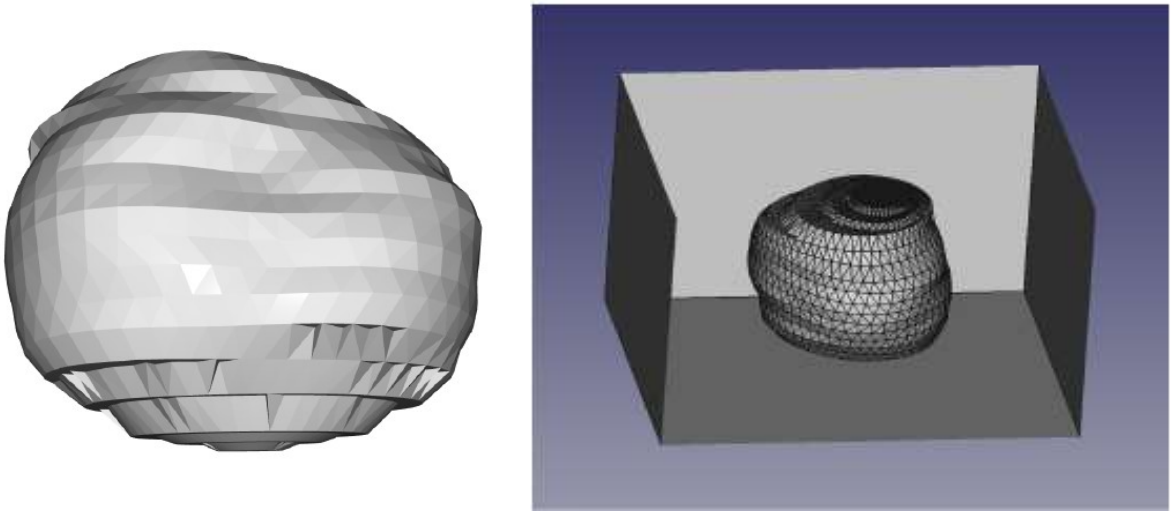

Figure 51: 3D surface generation of spheroids. 3D surfaces were created by Jonas Meier from the positional information of microspheres in PEG-gels from Z-stack imaging data. Courtesy of the Budday group.

Instead of imaging the LiveAct-RFP signal of PEG-embedded spheroids, it was decided to use a different approach. Figure 41 shows that the Spheroid-PEG-gel interface is well discernable by the absence of fluorescent microspheres, which can be utilized to generate 3D surfaces. A surface generation routine for this purpose was already successfully established by M. Sc. Jonas Meier as part of his master thesis “Entwicklung einer Softwarelösung zur Erstellung von 3D-Netzen von Zellstrukturen aus mikroskopischen Bilddaten”(figure 52).

7 Acknowledgments

First, I want to thank Prof. Rudolf Merkel for giving me the chance to work on my Ph. D. project in the IBI-2. I am incredibly thankful for having such an experienced and patient guide for my Ph. D. project, who always took his time to discuss science and share his knowledge enthusiastically and constructively.

I would also like to thank the rest of the committee members Prof. Kubitschek, Prof. Lützen and Prof. Höhelfd.

I also want to thank Dr. Erik Noetzel-Reiss for his engaging, passionate and energizing supervision and support throughout my time at the IBI-2 and the productive discussion on scientific matters. I am very grateful for his endurance with me and his understanding and empathetic character.

Of course, I also want to thank Dr. Ronald Springer, who enabled me to progress my projects and was critical to pursue my scientific investigations with his dedicated work. As his work was decisive for my projects in terms of image analysis, I am thankful for his commitment to my projects and for taking the time to find creative and productive ways to overcome obstacles.

I want to thank Susan Babu and Prof. Laura De Laporte for their manifold contributions to this thesis, as their work was crucial to my scientific endeavors.

I am thankful for the help and contribution of Jens Konrad to my projects with his ingenuity.

Many thanks also to all the members of the ME3T graduate college for the fun times and engaging discussions.

I am also very thankful to all members of the IBI-2 for their support in the lab. I am especially thankful for the support of Yannick Herfs, whose tireless work in the lab and kind nature were always reinvigorating and an invaluable aid in everyday lab work.

I also want to thank my family and close friends, who supported me throughout my life for their love, support, and stability in times of need.

Most of all, I want to thank my mother, who supported me throughout my life vigorously and unwaveringly.

8 Publication

Friedland F, Babu S, Springer R, et al. ECM-transmitted shear stress induces apoptotic cell extrusion in early breast gland development. *Front Cell Dev Biol*. 2022;10(August):1-15. doi:10.3389/fcell.2022.947430

9 Bibliography

1. Zhang W, Liu Y, Kassab GS. Flow-induced shear strain in intima of porcine coronary arteries. *J Appl Physiol*. 2007;103(2):587-593. doi:10.1152/japplphysiol.00199.2007

2. Ruwhof C, van der Laarse A. Mechanical stress-induced cardiac hypertrophy: mechanisms and signal transduction pathways. *Cardiovasc Res*. 2000;47(1):23-37. doi:10.1016/s0008-6363(00)00076-6

3. Hubmayr RD, Kallet RH. Understanding pulmonary stress-strain relationships in severe ARDS and its implications for designing a safer approach to setting the ventilator. *Respir Care*. 2018;63(2):219-226. doi:10.4187/RESPCARE.05900

4. Paszek MJ, Zahir N, Johnson KR, et al. Tensional homeostasis and the malignant phenotype. *Cancer Cell*. 2005;8(3):241-254. doi:10.1016/j.ccr.2005.08.010

5. Boughton OR, Ma S, Zhao S, et al. Measuring bone stiffness using spherical indentation. *PLoS One*. 2018;13(7):e0200475. doi:10.1371/journal.pone.0200475

6. Jansen KA, Donato DM, Balcioglu HE, Schmidt T, Danen EHJ, Koenderink GH. A guide to mechanobiology: Where biology and physics meet. *Biochim Biophys Acta - Mol Cell Res*. 2015;1853(11, Part B):3043-3052. doi:https://doi.org/10.1016/j.bbamcr.2015.05.007

7. Li D, Wang Y. Chapter 14 - Mechanobiology, tissue development, and tissue engineering. In: Lanza R, Langer R, Vacanti JP, Atala ABT-P of TE (Fifth E, eds. Academic Press; 2020:237-256. doi:https://doi.org/10.1016/B978-0-12-818422-6.00015-0

8. Rosińczuk J, Taradaj J, Dymarek R, Sopel M. Mechanoregulation of Wound Healing and Skin Homeostasis. *Biomed Res Int*. 2016;2016:3943481. doi:10.1155/2016/3943481

9. Eichinger JF, Haeusel LJ, Paukner D, Aydin RC, Humphrey JD, Cyron CJ. Mechanical homeostasis in tissue equivalents: a review. *Biomech Model Mechanobiol*. 2021;20(3):833-850. doi:10.1007/s10237-021-01433-9

10. Roy Choudhury A, Gupta S, Chaturvedi PK, Kumar N, Pandey D. Mechanobiology of Cancer Stem Cells and Their Niche. *Cancer Microenviron Off J Int Cancer Microenviron Soc*. 2019;12(1):17-27. doi:10.1007/s12307-019-00222-4

11. Yu W, Sharma S, Rao E, et al. Cancer cell mechanobiology: a new frontier for cancer research. *J Natl Cancer Cent*. 2022;2(1):10-17. doi:https://doi.org/10.1016/j.jncc.2021.11.007

12. Li X. 乳鼠心肌提取 HHS Public Access. *Physiol Behav*. 2016;176(3):139-148. doi:10.1016/j.semcdb.2016.05.010.Epithelial

13. Lee G, Han S-B, Lee J-H, Kim H-W, Kim D-H. Cancer Mechanobiology: Microenvironmental Sensing and Metastasis. *ACS Biomater Sci Eng*. 2019;5(8):3735-3752. doi:10.1021/acsbiomaterials.8b01230

14. Norris M, Mills C, Sanchez A, Wakefield-Scurr J. Do static and dynamic activities induce potentially damaging breast skin strain? *BMJ Open Sport Exerc Med*. 2020;6(1):1-10. doi:10.1136/bmjsem-2020-000770

15. Haake S, Scurr J. A method to estimate strain in the breast during exercise. *Sport Eng*. 2011;14:49-56. doi:10.1007/s12283-011-0071-6

16. Butcher DT, Alliston T, Weaver VM. A tense situation: Forcing tumour progression. *Nat Rev Cancer*. 2009;9(2):108-122. doi:10.1038/nrc2544

17. Yue B. Biology of the extracellular matrix: an overview. *J Glaucoma*. 2014;23(8 Suppl 1):S20-3. doi:10.1097/IJG.0000000000000108

18. Paluch EK, Nelson CM, Biais N, et al. Mechanotransduction: use the force(s). *BMC Biol*. 2015;13(1):47. doi:10.1186/s12915-015-0150-4

19. Jaalouk DE, Lammerding J. Mechanotransduction gone awry. *Nat Rev Mol Cell Biol*. 2009;10(1):63-73. doi:10.1038/nrm2597

20. Leiphart RJ, Chen D, Peredo AP, Loneker AE, Janmey PA. Mechanosensing at Cellular Interfaces. *Langmuir*. 2019;35(23):7509-7519. doi:10.1021/acs.langmuir.8b02841

21. Zamir A, Li G, Chase K, Moskovitch R, Sun B, Zaritsky A. Emergence of synchronized multicellular mechanosensing from spatiotemporal integration of heterogeneous single-cell information transfer. *Cell Syst*. 2022;13(9):711-723.e7. doi:https://doi.org/10.1016/j.cels.2022.07.002

22. Sanchez, Ariana D; Feldman JL. Microtubule-organizing centers: from the centrosome

to non- centrosomal sites. *Curr Opin Cell Biol*. 2015;40(4):1291-1296. doi:10.1016/j.ceb.2016.09.003.Microtubule-organizing

23. Marx A, Müller J, Mandelkow E. The structure of microtubule motor proteins. In: *Fibrous Proteins: Muscle and Molecular Motors*. Vol 71. Advances in Protein Chemistry. Academic Press; 2005:299-344. doi:https://doi.org/10.1016/S0065-3233(04)71008-6

24. Barlan K, Gelfand VI. Microtubule-based transport and the distribution, tethering, and organization of organelles. *Cold Spring Harb Perspect Biol*. 2017;9(5). doi:10.1101/cshperspect.a025817

25. van Doorn GS, Tanase C, Mulder BM, Dogterom M. On the stall force for growing microtubules. *Eur Biophys J*. 2000;29(1):2-6. doi:10.1007/s002490050245

26. Galou M, Gao J, Humbert J, et al. The importance of intermediate filaments in the adaptation of tissues to mechanical stress: evidence from gene knockout studies. *Biol cell*. 1997;89(2):85-97.

27. Biggs LC, Kim CS, Miroshnikova YA, Wickström SA. Mechanical Forces in the Skin: Roles in Tissue Architecture, Stability, and Function. *J Invest Dermatol*. 2020;140(2):284-290. doi:https://doi.org/10.1016/j.jid.2019.06.137

28. Michelot A, Drubin DG. Building distinct actin filament networks in a common cytoplasm. *Curr Biol*. 2011;21(14):R560-9. doi:10.1016/j.cub.2011.06.019

29. Chou SZ, Pollard TD. Mechanism of actin polymerization revealed by cryo-EM structures of actin filaments with three different bound nucleotides. *Proc Natl Acad Sci U S A*. 2019;116(10):4265-4274. doi:10.1073/pnas.1807028115

30. Marston SB. The rates of formation and dissociation of actin-myosin complexes. Effects of solvent, temperature, nucleotide binding and head-head interactions. *Biochem J*. 1982;203(2):453-460. doi:10.1042/bj2030453

31. Lee SH, Dominguez R. Regulation of actin cytoskeleton dynamics in cells. *Mol Cells*. 2010;29(4):311-325. doi:10.1007/s10059-010-0053-8

32. Murrell M, Oakes PW, Lenz M, Gardel ML. Forcing cells into shape: the mechanics of actomyosin contractility. *Nat Rev Mol Cell Biol*. 2015;16(8):486-498.

doi:10.1038/nrm4012

33. Gaiko-Shcherbak A, Eschenbruch J, Kronenberg NM, et al. Cell force-driven basement membrane disruption fuels egf-and stiffness-induced invasive cell dissemination from benign breast gland acini. *Int J Mol Sci*. 2021;22(8). doi:10.3390/ijms22083962

34. Eschenbruch J, Dreissen G, Springer R, et al. From microspikes to stress fibers: Actin remodeling in breast acini drives myosin ii-mediated basement membrane invasion. *Cells*. 2021;10(8). doi:10.3390/cells10081979

35. Sheetz MP et al. MBInfo © 2018 National University of Singapore. www.mechanobio.info. Published 2018.

36. Tang DD, Gerlach BD. The roles and regulation of the actin cytoskeleton, intermediate filaments and microtubules in smooth muscle cell migration. *Respir Res*. 2017;18(1):1-12. doi:10.1186/s12931-017-0544-7

37. Clark AG, Wartlick O, Salbreux G, Paluch EK. Stresses at the Cell Surface during Animal Cell Morphogenesis. *Curr Biol*. 2014;24(10):R484-R494. doi:https://doi.org/10.1016/j.cub.2014.03.059

38. Svitkina TM. Actin Cell Cortex: Structure and Molecular Organization. *Trends Cell Biol*. 2020;30(7):556-565. doi:10.1016/j.tcb.2020.03.005

39. Gibieža P, Petrikaitė V. The regulation of actin dynamics during cell division and malignancy. *Am J Cancer Res*. 2021;11(9):4050-4069. http://www.ncbi.nlm.nih.gov/pubmed/34659876%0Ahttp://www.pubmedcentral.nih.gov/articlerender.fcgi?artid=PMC8493394.

40. Miller AL. The contractile ring. *Curr Biol*. 2011;21(24):R976-8. doi:10.1016/j.cub.2011.10.044

41. Shankar J, Nabi IR. Actin cytoskeleton regulation of epithelial mesenchymal transition in metastatic cancer cells. *PLoS One*. 2015;10(3):e0119954. doi:10.1371/journal.pone.0119954

42. Son H, Moon A. Epithelial-mesenchymal Transition and Cell Invasion. *Toxicol Res*. 2010;26(4):245-252. doi:10.5487/TR.2010.26.4.245

43. Svitkina T. The actin cytoskeleton and actin-based motility. *Cold Spring Harb Perspect Biol*. 2018;10(1):1-21. doi:10.1101/cshperspect.a018267

44. Schaks M, Giannone G, Rottner K. Actin dynamics in cell migration. *Essays Biochem*. 2019;63(5):483-495. doi:10.1042/EBC20190015

45. Hotulainen P, Lappalainen P. Stress fibers are generated by two distinct actin assembly mechanisms in motile cells. *J Cell Biol*. 2006;173(3):383-394. doi:10.1083/jcb.200511093

46. Lehtimäki JI, Rajakylä EK, Tojkander S, Lappalainen P. Generation of stress fibers through myosin-driven reorganization of the actin cortex. *Elife*. 2021;10:1-43. doi:10.7554/eLife.60710

47. Callister W. *Fundamentals of Materials Science and Engineering*. Wiley; 2007.

48. Chalut KJ, Paluch EK. The Actin Cortex: A Bridge between Cell Shape and Function. *Dev Cell*. 2016;38(6):571-573. doi:10.1016/j.devcel.2016.09.011

49. Yeung T, Georges PC, Flanagan LA, et al. Effects of substrate stiffness on cell morphology, cytoskeletal structure, and adhesion. *Cell Motil Cytoskeleton*. 2005;60(1):24-34. doi:10.1002/cm.20041

50. Sun X, Phua DYZ, Axiotakis L, et al. Mechanosensing through Direct Binding of Tensed F-Actin by LIM Domains. *Dev Cell*. 2020;55(4):468-482.e7. doi:10.1016/j.devcel.2020.09.022

51. Saito M, Tucker DK, Kohlhorst D, Niessen CM, Kowalczyk AP. Classical and desmosomal cadherins at a glance. *J Cell Sci*. 2012;125(11):2547-2552. doi:10.1242/jcs.066654

52. DeMali KA, Sun X, Bui GA. Force transmission at cell-cell and cell-matrix adhesions. *Biochemistry*. 2014;53(49):7706-7717. doi:10.1021/bi501181p

53. Green KJ, Jaiganesh A, Broussard JA. Desmosomes: Essential contributors to an integrated intercellular junction network. *F1000Research*. 2019;8:1-16. doi:10.12688/f1000research.20942.1

54. Yonemura S, Wada Y, Watanabe T, Nagafuchi A, Shibata M. α-Catenin as a tension

transducer that induces adherens junction development. *Nat Cell Biol*. 2010;12(6):533-542. doi:10.1038/ncb2055

55. Buckley CD, Tan J, Anderson KL, et al. Cell adhesion. The minimal cadherin-catenin complex binds to actin filaments under force. *Science*. 2014;346(6209):1254211. doi:10.1126/science.1254211

56. Hüttelmaier S, Bubeck P, Rüdiger M, Jockusch BM. Characterization of two F-actin-binding and oligomerization sites in the cell-contact protein vinculin. *Eur J Biochem*. 1997;247(3):1136-1142. doi:10.1111/j.1432-1033.1997.01136.x

57. Angulo-Urarte A, van der Wal T, Huveneers S. Cell-cell junctions as sensors and transducers of mechanical forces. *Biochim Biophys Acta - Biomembr*. 2020;1862(9):183316. doi:10.1016/j.bbamem.2020.183316

58. McKee TJ, Perlman G, Morris M, Komarova S V. Extracellular matrix composition of connective tissues: a systematic review and meta-analysis. *Sci Rep*. 2019;9(1):1-15. doi:10.1038/s41598-019-46896-0

59. Karamanos NK, Theocharis AD, Piperigkou Z, et al. A guide to the composition and functions of the extracellular matrix. *FEBS J*. 2021;288(24):6850-6912. doi:10.1111/febs.15776

60. Hu M, Ling Z, Ren X. Extracellular matrix dynamics: tracking in biological systems and their implications. *J Biol Eng*. 2022;16(1):1-13. doi:10.1186/s13036-022-00292-x

61. Burridge K, Guilluy C. Focal adhesions, stress fibers and mechanical tension. *Exp Cell Res*. 2016;343(1):14-20. doi:10.1016/j.yexcr.2015.10.029

62. Ciobanasu C, Faivre B, Le Clainche C. Actin dynamics associated with focal adhesions. *Int J Cell Biol*. 2012;2012. doi:10.1155/2012/941292

63. Nagano M, Hoshino D, Koshikawa N, Akizawa T, Seiki M. Turnover of focal adhesions and cancer cell migration. *Int J Cell Biol*. 2012;2012:310616. doi:10.1155/2012/310616

64. Bell S, Terentjev EM. Focal Adhesion Kinase: The Reversible Molecular Mechanosensor. *Biophys J*. 2017;112(11):2439-2450. doi:https://doi.org/10.1016/j.bpj.2017.04.048

65. Wang W, Lollis EM, Bordeleau F, Reinhart-King CA. Matrix stiffness regulates vascular integrity through focal adhesion kinase activity. *FASEB J Off Publ Fed Am Soc Exp Biol*. 2019;33(1):1199-1208. doi:10.1096/fj.201800841R

66. Wozniak MA, Modzelewska K, Kwong L, Keely PJ. Focal adhesion regulation of cell behavior. *Biochim Biophys Acta - Mol Cell Res*. 2004;1692(2):103-119. doi:https://doi.org/10.1016/j.bbamcr.2004.04.007

67. Bauer MS, Baumann F, Daday C, et al. Structural and mechanistic insights into mechanoactivation of focal adhesion kinase. *Proc Natl Acad Sci*. 2019;116(14):6766-6774. doi:10.1073/pnas.1820567116

68. Sulzmaier FJ, Jean C, Schlaepfer DD. FAK in cancer: mechanistic findings and clinical applications. *Nat Rev Cancer*. 2014;14(9):598-610. doi:10.1038/nrc3792

69. Halfter W, Candiello J, Hu H, Zhang P, Schreiber E, Balasubramani M. Protein composition and biomechanical properties of in vivo-derived basement membranes. *Cell Adh Migr*. 2013;7(1):64-71. doi:10.4161/cam.22479

70. Gaiko-Shcherbak A, Fabris G, Dreissen G, Merkel R, Hoffmann B, Noetzel E. The acinar cage: Basement membranes determine molecule exchange and mechanical stability of human breast cell acini. *PLoS One*. 2015;10(12):1-20. doi:10.1371/journal.pone.0145174

71. LeBleu VS, MacDonald B, Kalluri R. Structure and Function of Basement Membranes. *Exp Biol Med*. 2007;232(9):1121-1129. doi:10.3181/0703-MR-72

72. Fabris G, Lucantonio A, Hampe N, et al. Nanoscale Topography and Poroelastic Properties of Model Tissue Breast Gland Basement Membranes. *Biophys J*. 2018;115(9):1770-1782. doi:10.1016/j.bpj.2018.09.020

73. Khalilgharibi N, Mao Y. To form and function: On the role of basement membrane mechanics in tissue development, homeostasis and disease. *Open Biol*. 2021;11(2). doi:10.1098/rsob.200360

74. Taddei I, Faraldo MM, Teulière J, Deugnier M-A, Thiery JP, Glukhova MA. Integrins in mammary gland development and differentiation of mammary epithelium. *J Mammary Gland Biol Neoplasia*. 2003;8(4):383-394.

doi:10.1023/B:JOMG.0000017426.74915.b9

75. Bergstraesser LM, Srinivasan G, Jones JC, Stahl S, Weitzman SA. Expression of hemidesmosomes and component proteins is lost by invasive breast cancer cells. *Am J Pathol*. 1995;147(6):1823-1839.

76. Nisticò P, Modugno F Di, Spada S, Bissell MJ. β1 and β4 integrins: From breast development to clinical practice. *Breast Cancer Res*. 2014;16(1):1-9. doi:10.1186/s13058-014-0459-x

77. Sun Z, Guo SS, Fässler R. Integrin-mediated mechanotransduction. 2016;215(4).

78. Schwartz MA, Assoian RK. Integrins and cell proliferation: regulation of cyclin-dependent kinases via cytoplasmic signaling pathways. *J Cell Sci*. 2001;114(Pt 14):2553-2560. doi:10.1242/jcs.114.14.2553

79. Hood JD, Cheresh DA. Role of integrins in cell invasion and migration. *Nat Rev Cancer*. 2002;2(2):91-100. doi:10.1038/nrc727

80. Wang H, Luo X, Leighton J. Extracellular Matrix and Integrins in Embryonic Stem Cell Differentiation. *Biochem insights*. 2015;8(Suppl 2):15-21. doi:10.4137/BCI.S30377

81. Martinac B. Mechanosensitive ion channels: an evolutionary and scientific tour de force in mechanobiology. *Channels (Austin)*. 2012;6(4):211-213. doi:10.4161/chan.22047

82. Martinac B. Mechanosensitive ion channels: Molecules of mechanotransduction. *J Cell Sci*. 2004;117(12):2449-2460. doi:10.1242/jcs.01232

83. Peyronnet R, Tran D, Girault T, Frachisse JM. Mechanosensitive channels: Feeling tension in a world under pressure. *Front Plant Sci*. 2014;5(OCT):1-14. doi:10.3389/fpls.2014.00558

84. Zhang Y, Daday C, Gu R-X, et al. Visualization of the mechanosensitive ion channel MscS under membrane tension. *Nature*. 2021;590(7846):509-514. doi:10.1038/s41586-021-03196-w

85. Qiu X, Müller U. Mechanically gated ion channels in mammalian hair cells. *Front Cell Neurosci*. 2018;12(April):1-10. doi:10.3389/fncel.2018.00100

86. Woo S-H, Lukacs V, de Nooij JC, et al. Piezo2 is the principal mechanotransduction channel for proprioception. *Nat Neurosci*. 2015;18(12):1756-1762. doi:10.1038/nn.4162

87. Canales Coutiño B, Mayor R. Reprint of: Mechanosensitive ion channels in cell migration. *Cells Dev*. 2021;168(April). doi:10.1016/j.cdev.2021.203730

88. Djamgoz MBA, Pchelintseva E. Mechanosensitive Ion Channels and Stem Cell Differentiation. *Bioelectricity*. 2021;3(4):249-254. doi:10.1089/bioe.2021.0037

89. Guharay F, Sachs F. Stretch-activated single ion channel currents in tissue-cultured embryonic chick skeletal muscle. *J Physiol*. 1984;352:685-701. doi:10.1113/jphysiol.1984.sp015317

90. Brehm P, Kullberg R, Moody-Corbett F. Properties of non-junctional acetylcholine receptor channels on innervated muscle of Xenopus laevis. *J Physiol*. 1984;350:631-648. doi:10.1113/jphysiol.1984.sp015222

91. Bavi N, Nikolaev YA, Bavi O, et al. *Principles of Mechanosensing at the Membrane Interface*.; 2017. doi:10.1007/978-981-10-6244-5_4

92. Wang J, Jiang J, Yang X, Zhou G, Wang L, Xiao B. Tethering Piezo channels to the actin cytoskeleton for mechanogating via the cadherin-β-catenin mechanotransduction complex. *Cell Rep*. 2022;38(6):110342. doi:10.1016/j.celrep.2022.110342

93. Gu Y, Gu C. Physiological and pathological functions of mechanosensitive ion channels. *Mol Neurobiol*. 2014;50(2):339-347. doi:10.1007/s12035-014-8654-4

94. Jung H, Kim SY, Canbakis Cecen FS, Cho Y, Kwon SK. Dysfunction of Mitochondrial Ca2+ Regulatory Machineries in Brain Aging and Neurodegenerative Diseases. *Front Cell Dev Biol*. 2020;8(December):1-11. doi:10.3389/fcell.2020.599792

95. Cox CD, Bavi N, Martinac B. Origin of the Force: The Force-From-Lipids Principle Applied to Piezo Channels. *Curr Top Membr*. 2017;79:59-96. doi:10.1016/bs.ctm.2016.09.001

96. Gnanasambandam R, Bae C, Gottlieb PA, Sachs F. Ionic selectivity and permeation properties of human PIEZO1 channels. *PLoS One*. 2015;10(5):1-16. doi:10.1371/journal.pone.0125503

97. Hennes A, Held K, Boretto M, et al. Functional expression of the mechanosensitive PIEZO1 channel in primary endometrial epithelial cells and endometrial organoids. *Sci Rep*. 2019;9(1):1-14. doi:10.1038/s41598-018-38376-8

98. Sun W, Chi S, Li Y, et al. The mechanosensitive Piezo1 channel is required for bone formation. Rosen CJ, Dietz HC, Sherk V, Haelterman NA, eds. *Elife*. 2019;8:e47454. doi:10.7554/eLife.47454

99. Dalghi MG, Clayton DR, Ruiz WG, et al. Expression and distribution of PIEZO1 in the mouse urinary tract. *Am J Physiol Renal Physiol*. 2019;317(2):F303-F321. doi:10.1152/ajprenal.00214.2019

100. Ortuste Quiroga HP, Ganassi M, Yokoyama S, et al. Fine-Tuning of Piezo1 Expression and Activity Ensures Efficient Myoblast Fusion during Skeletal Myogenesis. *Cells*. 2022;11(3). doi:10.3390/cells11030393

101. Eisenhoffer GT, Loftus PD, Yoshigi M, et al. Crowding induces live cell extrusion to maintain homeostatic cell numbers in epithelia. *Nature*. 2012;484(7395):546-549. doi:10.1038/nature10999

102. Andrade D, Rosenblatt J. Apoptotic regulation of epithelial cellular extrusion. *Apoptosis*. 2011;16(5):491-501. doi:10.1007/s10495-011-0587-z

103. Gu Y, Shea J, Slattum G, et al. Defective apical extrusion signaling contributes to aggressive tumor hallmarks. *Elife*. 2015;2015(4):1-17. doi:10.7554/eLife.04069

104. Guo Y, Pan W, Liu S, Shen Z, Xu Y, Hu L. ERK/MAPK signalling pathway and tumorigenesis (Review). *Exp Ther Med*. 2020:1997-2007. doi:10.3892/etm.2020.8454

105. Shen Y, Pan Y, Guo S, Sun L, Zhang C, Wang L. The roles of mechanosensitive ion channels and associated downstream MAPK signaling pathways in PDLC mechanotransduction. *Mol Med Rep*. 2020;21(5):2113-2122. doi:10.3892/mmr.2020.11006

106. Lu Y, Liu B, Liu Y, Yu X, Cheng G. Dual effects of active erk in cancer: A potential target for enhancing radiosensitivity (review). *Oncol Lett*. 2020;20(2):993-1000. doi:10.3892/ol.2020.11684

107. Sulzmaier FJ, Ramos JW. RSK isoforms in cancer cell invasion and metastasis. *Cancer*

Res. 2013;73(20):6099-6105. doi:10.1158/0008-5472.CAN-13-1087

108. Ranade SS, Qiu Z, Woo SH, et al. Piezo1, a mechanically activated ion channel, is required for vascular development in mice. *Proc Natl Acad Sci U S A*. 2014;111(28):10347-10352. doi:10.1073/pnas.1409233111

109. Goessler UR, Bugert P, Bieback K, et al. Integrin expression in stem cells from bone marrow and adipose tissue during chondrogenic differentiation. *Int J Mol Med*. 2008;21(3):271-279.

110. Sugimoto A, Miyazaki A, Kawarabayashi K, et al. Piezo type mechanosensitive ion channel component 1 functions as a regulator of the cell fate determination of mesenchymal stem cells. *Sci Rep*. 2017;7. doi:10.1038/s41598-017-18089-0

111. Fata JE, Werb Z, Bissell MJ. Regulation of mammary gland branching morphogenesis by the extracellular matrix and its remodeling enzymes. *Breast Cancer Res*. 2004;6(1):1-11. doi:10.1186/bcr634

112. Hannan FM, Elajnaf T, Vandenberg LN, Kennedy SH, Thakker R V. Hormonal regulation of mammary gland development and lactation. *Nat Rev Endocrinol*. 2022. doi:10.1038/s41574-022-00742-y

113. Oftedal OT. The evolution of milk secretion and its ancient origins. *Animal*. 2012;6(3):355-368. doi:10.1017/S1751731111001935

114. Bao Z, Lin J, Ye L, et al. Modulation of Mammary Gland Development and Milk Production by Growth Hormone Expression in GH Transgenic Goats. *Front Physiol*. 2016;7(June):1-8. doi:10.3389/fphys.2016.00278

115. Fata JE, Werb Z, Bissell MJ. Regulation of mammary gland branching morphogenesis by the extracellular matrix and its remodeling enzymes. *Breast Cancer Res*. 2004;6(1):1-11. doi:10.1186/bcr634

116. Speroni L, Schaeberle CM, Sonnenschein C, Soto AM. Mammary gland development. *Encycl Reprod*. 2018:786-792. doi:10.1016/B978-0-12-801238-3.64420-3

117. Colleluori G, Perugini J, Barbatelli G, Cinti S. Mammary gland adipocytes in lactation cycle, obesity and breast cancer. *Rev Endocr Metab Disord*. 2021;22(2):241-255. doi:10.1007/s11154-021-09633-5

118. Macias H, Hinck L. Mammary gland development. *Wiley Interdiscip Rev Dev Biol*. 2012;1(4):533-557. doi:10.1002/wdev.35

119. Sternlicht MD. Key stages in mammary gland development: The cues that regulate ductal branching morphogenesis. *Breast Cancer Res*. 2005;8(1). doi:10.1186/bcr1368

120. Paavolainen O, Peuhu E. Integrin-mediated adhesion and mechanosensing in the mammary gland. *Semin Cell Dev Biol*. 2021;114:113-125. doi:10.1016/j.semcdb.2020.10.010

121. Paine IS, Lewis MT. The Terminal End Bud: the Little Engine that Could. *J Mammary Gland Biol Neoplasia*. 2017;22(2):93-108. doi:10.1007/s10911-017-9372-0

122. Pellacani D, Tan S, Lefort S, Eaves CJ. Transcriptional regulation of normal human mammary cell heterogeneity and its perturbation in breast cancer. *EMBO J*. 2019;38(14):1-19. doi:10.15252/embj.2018100330

123. Vidi P-A, Bissell M, Lelièvre S. Three-Dimensional Culture of Human Breast Epithelial Cells: The How and the Why. *Methods Mol Biol*. 2013;945:193-219. doi:10.1007/978-1-62703-125-7_13

124. Neville MC, Allen JC, Watters C. The Mechanisms of Milk Secretion BT - Lactation: Physiology, Nutrition, and Breast-Feeding. In: Neville MC, Neifert MR, eds. Boston, MA: Springer US; 1983:49-102. doi:10.1007/978-1-4613-3688-4_3

125. Jena MK. Molecular mechanism of mammary gland involution : An update. *Dev Biol*. 2019;445(2):145-155. doi:10.1016/j.ydbio.2018.11.002

126. Nerger BA, Jaslove JM, Elashal HE, et al. Local accumulation of extracellular matrix regulates global morphogenetic patterning in the developing mammary gland. *Curr Biol*. 2021;31(9):1903-1917.e6. doi:10.1016/j.cub.2021.02.015

127. Yin Y, Deng X, Liu Z, et al. CD151 represses mammary gland development by maintaining the niches of progenitor cells CD151 represses mammary gland development by maintaining the niches of progenitor cells. 2015;4101. doi:10.4161/15384101.2015.945823

128. Liu K, Cheng L, Flesken-Nikitin A, Huang L, Nikitin AY, Pauli BU. Conditional knockout of fibronectin abrogates mouse mammary gland lobuloalveolar differentiation. *Dev Biol*.

2010;346(1):11-24. doi:10.1016/j.ydbio.2010.07.001

129. Pratt SJP, Lee RM, Martin SS. The Mechanical Microenvironment in Breast Cancer. *Cancers (Basel)*. 2020;12(6). doi:10.3390/cancers12061452

130. Bissell MJ, Hall HG, Parry G. How does the extracellular matrix direct gene expression? *J Theor Biol*. 1982;99(1):31-68. doi:10.1016/0022-5193(82)90388-5

131. Thorne JT, Segal TR, Chang S, Jorge S, Segars JH, Leppert PC. Dynamic reciprocity between cells and their microenvironment in reproduction. *Biol Reprod*. 2015;92(1):25. doi:10.1095/biolreprod.114.121368

132. Riehl BD, Kim E, Bouzid T, Lim JY. The Role of Microenvironmental Cues and Mechanical Loading Milieus in Breast Cancer Cell Progression and Metastasis . *Front Bioeng Biotechnol* . 2021;8. https://www.frontiersin.org/articles/10.3389/fbioe.2020.608526.

133. Boyd NF, Li Q, Melnichouk O, et al. Evidence That Breast Tissue Stiffness Is Associated with Risk of Breast Cancer. 2014;9(7):1-8. doi:10.1371/journal.pone.0100937

134. Yavuz BG, Gunaydin G, Gedik ME, Kos K. Cancer associated fibroblasts sculpt tumour microenvironment by recruiting monocytes and inducing immunosuppressive PD-1 + TAMs. 2019;(November 2018):1-15. doi:10.1038/s41598-019-39553-z

135. Ping Q, Yan R, Cheng X, et al. Cancer-associated fibroblasts: overview, progress, challenges, and directions. *Cancer Gene Ther*. 2021;28(9):984-999. doi:10.1038/s41417-021-00318-4

136. Kawano S, Kojima M, Higuchi Y, et al. Assessment of elasticity of colorectal cancer tissue, clinical utility, pathological and phenotypical relevance. *Cancer Sci*. 2015;106(9):1232-1239. doi:10.1111/cas.12720

137. Park S, Shi Y, Kim BC, et al. Force-dependent trans-endocytosis by breast cancer cells depletes costimulatory receptor CD80 and attenuates T cell activation. *Biosens Bioelectron*. 2020;165:112389. doi:10.1016/j.bios.2020.112389

138. Kraning-rush CM, Califano JP, Reinhart-king CA. Cellular Traction Stresses Increase with Increasing Metastatic Potential. 2012;7(2). doi:10.1371/journal.pone.0032572

139. Balcioglu HE, Harkes R, Danen EHJ, Schmidt T. Substrate rigidity modulates traction forces and stoichiometry of cell-matrix adhesions. *J Chem Phys*. 2022;156(8):85101. doi:10.1063/5.0077004

140. Rheinlaender J. RSC Advances Spatial correlation of cell sti ff ness and traction forces in cancer cells measured with combined. 2021:13951-13956. doi:10.1039/d1ra01277k

141. Harrison R. G.: Observations on the living developing nerve fiber. *Anat Rec*. 1906;1:116-118.

142. Carter M, Shieh JC. Chapter 13 - Cell Culture Techniques. In: Carter M, Shieh JC, eds. *Guide to Research Techniques in Neuroscience*. New York: Academic Press; 2010:281-296. doi:https://doi.org/10.1016/B978-0-12-374849-2.00013-6

143. Spink BC, Cole RW, Katz BH, Gierthy JF, Bradley LM, Spink DC. Inhibition of MCF-7 breast cancer cell proliferation by MCF-10A breast epithelial cells in coculture. *Cell Biol Int*. 2006;30(3):227-238. doi:https://doi.org/10.1016/j.cellbi.2005.11.006

144. Mubeen AA, Chaudhary S, R AB, Chandrashekara C V. Dynamic analysis of MCF-10A and MCF-7 : A simulation approach. 2020:126-132. doi:10.21595/vp.2020.21392

145. Geltmeier A, Rinner B, Bade D, et al. Characterization of Dynamic Behaviour of MCF7 and MCF10A Cells in Ultrasonic Field Using Modal and Harmonic Analyses. *PLoS One*. 2015;10(8):e0134999. doi:10.1371/journal.pone.0134999

146. Amaro F, Silva D, Reguengo H, Oliveira JC, Quintas C. β -Adrenoceptor Activation in Breast MCF-10A Cells Induces a Pattern of Catecholamine Production Similar to that of Tumorigenic MCF-7 Cells.

147. Parry G, Lee EY, Farson D, Koval M, Bissell MJ. Collagenous substrata regulate the nature and distribution of glycosaminoglycans produced by differentiated cultures of mouse mammary epithelial cells. *Exp Cell Res*. 1985;156(2):487-499. doi:10.1016/0014-4827(85)90556-7

148. Jensen C, Teng Y. Is It Time to Start Transitioning From 2D to 3D Cell Culture? *Front Mol Biosci*. 2020;7(March):1-15. doi:10.3389/fmolb.2020.00033

149. Anton D, Burckel H, Josset E, Noel G. Three-dimensional cell culture: A breakthrough in vivo. *Int J Mol Sci*. 2015;16(3):5517-5527. doi:10.3390/ijms16035517

150. Kapałczyńska M, Kolenda T, Przybyła W, et al. 2D and 3D cell cultures – a comparison of different. *Arch Med Sci*. 2016;14(4):910-919.

151. Elia N, Lippincott-schwartz J. Culturing Three Dimensional MDCK cells for Analyzing Intracellular Dynamics. *Curr Protoc Cell Biol*. 209AD. doi:10.1002/0471143030.cb0422s43.Culturing

152. Hill SM, Padilla-Rodriguez M, Clements A, et al. Optimized in vitro three-dimensional invasion assay for quantifying a wide range of cancer cell invasive behavior. *STAR Protoc*. 2022;3(3):101516. doi:10.1016/j.xpro.2022.101516

153. Baruffaldi D, Palmara G, Pirri C, Frascella F. 3D Cell Culture: Recent Development in Materials with Tunable Stiffness. *ACS Appl Bio Mater*. 2021;4(3):2233-2250. doi:10.1021/acsabm.0c01472

154. Campbell JJ, Watson CJ. Three-dimensional culture models of mammary gland. *Organogenesis*. 2009;5(2):43-49. doi:10.4161/org.5.2.8321

155. Debnath J, Muthuswamy SK, Brugge JS. Morphogenesis and oncogenesis of MCF-10A mammary epithelial acini grown in three-dimensional basement membrane cultures. *Methods*. 2003;30(3):256-268. doi:10.1016/s1046-2023(03)00032-x

156. Riga A, Castiglioni VG, Boxem M. New insights into apical-basal polarization in epithelia. *Curr Opin Cell Biol*. 2020;62:1-8. doi:10.1016/j.ceb.2019.07.017

157. Ahuja N, Cleaver O. The cell cortex as mediator of pancreatic epithelial development and endocrine differentiation. *Curr Opin Genet Dev*. 2022;72:118-127. doi:10.1016/j.gde.2021.11.004

158. Krtolica A, Genbacev O, Escobedo C, et al. Disruption of Apical-Basal Polarity of Human Embryonic Stem Cells Enhances Hematoendothelial Differentiation. *Stem Cells*. 2007;25(9):2215-2223. doi:10.1634/stemcells.2007-0230

159. Pogoda K, Bucki R, Byfield FJ, et al. Soft Substrates Containing Hyaluronan Mimic the Effects of Increased Stiffness on Morphology, Motility, and Proliferation of Glioma Cells. *Biomacromolecules*. 2017;18(10):3040-3051. doi:10.1021/acs.biomac.7b00324

160. Serafim RB, da Silva P, Cardoso C, et al. Expression Profiling of Glioblastoma Cell Lines Reveals Novel Extracellular Matrix-Receptor Genes Correlated With the

Responsiveness of Glioma Patients to Ionizing Radiation. *Front Oncol*. 2021;11(May):1-14. doi:10.3389/fonc.2021.668090

161. Ondeck MG, Kumar A, Placone JK, et al. Dynamically stiffened matrix promotes malignant transformation of mammary epithelial cells via collective mechanical signaling. *Proc Natl Acad Sci U S A*. 2019;116(9):3502-3507. doi:10.1073/pnas.1814204116

162. Fattet L, Jung HY, Matsumoto MW, et al. Matrix Rigidity Controls Epithelial-Mesenchymal Plasticity and Tumor Metastasis via a Mechanoresponsive EPHA2/LYN Complex. *Dev Cell*. 2020;54(3):302-316.e7. doi:10.1016/j.devcel.2020.05.031

163. Cheng Q, Bilgin CC, Fonteney G, et al. Stiffness of the microenvironment upregulates ERBB2 expression in 3D cultures of MCF10A within the range of mammographic density. *Sci Rep*. 2016;6(February):1-14. doi:10.1038/srep28987

164. Joshi SK, Keck JM, Eide CA, et al. ERBB2/HER2 mutations are transforming and therapeutically targetable in leukemia. *Leukemia*. 2020;34(10):2798-2804. doi:10.1038/s41375-020-0844-7

165. Ruud KF, Hiscox WC, Yu I, Chen RK, Li W. Distinct phenotypes of cancer cells on tissue matrix gel. *Breast Cancer Res*. 2020;22(1):1-22. doi:10.1186/s13058-020-01321-7

166. Denisin AK, Pruitt BL. Tuning the Range of Polyacrylamide Gel Stiffness for Mechanobiology Applications. *ACS Appl Mater Interfaces*. 2016;8(34):21893-21902. doi:10.1021/acsami.5b09344

167. M. Jonker A, A. Bode S, H. Kusters A, van Hest JCM, Löwik DWPM. Soft PEG-Hydrogels with Independently Tunable Stiffness and RGDS-Content for Cell Adhesion Studies. *Macromol Biosci*. 2015;15(10):1338-1347. doi:https://doi.org/10.1002/mabi.201500110

168. Chen W, Zhang Y, Kumari J, Engelkamp H, Kouwer PHJ. Magnetic Stiffening in 3D Cell Culture Matrices. *Nano Lett*. 2021;21(16):6740-6747. doi:10.1021/acs.nanolett.1c00371

169. Stowers RS, Allen SC, Suggs LJ. Dynamic phototuning of 3D hydrogel stiffness. *Proc Natl Acad Sci*. 2015;112(7):1953-1958. doi:10.1073/pnas.1421897112

170. Ma C, Liu K, Li Q, et al. Synthetic Extracellular Matrices for 3D Culture of Schwann Cells, Hepatocytes, and HUVECs. *Bioengineering*. 2022;9(9):1-15. doi:10.3390/bioengineering9090453

171. Licht C, Rose JC, Anarkoli AO, et al. Synthetic 3D PEG-Anisogel Tailored with Fibronectin Fragments Induce Aligned Nerve Extension. *Biomacromolecules*. 2019;20(11):4075-4087. doi:10.1021/acs.biomac.9b00891

172. Tibbitt MW, Anseth KS. Hydrogels as extracellular matrix mimics for 3D cell culture. *Biotechnol Bioeng*. 2009;103(4):655-663. doi:10.1002/bit.22361

173. Yang B, Wei K, Loebel C, et al. Enhanced mechanosensing of cells in synthetic 3D matrix with controlled biophysical dynamics. *Nat Commun*. 2021;12(1). doi:10.1038/s41467-021-23120-0

174. Ashworth JC, Thompson JL, James JR, et al. Peptide gels of fully-defined composition and mechanics for probing cell-cell and cell-matrix interactions in vitro. *Matrix Biol*. 2020;85-86:15-33. doi:10.1016/j.matbio.2019.06.009

175. Schwarz US, Soiné JRD. Traction force microscopy on soft elastic substrates: A guide to recent computational advances. *Biochim Biophys Acta - Mol Cell Res*. 2015;1853(11):3095-3104. doi:10.1016/j.bbamcr.2015.05.028

176. Merkel R, Kirchgessner N, Cesa CM, Hoffmann B. Cell force microscopy on elastic layers of finite thickness. *Biophys J*. 2007;93(9):3314-3323. doi:10.1529/biophysj.107.111328

177. Cesa C, Kirchgessner N, Mayer D, Schwarz U, Hoffmann B, Merkel R. Micropatterned silicone elastomer substrates for high resolution analysis of cellular force patterns. *Rev Sci Instrum*. 2007;78:34301. doi:10.1063/1.2712870

178. Faust U, Hampe N, Rubner W, et al. Cyclic stress at mHz frequencies aligns fibroblasts in direction of zero strain. *PLoS One*. 2011;6(12). doi:10.1371/journal.pone.0028963

179. Wysotzki P, Gimsa J. Surface Coatings Modulate the Differences in the Adhesion Forces of Eukaryotic and Prokaryotic Cells as Detected by Single Cell Force Microscopy. *Int J Biomater*. 2019;2019. doi:10.1155/2019/7024259

180. Mulligan JA, Feng X, Adie SG. Quantitative reconstruction of time-varying 3D cell

forces with traction force optical coherence microscopy. *Sci Rep*. 2019;9(1):1-14. doi:10.1038/s41598-019-40608-4

181. Legant WR, Choi CK, Miller JS, et al. Multidimensional traction force microscopy reveals out-of-plane rotational moments about focal adhesions. *Proc Natl Acad Sci*. 2013;110(3):881-886. doi:10.1073/pnas.1207997110

182. Koch TM, Münster S, Bonakdar N, Butler JP, Fabry B. 3D Traction Forces in Cancer Cell Invasion. *PLoS One*. 2012;7(3):e33476. https://doi.org/10.1371/journal.pone.0033476.

183. Mariano CA, Sattari S, Quiros KAM, Nelson TM, Eskandari M. Examining lung mechanical strains as influenced by breathing volumes and rates using experimental digital image correlation. *Respir Res*. 2022;23(1):1-13. doi:10.1186/s12931-022-01999-7

184. Marwick TH. Measurement of strain and strain rate by echocardiography: Ready for prime time? *J Am Coll Cardiol*. 2006;47(7):1313-1327. doi:10.1016/j.jacc.2005.11.063

185. Hirsch S, Klatt D, Freimann F, Scheel M, Braun J, Sack I. In vivo measurement of volumetric strain in the human brain induced by arterial pulsation and harmonic waves. *Magn Reson Med*. 2013;70(3):671-683. doi:10.1002/mrm.24499

186. Al-Maslamani NA, Khilan AA, Horn HF. Design of a 3D printed, motorized, uniaxial cell stretcher for microscopic and biochemical analysis of mechanotransduction. *Biol Open*. 2021;10(2). doi:10.1242/bio.057778

187. Kreutzer J, Viehrig M, Pölönen RP, et al. Pneumatic unidirectional cell stretching device for mechanobiological studies of cardiomyocytes. *Biomech Model Mechanobiol*. 2020;19(1):291-303. doi:10.1007/s10237-019-01211-8

188. Xu K, Liu X, Li X, et al. Effect of Electrical and Electromechanical Stimulation on PC12 Cell Proliferation and Axon Outgrowth. *Front Bioeng Biotechnol*. 2021;9(October):1-10. doi:10.3389/fbioe.2021.757906

189. Atcha H, Davis CT, Sullivan NR, et al. A Low-Cost Mechanical Stretching Device for Uniaxial Strain of Cells: A Platform for Pedagogy in Mechanobiology. *J Biomech Eng*. 2018;140(8):1-9. doi:10.1115/1.4039949

190. Kada K, Yasui K, Naruse K, Kamiya K, Kodama I, Toyama J. Orientation change of cardiocytes induced by cyclic stretch stimulation: time dependency and involvement of protein kinases. *J Mol Cell Cardiol*. 1999;31(1):247-259. doi:10.1006/jmcc.1998.0865

191. Abraham JA, Blaschke S, Tarazi S, et al. NSCs Under Strain—Unraveling the Mechanoprotective Role of Differentiating Astrocytes in a Cyclically Stretched Coculture With Differentiating Neurons. *Front Cell Neurosci*. 2021;15(September):1-14. doi:10.3389/fncel.2021.706585

192. Mao T, He Y, Gu Y, et al. Critical Frequency and Critical Stretching Rate for Reorientation of Cells on a Cyclically Stretched Polymer in a Microfluidic Chip. *ACS Appl Mater Interfaces*. 2021;13(12):13934-13948. doi:10.1021/acsami.0c21186

193. Na S, Trache A, Trzeciakowski J, Sun Z, Meininger GA, Humphrey JD. Time-dependent changes in smooth muscle cell stiffness and focal adhesion area in response to cyclic equibiaxial stretch. *Ann Biomed Eng*. 2008;36(3):369-380. doi:10.1007/s10439-008-9438-7

194. Yeh C-H, Tsai S-H, Wu L-W, Lin Y-C. Using a co-culture microsystem for cell migration under fluid shear stress. *Lab Chip*. 2011;11:2583-2590. doi:10.1039/c1lc20113a

195. Tsao CW, Cheng YC, Cheng JH. Fluid flow shear stress stimulation on a multiplex microfluidic device for rat bone marrow stromal cell differentiation enhancement. *Micromachines*. 2015;6(12):1996-2009. doi:10.3390/mi6121470

196. Benbrahim A, L'Italien GJ, Milinazzo BB, et al. A compliant tubular device to study the influences of wall strain and fluid shear stress on cells of the vascular wall. *J Vasc Surg*. 1994;20(2):184-194. doi:10.1016/0741-5214(94)90005-1

197. Dash SK, Patra B, Sharma V, Das SK, Verma RS. Fluid shear stress in a logarithmic microfluidic device enhances cancer cell stemness marker expression. *Lab Chip*. 2022;22(11):2200-2211. doi:10.1039/D1LC01139A

198. Moore JEJ, Bürki E, Suciu A, et al. A device for subjecting vascular endothelial cells to both fluid shear stress and circumferential cyclic stretch. *Ann Biomed Eng*. 1994;22(4):416-422. doi:10.1007/BF02368248

199. Yuan L, Sakamoto N, Song G, Sato M. High-level Shear Stress Stimulates Endothelial Differentiation and VEGF Secretion by Human Mesenchymal Stem Cells. *Cell Mol Bioeng*. 2013;6(2):220-229. doi:10.1007/s12195-013-0275-x

200. Shojaei S, Tafazzoli-Shahdpour M, Shokrgozar MA, Haghighipour N. Effects of Mechanical and Chemical Stimuli on Differentiation of Human Adipose-Derived Stem Cells into Endothelial Cells. *Int J Artif Organs*. 2013;36(9):663-673. doi:10.5301/ijao.5000242

201. Bassaneze V, Barauna VG, Lavini-Ramos C, et al. Shear Stress Induces Nitric Oxide–Mediated Vascular Endothelial Growth Factor Production in Human Adipose Tissue Mesenchymal Stem Cells. *Stem Cells Dev*. 2009;19(3):371-378. doi:10.1089/scd.2009.0195

202. Maul TM, Chew DW, Nieponice A, Vorp DA. Mechanical stimuli differentially control stem cell behavior: morphology, proliferation, and differentiation. *Biomech Model Mechanobiol*. 2011;10(6):939-953. doi:10.1007/s10237-010-0285-8

203. Erlich A, Étienne J, Fouchard J, Wyatt T. How dynamic prestress governs the shape of living systems, from the subcellular to tissue scale. *Interface Focus*. 2022;12(6):20220038. doi:10.1098/rsfs.2022.0038

204. Friedland F, Babu S, Springer R, et al. ECM-transmitted shear stress induces apoptotic cell extrusion in early breast gland development. *Front Cell Dev Biol*. 2022;10(August):1-15. doi:10.3389/fcell.2022.947430

205. Stacey GN. Cell culture contamination. *Methods Mol Biol*. 2011;731:79-91. doi:10.1007/978-1-61779-080-5_7

206. Hersch N, Wolters B, Dreissen G, et al. The constant beat: cardiomyocytes adapt their forces by equal contraction upon environmental stiffening. *Biol Open*. 2013;2(3):351-361. doi:10.1242/bio.20133830

207. Gaiko-Shcherbak A. Functional and Mechanical in vitro Analyses of the Mammary Gland Basement Membrane as a Barrier During Cancer Invasion. 2013.

208. Babu S, Chen I, Vedaraman S, et al. How do the Local Physical, Biochemical, and Mechanical Properties of an Injectable Synthetic Anisotropic Hydrogel Affect Oriented

Nerve Growth? *Adv Funct Mater*. 2022;n/a(n/a):2202468. doi:https://doi.org/10.1002/adfm.202202468

209. Nam S, Lee J, Brownfield D, Chaudhuri O. Viscoplasticity Enables Mechanical Remodeling of Matrix by Cells. *Biophys J*. 2016;111. doi:10.1016/j.bpj.2016.10.002

210. Boudou T, Ohayon J, Picart C, Tracqui P. An extended relationship for the characterization of Young's modulus and Poisson's ratio of tunable polyacrylamide gels. *Biorheology*. 2006;43(6):721-728.

211. Wang H, Lacoche S, Huang L, Xue B, Muthuswamy SK. Rotational motion during three-dimensional morphogenesis of mammary epithelial acini relates to laminin matrix assembly. *Proc Natl Acad Sci*. 2013;110(1):163-168. doi:10.1073/pnas.1201141110

212. Mashima T, Naito M, Tsuruo T. Caspase-mediated cleavage of cytoskeletal actin plays a positive role in the process of morphological apoptosis. *Oncogene*. 1999;18(15):2423-2430. doi:10.1038/sj.onc.1202558

213. Santavanond JP, Rutter SF, Atkin-Smith GK, Poon IKH. Apoptotic Bodies: Mechanism of Formation, Isolation and Functional Relevance. *Subcell Biochem*. 2021;97:61-88. doi:10.1007/978-3-030-67171-6_4

214. Yoo S, Mittelstein DR, Hurt RC, Lacroix J, Shapiro MG. Focused ultrasound excites cortical neurons via mechanosensitive calcium accumulation and ion channel amplification. *Nat Commun*. 2022;13(1):493. doi:10.1038/s41467-022-28040-1

215. Ermakov YA, Kamaraju K, Sengupta K, Sukharev S. Gadolinium ions block mechanosensitive channels by altering the packing and lateral pressure of anionic lipids. *Biophys J*. 2010;98(6):1018-1027. doi:10.1016/j.bpj.2009.11.044

216. Wolff HJM, Linkhorst J, Göttlich T, et al. Soft temperature-responsive microgels of complex shape in stop-flow lithography. *Lab Chip*. 2020;20(2):285-295. doi:10.1039/c9lc00749k

217. Salmons BS, Katz DR, Trawick ML. Correction of distortion due to thermal drift in scanning probe microscopy. *Ultramicroscopy*. 2010;110(4):339-349. doi:10.1016/j.ultramic.2010.01.006

218. Kleinberg DL, Ruan W. IGF-I, GH, and sex steroid effects in normal mammary gland

development. *J Mammary Gland Biol Neoplasia*. 2008;13(4):353-360. doi:10.1007/s10911-008-9103-7

219. Stowers RS, Allen SC, Sanchez K, et al. Extracellular Matrix Stiffening Induces a Malignant Phenotypic Transition in Breast Epithelial Cells. *Cell Mol Bioeng*. 2017;10(1):114-123. doi:10.1007/s12195-016-0468-1

220. Debnath J, Mills KR, Collins NL, Reginato MJ, Muthuswamy SK, Brugge JS. The role of apoptosis in creating and maintaining luminal space within normal and oncogene-expressing mammary acini. *Cell*. 2002;111(1):29-40. doi:10.1016/s0092-8674(02)01001-2

221. Li Y, Huang G, Li M, et al. An approach to quantifying 3D responses of cells to extreme strain. *Sci Rep*. 2016;6(November 2015):1-9. doi:10.1038/srep19550

222. Huang R, Xu L, Wang Y, et al. Efficient fabrication of stretching hydrogels with programmable strain gradients as cell sheet delivery vehicles. *Mater Sci Eng C*. 2021;129:112415. doi:https://doi.org/10.1016/j.msec.2021.112415

223. Mei Q, Yuen HY, Zhao X. Mechanical stretching of 3D hydrogels for neural stem cell differentiation. *Bio-Design Manuf*. 2022;5(4):714-728. doi:10.1007/s42242-022-00209-z

224. Reed J, Walczak WJ, Petzold ON, Gimzewski JK. In situ mechanical interferometry of matrigel films. *Langmuir*. 2009;25(1):36-39. doi:10.1021/la8033098

225. Chen JH, Chan S, Zhang Y, Li S, Chang RF, Su MY. Evaluation of breast stiffness measured by ultrasound and breast density measured by MRI using a prone-supine deformation model. *Biomark Res*. 2019;7(1):1-10. doi:10.1186/s40364-019-0171-1

226. Funaki M, Janmey PA. Chapter 23 - Technologies to Engineer Cell Substrate Mechanics in Hydrogels. In: Vishwakarma A, Karp JMBT-B and E of SCN, eds. Boston: Academic Press; 2017:363-373. doi:https://doi.org/10.1016/B978-0-12-802734-9.00023-8

227. Soofi SS, Last JA, Lliensiek SJ, Nealey PF, Murphy CJ. Elastic modulus of Matrigel as determined by AFM. *J Struct Biol*. 2009;167(3):216-219. doi:10.1016/j.jsb.2009.05.005.The

228. Stowers RS, Allen SC, Sanchez K, et al. Extracellular Matrix Stiffening Induces a

Malignant Phenotypic Transition in Breast Epithelial Cells. *Cell Mol Bioeng*. 2017;10(1):114-123. doi:10.1007/s12195-016-0468-1

229. Méhes E, Biri-Kovács B, Isai DG, Gulyás M, Nyitray L, Czirók A. Matrigel patterning reflects multicellular contractility. *PLOS Comput Biol*. 2019;15(10):e1007431. https://doi.org/10.1371/journal.pcbi.1007431.

230. Ramos-Lewis W, Page-McCaw A. Basement membrane mechanics shape development: Lessons from the fly. *Matrix Biol*. 2019;75-76:72-81. doi:10.1016/j.matbio.2018.04.004

231. Morrissey MA, Sherwood DR. An active role for basement membrane assembly and modification in tissue sculpting. *J Cell Sci*. 2015;128(9):1661-1668. doi:10.1242/jcs.168021

232. Leclech C, Natale CF, Barakat AI. The basement membrane as a structured surface – role in vascular health and disease. *J Cell Sci*. 2020;133(18):jcs239889. doi:10.1242/jcs.239889

233. Khalilgharibi N, Mao Y. To form and function: on the role of basement membrane mechanics in tissue development, homeostasis and disease. *Open Biol*. 2022;11(2):200360. doi:10.1098/rsob.200360

234. Li H, Zheng Y, Han YL, Cai S, Guo M. Nonlinear elasticity of biological basement membrane revealed by rapid inflation and deflation. *Proc Natl Acad Sci*. 2021;118(11):e2022422118. doi:10.1073/pnas.2022422118

235. Parsa S, Ramasamy SK, De Langhe S, et al. Terminal end bud maintenance in mammary gland is dependent upon FGFR2b signaling. *Dev Biol*. 2008;317(1):121-131. doi:https://doi.org/10.1016/j.ydbio.2008.02.014

236. Yong H-Y, Kim I-Y, Kim JS, Moon A. ErbB2-enhanced invasiveness of H-Ras MCF10A breast cells requires MMP-13 and uPA upregulation via p38 MAPK signaling. *Int J Oncol*. 2010;36(2):501-507.

237. Beliveau A, Mott JD, Lo A, et al. Raf-induced MMP9 disrupts tissue architecture of human breast cells in three-dimensional culture and is necessary for tumor growth in vivo. *Genes Dev*. 2010;24(24):2800-2811. doi:10.1101/gad.1990410

238. Mackay AR, Gomez DE, Cottam DW, Rees RC, Nason AM, Thorgeirsson UP. Identification of the 72-kDa (MMP-2) and 92-kDa (MMP-9) gelatinase/type IV collagenase in preparations of laminin and Matrigel. *Biotechniques*. 1993;15(6):1048-1051.

239. Gillette KM, Forbes K, Sehgal I. Detection of Matrix Metalloproteinases (MMP), Tissue Inhibitor of Metalloproteinase-2, Urokinase and Plasminogen Activator Inhibitor-1 within Matrigel and Growth Factor-Reduced Matrigel Basement Membrane. *Tumori J*. 2003;89(4):421-425. doi:10.1177/030089160308900415

240. Rasmussen HS, McCann PP. Matrix metalloproteinase inhibition as a novel anticancer strategy: a review with special focus on batimastat and marimastat. *Pharmacol Ther*. 1997;75(1):69-75. doi:10.1016/s0163-7258(97)00023-5

241. Živanović S, Pavić A. Quantification of dynamic excitation potential of pedestrian population crossing footbridges. *Shock Vib*. 2011;18(4):563-577. doi:10.3233/SAV-2010-0562

242. Noethel B, Ramms L, Dreissen G, et al. Transition of responsive mechanosensitive elements from focal adhesions to adherens junctions on epithelial differentiation. *Mol Biol Cell*. 2018;29(19):2317-2325. doi:10.1091/mbc.E17-06-0387

243. Green KA, Streuli CH. Apoptosis regulation in the mammary gland. *Cell Mol Life Sci*. 2004;61(15):1867-1883. doi:10.1007/s00018-004-3366-y

244. Humphreys RC, Krajewska M, Krnacik S, et al. Apoptosis in the terminal endbud of the murine mammary gland: a mechanism of ductal morphogenesis. *Development*. 1996;122(12):4013-4022. doi:10.1242/dev.122.12.4013

245. Mailleux AA, Overholtzer M, Brugge JS. Lumen formation during mammary epithelial morphogenesis: Insights from in vitro and in vivo models. *Cell Cycle*. 2008;7(1):57-62. doi:10.4161/cc.7.1.5150

246. Mailleux AA, Overholtzer M, Schmelzle T, Bouillet P, Strasser A, Brugge JS. BIM regulates apoptosis during mammary ductal morphogenesis, and its absence reveals alternative cell death mechanisms. *Dev Cell*. 2007;12(2):221-234. doi:10.1016/j.devcel.2006.12.003

247. Eisenhoffer GT, Loftus PD, Yoshigi M, et al. Crowding induces live cell extrusion to maintain homeostatic cell numbers in epithelia. *Nature*. 2012;484(7395):546-549. doi:10.1038/nature10999

248. Taddei ML, Giannoni E, Fiaschi T, Chiarugi P. Anoikis: an emerging hallmark in health and diseases. *J Pathol*. 2012;226(2):380-393. doi:10.1002/path.3000

249. Malagobadan S, Nagoor NH. Anoikis. In: Boffetta P, Hainaut PBT-E of C (Third E, eds. Oxford: Academic Press; 2019:75-84. doi:https://doi.org/10.1016/B978-0-12-801238-3.65021-3

250. Rosen K, Shi W, Calabretta B, Filmus J. Cell detachment triggers p38 mitogen-activated protein kinase-dependent overexpression of Fas ligand. A novel mechanism of Anoikis of intestinal epithelial cells. *J Biol Chem*. 2002;277(48):46123-46130. doi:10.1074/jbc.M207883200

251. Fouquet S, Lugo-Martínez VH, Faussat AM, et al. Early loss of E-cadherin from cell-cell contacts is involved in the onset of anoikis in enterocytes. *J Biol Chem*. 2004;279(41):43061-43069. doi:10.1074/jbc.M405095200

252. Gudipaty SA, Rosenblatt J. Epithelial cell extrusion: Pathways and pathologies. *Semin Cell Dev Biol*. 2017;67:132-140. doi:https://doi.org/10.1016/j.semcdb.2016.05.010

253. Marshall TW, Lloyd IE, Delalande JM, Näthke I, Rosenblatt J. The tumor suppressor adenomatous polyposis coli controls the direction in which a cell extrudes from an epithelium. *Mol Biol Cell*. 2011;22(21):3962-3970. doi:10.1091/mbc.E11-05-0469

254. Hope JM, Lopez-Cavestany M, Wang W, Reinhart-King CA, King MR. Activation of Piezo1 sensitizes cells to TRAIL-mediated apoptosis through mitochondrial outer membrane permeability. *Cell Death Dis*. 2019;10(11):837. doi:10.1038/s41419-019-2063-6

255. Li X-F, Zhang Z, Chen Z-K, Cui Z-W, Zhang H-N. Piezo1 protein induces the apoptosis of human osteoarthritis-derived chondrocytes by activating caspase-12, the signaling marker of ER stress. *Int J Mol Med*. 2017;40(3):845-853. doi:10.3892/ijmm.2017.3075

256. Song Y, Chen J, Zhang C, et al. Mechanosensitive channel Piezo1 induces cell apoptosis in pancreatic cancer by ultrasound with microbubbles. *iScience*. 2022;25(2):103733.

doi:https://doi.org/10.1016/j.isci.2022.103733

257. Wang B, Ke W, Wang K, et al. Mechanosensitive Ion Channel Piezo1 Activated by Matrix Stiffness Regulates Oxidative Stress-Induced Senescence and Apoptosis in Human Intervertebral Disc Degeneration. Ding W, ed. *Oxid Med Cell Longev*. 2021;2021:8884922. doi:10.1155/2021/8884922

258. Rambur A, Lours-Calet C, Beaudoin C, et al. Sequential Ras/MAPK and PI3K/AKT/mTOR pathways recruitment drives basal extrusion in the prostate-like gland of Drosophila. *Nat Commun*. 2020;11(1). doi:10.1038/s41467-020-16123-w

259. Han Y, Liu C, Zhang D, et al. Mechanosensitive ion channel Piezo1 promotes prostate cancer development through the activation of the Akt/mTOR pathway and acceleration of cell cycle. *Int J Oncol*. 2019;55(3):629-644. doi:10.3892/ijo.2019.4839

260. Zhang S, Cao S, Gong M, et al. Mechanically activated ion channel Piezo1 contributes to melanoma malignant progression through AKT/mTOR signaling. *Cancer Biol Ther*. 2022;23(1):336-347. doi:10.1080/15384047.2022.2060015

261. Caldwell RA, Clemo HF, Baumgarten CM. Using gadolinium to identify stretch-activated channels: technical considerations. *Am J Physiol Physiol*. 1998;275(2):C619-C621. doi:10.1152/ajpcell.1998.275.2.C619

262. Kuntze A, Goetsch O, Fels B, et al. Protonation of Piezo1 Impairs Cell-Matrix Interactions of Pancreatic Stellate Cells. *Front Physiol*. 2020;11(February):1-15. doi:10.3389/fphys.2020.00089

263. Park JS, Chu JS, Tsou AD, et al. The effect of matrix stiffness on the differentiation of mesenchymal stem cells in response to TGF-β. *Biomaterials*. 2011;32(16):3921-3930. doi:10.1016/j.biomaterials.2011.02.019

264. Sun M, Chi G, Xu J, et al. Extracellular matrix stiffness controls osteogenic differentiation of mesenchymal stem cells mediated by integrin α5. *Stem Cell Res Ther*. 2018;9(1):1-13. doi:10.1186/s13287-018-0798-0

265. Smith LR, Cho S, Discher DE. Stem Cell Differentiation is Regulated by Extracellular Matrix Mechanics. *Physiology (Bethesda)*. 2018;33(1):16-25. doi:10.1152/physiol.00026.2017

266. Califano JP, Reinhart-King CA. Substrate Stiffness and Cell Area Predict Cellular Traction Stresses in Single Cells and Cells in Contact. *Cell Mol Bioeng*. 2010;3(1):68-75. doi:10.1007/s12195-010-0102-6

267. Doss BL, Pan M, Gupta M, et al. Cell response to substrate rigidity is regulated by active and passive cytoskeletal stress. *Proc Natl Acad Sci U S A*. 2020;117(23):12817-12825. doi:10.1073/pnas.1917555117

268. Mark C, Grundy TJ, Strissel PL, et al. Collective forces of tumor spheroids in three-dimensional biopolymer networks. Bassereau P, Akhmanova A, Betz T, Nassoy P, eds. *Elife*. 2020;9:e51912. doi:10.7554/eLife.51912

269. Kenoian A, Rasmussen R. Design of Device to Stretch Tunable Stiffness Substrates for Cell Studies. 2009.

270. Quinlan AM, Sierad LN, Capulli AK, Firstenberg LE, Billiar KL. Combining dynamic stretch and tunable stiffness to probe cell mechanobiology in vitro. *PLoS One*. 2011;6(8). doi:10.1371/journal.pone.0023272

271. Avadhanam B, Gupta V, Butlin M, Avolio A. SUBSTRATE STIFFNESS AND FREQUENCY OF CYCLIC STRETCH MODULATE EXPRESSION OF ENDOTHELIAL NITRIC OXIDE SYNTHASE IN HUMAN ENDOTHELIAL CELLS. *J Hypertens*. 2019;37. https://journals.lww.com/jhypertension/Fulltext/2019/07001/SUBSTRATE_STIFFNESS_AND_FREQUENCY_OF_CYCLIC.184.aspx.

272. Conforte ML, Mavromatis M, Youssef J, Pins G, Billiar KL. A Method to Determine the Effect of Stiffness and Stretch on Cell Phenotype. In: *Proceedings of the IEEE 32nd Annual Northeast Bioengineering Conference*. ; 2006:79-80. doi:10.1109/NEBC.2006.1629761

273. Du R, Li D, Huang Y, et al. Effect of mechanical stretching and substrate stiffness on the morphology, cytoskeleton and nuclear shape of corneal endothelial cells. *Med Nov Technol Devices*. 2022;16:100180. doi:https://doi.org/10.1016/j.medntd.2022.100180

274. Slater K, Partridge J, Nandivada H. Tuning the Elastic Moduli of Corning ® Matrigel ® and Collagen I 3D Matrices by Varying the Protein Concentration Application Note.

Corning Inc Life Sci. 2018;1(I):1-8.

275. Douthwright S, Sluder G. Live Cell Imaging: Assessing the Phototoxicity of 488 and 546 nm Light and Methods to Alleviate it. *J Cell Physiol*. 2017;232(9):2461-2468. doi:10.1002/jcp.25588

276. Hamill K. LaNts and Laminins, The Hamill lab blog. https://lantsandlaminins.com/laminins/.

277. Dunsmore SE. Treatment of COPD: a matrix perspective. *Int J Chron Obstruct Pulmon Dis*. 2008;3(1):113-122. doi:10.2147/copd.s1119

278. Qu Y, Han B, Yu Y, et al. Evaluation of MCF10A as a Reliable Model for Normal Human Mammary Epithelial Cells. *PLoS One*. 2015;10(7):e0131285. https://doi.org/10.1371/journal.pone.0131285.

279. Weisshart K. The basic Principle of Airyscanning. *Technol Note*. 2014;July. doi:10.1080/10511970.2010.518550

280. Huff J. The Airyscan detector from ZEISS: confocal imaging with improved signal-to-noise ratio and super-resolution. *Nat Methods*. 2015;12(12):ii. doi:10.1038/NMETH.F.388

10 Appendix

pNIPAM-microgel production protocol by Susan Babu (DWI, RWTH Aachen)

Poly N-isopropyl acrylamide (pNIPAM) based thermoresponsive microgels were produced by droplet microfluidics and contained 15 wt% of NIPAM and were dyed with Rhodamine. They were also modified with glycidyl methacrylate (GMA) to introduce epoxy groups on their surface. The epoxy groups could then react with the free amine groups of the PEG matrix to form the covalent bonds by incubating the samples at 37 ^{o}C in media overnight. The inner phase during the microfluidics contained 176.47 mg of NIPAM, 10 mg of photoinitiator (Lithium phenyl-2,4,6-trimethylbenzoylphosphinate), 5.29 mg of crosslinker (N,N'-methylenebisacrylamide) and 18.18 mg of GMA dissolved in 1000 µL of water. Four replicas of 15 µL PEG gel droplets containing the microgels were made and after the gelation of the matrix hydrogel, 1 mL of RPMI media (Gibco) with 10% fetal bovine serum and 1% Pen-Strep was added and left for incubation at 37 ^{o}C in media overnight. The gels were non-degradable and had a storage modulus of 45 Pa.

Correction for deformations via transformation in three dimensions by Dr. Ronald Springer

Deformationskorrektur mittels affiner Transformation in drei Raumdimensionen

Dr. Ronald Springer

17. April 2021

1 Dehnungskorrektur in drei Dimensionen

Aus der Kenntnis der Beadspositionen (Bead: fluoreszierende Kugel mit einem Durchmesser von 200 nm)) im Substrat vor und nach der Deformation lassen sich die Parameter der Deformation (affine Transformation) bestimmen. Anstelle der Beads können in der Probe auch kleine Volumina (Quader) betrachtet werden, die über die Zeit verfolgt werden.
Die Koordinaten der Beads bzw. der Volumina des nicht deformierten Substrates sollen mit x, y und z bezeichnet werden, die des deformierten Substrates mit $\bar{x}$, $\bar{y}$ und $\bar{z}$. Die 12 Parameter a bis m bestimmen die affine Transformation (Rotation, Torsion, Dehnung, Translation). Es gilt dabei:

$$\begin{pmatrix} \bar{x} \\ \bar{y} \\ \bar{z} \\ 1 \end{pmatrix} = \begin{pmatrix} a & b & c & d \\ e & f & g & h \\ j & k & l & m \\ 0 & 0 & 0 & 1 \end{pmatrix} \cdot \begin{pmatrix} x \\ y \\ z \\ 1 \end{pmatrix} \tag{1}$$

Mittels der Methode der kleinsten Fehlerquadrate (engl. least square fit) können die einzelnen Parameter bestimmt werden.

$$\frac{\partial}{\partial a,b,c,d} \sum_{i=1}^{N} [\bar{x}_i - (ax_i + by_i + cz_i + d)]^2 = 0 \tag{2}$$

$$\frac{\partial}{\partial e,f,g,h} \sum_{i=1}^{N} [\bar{y}_i - (ex_i + fy_i + gz_i + h)]^2 = 0 \tag{3}$$

$$\frac{\partial}{\partial j,k,l,m} \sum_{i=1}^{N} [\bar{z}_i - (jx_i + ky_i + lz_i + m)]^2 = 0 \tag{4}$$

Daraus resultieren drei Vektorgleichungen bzw. ein Gleichungssystem mit neun Gleichungen:

$$\begin{pmatrix} \sum_{i=1}^{N} x_i^2 & \sum_{i=1}^{N} x_i y_i & \sum_{i=1}^{N} x_i z_i & \sum_{i=1}^{N} x_i \\ \sum_{i=1}^{N} x_i y_i & \sum_{i=1}^{N} y_i^2 & \sum_{i=1}^{N} y_i z_i & \sum_{i=1}^{N} y_i \\ \sum_{i=1}^{N} x_i z_i & \sum_{i=1}^{N} y_i z_i & \sum_{i=1}^{N} z_i^2 & \sum_{i=1}^{N} z_i \\ \sum_{i=1}^{N} x_i & \sum_{i=1}^{N} y_i & \sum_{i=1}^{N} z_i & \sum_{i=1}^{N} 1 \end{pmatrix} \begin{pmatrix} a \\ b \\ c \\ d \end{pmatrix} = \begin{pmatrix} \sum_{i=1}^{N} x_i \bar{x}_i \\ \sum_{i=1}^{N} y_i \bar{x}_i \\ \sum_{i=1}^{N} z_i \bar{x}_i \\ \sum_{i=1}^{N} \bar{x}_i \end{pmatrix} \tag{5}$$

$$\begin{pmatrix} \sum_{i=1}^{N} x_i^2 & \sum_{i=1}^{N} x_i y_i & \sum_{i=1}^{N} x_i z_i & \sum_{i=1}^{N} x_i \\ \sum_{i=1}^{N} x_i y_i & \sum_{i=1}^{N} y_i^2 & \sum_{i=1}^{N} y_i z_i & \sum_{i=1}^{N} y_i \\ \sum_{i=1}^{N} x_i z_i & \sum_{i=1}^{N} y_i z_i & \sum_{i=1}^{N} z_i^2 & \sum_{i=1}^{N} z_i \\ \sum_{i=1}^{N} x_i & \sum_{i=1}^{N} y_i & \sum_{i=1}^{N} z_i & \sum_{i=1}^{N} 1 \end{pmatrix} \begin{pmatrix} e \\ f \\ g \\ h \end{pmatrix} = \begin{pmatrix} \sum_{i=1}^{N} x_i \bar{y}_i \\ \sum_{i=1}^{N} y_i \bar{y}_i \\ \sum_{i=1}^{N} z_i \bar{y}_i \\ \sum_{i=1}^{N} \bar{y}_i \end{pmatrix} \tag{6}$$

$$\begin{pmatrix} \sum_{i=1}^{N} x_i^2 & \sum_{i=1}^{N} x_i y_i & \sum_{i=1}^{N} x_i z_i & \sum_{i=1}^{N} x_i \\ \sum_{i=1}^{N} x_i y_i & \sum_{i=1}^{N} y_i^2 & \sum_{i=1}^{N} y_i z_i & \sum_{i=1}^{N} y_i \\ \sum_{i=1}^{N} x_i z_i & \sum_{i=1}^{N} y_i z_i & \sum_{i=1}^{N} z_i^2 & \sum_{i=1}^{N} z_i \\ \sum_{i=1}^{N} x_i & \sum_{i=1}^{N} y_i & \sum_{i=1}^{N} z_i & \sum_{i=1}^{N} 1 \end{pmatrix} \begin{pmatrix} j \\ k \\ l \\ m \end{pmatrix} = \begin{pmatrix} \sum_{i=1}^{N} x_i \bar{z}_i \\ \sum_{i=1}^{N} y_i \bar{z}_i \\ \sum_{i=1}^{N} z_i \bar{z}_i \\ \sum_{i=1}^{N} \bar{z}_i \end{pmatrix} \tag{7}$$

Die drei Vektorgleichungen können auch zu einer Gleichung zusammengefasst werden.

$$\begin{pmatrix} \sum_{i=1}^{N} x_i^2 & \sum_{i=1}^{N} x_i y_i & \sum_{i=1}^{N} x_i z_i & \sum_{i=1}^{N} x_i \\ \sum_{i=1}^{N} x_i y_i & \sum_{i=1}^{N} y_i^2 & \sum_{i=1}^{N} y_i z_i & \sum_{i=1}^{N} y_i \\ \sum_{i=1}^{N} x_i z_i & \sum_{i=1}^{N} y_i z_i & \sum_{i=1}^{N} z_i^2 & \sum_{i=1}^{N} z_i \\ \sum_{i=1}^{N} x_i & \sum_{i=1}^{N} y_i & \sum_{i=1}^{N} z_i & \sum_{i=1}^{N} 1 \end{pmatrix} \begin{pmatrix} a & c & j \\ b & f & k \\ c & g & l \\ d & h & m \end{pmatrix} = \begin{pmatrix} \sum_{i=1}^{N} x_i \bar{x}_i & \sum_{i=1}^{N} x_i \bar{y}_i & \sum_{i=1}^{N} x_i \bar{z}_i \\ \sum_{i=1}^{N} y_i \bar{x}_i & \sum_{i=1}^{N} y_i \bar{y}_i & \sum_{i=1}^{N} y_i \bar{z}_i \\ \sum_{i=1}^{N} z_i \bar{x}_i & \sum_{i=1}^{N} z_i \bar{y}_i & \sum_{i=1}^{N} z_i \bar{z}_i \\ \sum_{i=1}^{N} \bar{x}_i & \sum_{i=1}^{N} \bar{y}_i & \sum_{i=1}^{N} \bar{z}_i \end{pmatrix} \tag{8}$$

Anstelle der komponentenweisen Summation für die Matrizen können auch alle Matrizen erzeugt und anschließend summiert werden.

$$\sum_{i=1}^{N} \begin{pmatrix} x_i^2 & x_i y_i & x_i z_i & x_i \\ x_i y_i & y_i^2 & y_i z_i & y_i \\ x_i z_i & y_i z_i & z_i^2 & z_i \\ x_i & y_i & z_i & 1 \end{pmatrix} \cdot \begin{pmatrix} a & c & j \\ b & f & k \\ c & g & l \\ d & h & m \end{pmatrix} = \sum_{i=1}^{N} \begin{pmatrix} x_i \bar{x}_i & x_i \bar{y}_i & x_i \bar{z}_i \\ y_i \bar{x}_i & y_i \bar{y}_i & y_i \bar{z}_i \\ z_i \bar{x}_i & z_i \bar{y}_i & z_i \bar{z}_i \\ \bar{x}_i & \bar{y}_i & \bar{z}_i \end{pmatrix} \tag{9}$$

(Es ist $\sum_{i=1}^{N} 1 = N$. Wegen der besseren Lesbarkeit wurde Ausdruck mit der Summe über die Einsen stehen gelassen.)
Nach Inversion der linken Matrix und deren Mutliplikation mit der Gleichung erhält man sofort explizit die Lösung der Gleichung und damit alle Koeffizienten.
Mittels der so bestimmten Koeffizienten a bis m werden die korrigierten Beadspositionen bzw. Voluminapositionen mit Gleichung 1 berechnet.